Recent Trends
in Charged Particle Optics and Surface Physics Instrumentation

Proceedings
of the 13th International Seminar,
held in Skalský dvůr near Brno, Czech Republic,
from June 25 to June 29, 2012,
organized by
the Institute of Scientific Instruments of the ASCR, v. v. i.,

Edited by Filip Mika

The publishers have made every effort to reproduce the papers at their optimum contrast and with optimum resolution from materials provided by the authors. The publishers accept no liability for the loss of image quality resulting from supply of poor original material or improperly prepared digital records.

PREFACE

Dear colleagues and friends,

welcome to the 13th Seminar on Recent Trends in Charged Particle Optics and Surface Physics Instrumentation, which has traditionally been held every two years in the hotel Skalský dvůr, in the seclusion of the Bohemian-Moravian Highlands.

The origin of this Seminar was a traditional summer seminar held at the Institute of Scientific Instruments in Brno on the occasion of the visits of Professor Tom Mulvey (University of Aston in Birmingham), whose presence justified the English language of the seminar. In 1989 we invited five foreign guests: Prof. T. Mulvey (UK), Prof. M. Troyon (France), F.J. Pijper (The Netherlands), Dr. L. Veneklasen (Germany) and Prof. K.-H. Herrmann (Germany), making this the 1st Seminar under the current name. In 1990 (2nd Seminar), there were as many as 30 participants from 5 countries.

The three-day Seminar is divided into ten sections, one of which consists of short oral introductions of the poster presentations. Traditionally, a half-day trip is organized on Wednesday afternoon, a concert is held on Thursday evening and special social events with Moravian wine and Czech beer are prepared for the participants every night.

The main goal of this seminar is to gather together a relatively small group of top scientists from the field of charged particle optics and surface physics, to give them the chance to discuss their topics during the three days and evenings. We would like to offer something different than the large conferences where it is sometimes difficult to meet your friends.

We greatly appreciate your coming to the forest to participate in a small seminar even though a huge amount of other conferences and seminars is organised in the world.

Enjoy your stay at Skalský dvůr.

Ilona Müllerová

CONTENTS

MEASUREMENTS OF CURRENT DENSITY DISTRIBUTION IN E-BEAM WRITER

J. Bok, V. Kolařík

Institute of Scientific Instruments of the ASCR, v. v .i., Královopolská 147, 612 64 Brno, CZ
E-mail: bok@isibrno.cz

An e-beam writer with a variable shaped beam needs a bright and stable source of electrons but also a homogeneous square beam segment. This is the starting element out of which smaller rectangular-shaped variable-sized patterns are selected (stamps). Current inhomogeneity of the starting element would cause a different current density of various stamps that negatively impacts the exposure quality. This problem implies the necessity of analysing and monitoring the current density distribution in the starting beam element.

A set of methods enabling the measurement of the beam current distribution was presented in the past. But only a part of them is suitable for the evaluation of the current density distribution in the exposure plane where the beam spot size is below 10 μm. We implemented a method based on the knife-edge approach [1], when a part of the starting element is blanked out and the current within the remaining "open" part (segment) is measured. The information of the current distribution (1 or 2 dimensional) is obtained by stepwise opening of selected segments. We aimed at using the stamp forming system of the e-beam writer to measure 2D current density distribution.

The measurements were performed using the e-beam writer Tesla BS 600. The forming system is composed of the first and the second rectangular shutters; the beam cross-over is in between them (Fig. 1) [2]. The beam size is adjusted by the electrostatic beam deflection in the cross-over plane independently in the two axes. However, the mutual position of the beam and the first shutter remains unchanged. Thus only the segments (or stamps) having the identical upper right corner (the position [6.3; 6.3] μm in the selected coordinates depicted in the Fig. 2) are available. This is why it is not possible to directly measure the current of an arbitrarily positioned beam segment.

The above-described limitation of the forming system implied the necessary modification of the knife-edge method: the current density of an arbitrary beam segment is derived from the current measurement of several appropriate stamps. We are searching the current density $j(x, y)$ of the element sized $\Delta x \times \Delta y$, which lower left corner has the coordinates $(x; y)$, where $x \in \langle 0; 6.3 - \Delta x \rangle$ and $y \in \langle 0; 6.3 - \Delta y \rangle$:

$$j(x, y) = \frac{1}{\Delta x \Delta y} \sum_{j=y-1}^{y} \sum_{i=x-1}^{x} (-1)^{(x+y)-(i+j)} I\left[s_i, s_j\right].$$

The $I\left[s_i, s_j\right]$ is the measured current of the stamp with s_i width and s_j height; this stamp size being $[s_i; s_j] = [(6.3–x); (6,3–y)]$ μm. By the current measurement in the appropriate stamps and using the equation above, the current density distribution within the whole starting element can be evaluated.

The presented procedure was implemented using National Instruments LabVIEW environment. Appropriate stamp size is set automatically through the service channel

to the basic exposure SW, Expo.NET. The current is measured using the Faraday cage and the pA-meter Keithley 487 through the IEEE-488 bus and the Agilent IEEE-488 to USB converter. An example of the current density distribution obtained by this method is in the Fig. 3a, while the Fig. 3b shows an equivalent image from a luminescent screen irradiated by the starting beam element.

The advantage of this method is that only the native parts of the e-beam writer are necessary. On the other hand, the drawback is a low signal to noise ratio (particularly in the left lower part of the starting element). In order to obtain conclusive results, a filtering procedure must be included into the measurement cycle which disables registration of short-term current density variations. We can conclude that the described procedure helps us in accurate beam adjustments (that is necessary for diffractive optics applications, [3]) but it also enables studies of the beam source long term stability [4].

Figure 2 Principle of the rectangular stamp forming (top view).
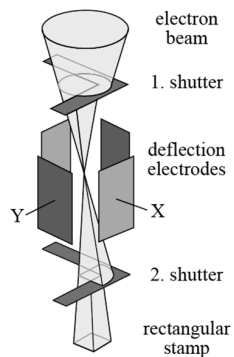
Figure 1 Beam forming system of the e-beam writer Tesla BS 600.
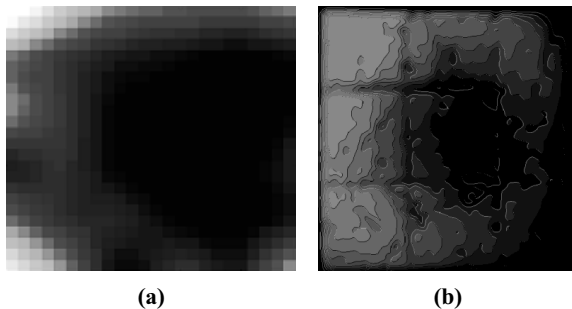
Figure 3 Beam current density distribution: **(a)** modified knife-edge method, filtered output (left); **(b)** equivalent image from the luminescent screen, enhanced contrast (right).

(a)   **(b)**

References:
[1] M. Sakakibara *et al.*, Measurements of Variable-Shaped Electron Beam with Solid-State Detector and Scattering Aperture, *Japanese J. of Applied Physics*, **Vol. 46**, **No. 9B**, pp. 6616–6170, 2007.
[2] V. Kolarik *et al.*, Writing System with a Shaped Electron Beam, *Jemná mechanika a optika*, **Vol. 53**, **No. 1** (2008), pp. 11–16, ISSN 0447–6441 (*in Czech*).
[3] M. Matejka *et al.*, Comparison of techniques for diffraction grating topography analysis. *In Proc. 12th Int'l Seminar on Recent Trends in CPO*. Brno : ISI AS CR, 2010, pp. 29-32. ISBN 978-80-254-6842-5.
[4] F. Matejka *et al.*, Modification of the Schottky Fe ZrO/W electron emitter. *In Proc. 12th Int'l Seminar on Recent Trends in CPO*. Brno : ISI AS CR, 2010, pp. 13-14. ISBN 978-80-254-6842-5.

QUALITY ASSESSMENT OF SCINTILLATION DETECTOR IN SEM USING MTF

J. Bok, P. Schauer

Institute of Scientific Instruments of the ASCR, v.v.i., Královopolská 147, 612 64 Brno, CZ
E-mail: bok@isibrno.cz

One of the recent trends in S(T)EM is increasing of the e-beam scanning speed. In general, higher speeds decrease object degradation and prevent image artifacts caused by slow electrical discharging. However, the increase of the scanning speed is limited by the time response of the signal-electron detector [1]. When the detector response is slower than the scanning speed, it can have negative influence to the quality of the scanned image, such as contrast reduction and image blurring. Usually, the rise and fall edges of the time response curve to a square electron pulse have more complex form, such as a multi-exponential function of time. Evaluate and compare the time-dependent edges in context of their influence on the image quality is rather complicated. Therefore, we propose to express the detector time response by the modulation transfer function (MTF), which contains all relevant information. It can give the answer to the important question, what maximum scanning speed can be used not to significantly decrease the image quality.

MTF represents relative image contrast as a function of spatial frequency [2]. The spatial frequency is expression of the image detail; higher spatial frequencies generally correspond to fine details, low frequencies represent global information about the shape. The spatial frequency can be expressed in units of cycles per pixel ($pixel^{-1}$), which means how many image alternations from a black point to a white point in the distance of one pixel are presented. Thus, the spatial frequency in the units $pixel^{-1}$ is always lower than 1, because a meaningful black-to-white alternation occupies distance above one pixel.

MTF can be calculated as the magnitude of the Fourier transform of the point spread function (PSF). PSF represents a line-scan of one pixel point broadened by the detector time response. In this work, PSF of the detector was acquired using the CL device [3] in which the detector can be irradiated by electrons for a variable time. Thus, one pixel line-scan can be simulated by irradiation for period arising from defined scanning speed. We aimed to measure PSF and calculate MTF of a scintillation detector, which is the most used type of electron detector in S(T)EM. The scintillation detector used consisted of single crystal scintillator produced by CRYTUR, photomultiplier tube Tesla 65-PK-415 and preamplifier Hamamatsu C9663. The scintillation detector was alternated using three samples of scintillators: YAG:Ce #1 with high concentration of the defect centers, standard YAG:Ce #2, and standard YAP:Ce.

The fall edges of the time response for the three alternative of the scintillation detector are shown in Fig. 1. One can conclude that the curve with the shorter decay (YAP:Ce) is better for fast scanning. However, these curves don't contain any explicit information about the resulting image. MTFs for a specific scanning speed are drawn in Fig. 2. The MTF curve with bigger area under the curve represents higher image contrast for higher spatial frequencies. In addition, the spatial frequency 0.5 $pixel^{-1}$ corresponds to difference between two image pixels, so MTF at this spatial frequency is particularly important.

In Fig 3 is shown that the contrast between the adjacent pixels increases with the decreasing scanning speed. The influence of the speed increase on contrast between two pixels is depicted in Fig. 4. This graph answers the question what maximum scanning speed can be used, if one requires contrast between two pixels at least, let say, 50 %. To conclude, MTF seems to be very useful to express the influence of the detector time response on the resulting image quality. For complete detector evaluation, MTF should be extended by the DQE function, which quantifies the noise performance of the detector.
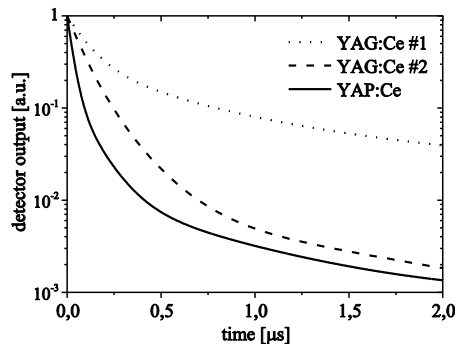
Figure 1 The fall edges of the time response to 100 ns square electron pulse of the three scintillation detector alternatives.
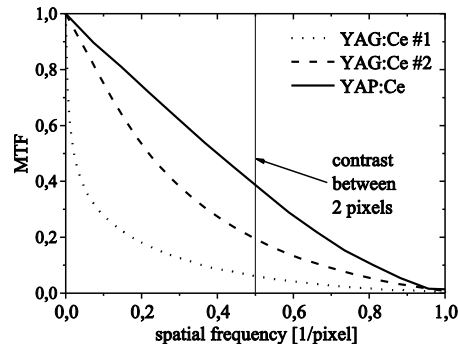
Figure 2 MTF of the three scintillation detector alternatives. The scanning speed is 100 ns/pixel.
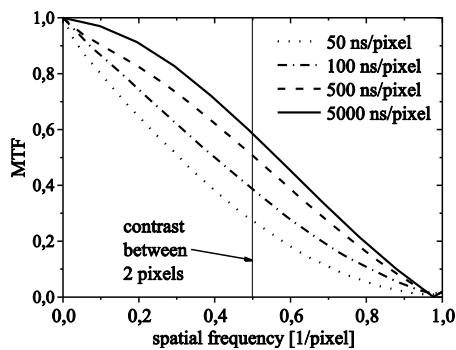
Figure 3 MTF of the scintillation detector using YAP:Ce for various scanning speeds.
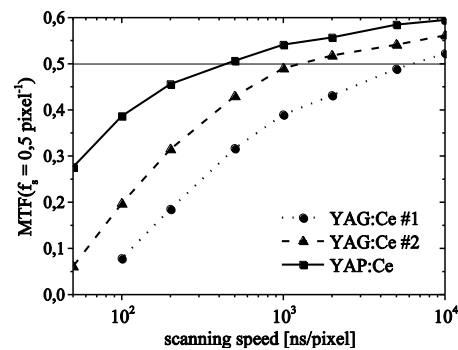
Figure 4 MTF at spatial frequency 0.5 pixel^{-1} as a function of the scanning speed. MTFs are drawn for the three scint. detectors alternatives.

References:
[1] Novák L., Journal of Microscopy **233** (2009), p. 76-83.
[2] Pratt W. K., Digital Image Processing (2001), p. 23-44.
[3] Bok J., Schauer P., Rev. Sci. Instrum. **82** (2011) 113109.

SIMULATED SEM IMAGES FOR 3D RECONSTRUCTION ASSESSMENT

P. Cizmar, K.-P. Johnsen, and C. G. Frase

Physikalisch-Technische Bundesanstalt, Bundesallee 100, D-38116 Braunschweig, Germany, e-mail: petr.cizmar@ptb.de

Three-dimensional (3D) scanning electron microscope (SEM) imaging of various samples ranging from nanometers to micrometers has recently become an important field. There is already a significant number of applications, yet many new are emerging. Quantitative measurement of surface wear and durability is indispensable e. g. for the future machine industry. 3D SEM reconstruction can provide extensive amount of information about volume changes and material transfer in inspected surfaces, which makes it one of the most suitable tools to measure wear. This technique is even more important, when such measurements are carried out in the nanometer scale. Semiconductor industry demands 3D metrology at the best possible resolution, where the 3D reconstruction is also essential for various applications.

3D reconstruction may only be rigorously applicable in metrology, when its accuracy has been assessed. Processing of a well-known sample would clearly furnish the most straight-forward method to evaluate a 3D-reconstruction technique. However, real images alone are not sufficient for several reasons. Firstly, all 3D measurement techniques suffer from inaccuracies and errors. Moreover, some of them may alter the sample adding more uncertainty after the processing. Performance of SEM imaging also varies and is strongly affected by drift, charging, noise, edge-effects, blur, etc. These effects are mostly random and thus also randomize the uncertainties. Therefore, the accuracy of the 3D-reconstruction technique itself would be uncertain due to the uncertainty of the input data.

Application of SEM image simulation eliminates the above mentioned issue. The sample is modeled and thus is entirely determined. The error of the SEM images including their inaccuracies are also completely defined. Therefore, the uncertainties may be thoroughly and accurately investigated in contrast with utilization of real images. Within this work, the SEM images have been simulated by a Monte-Carlo technique implemented at PTB [1].

This assessment method is universal and works with any 3D-reconstruction technique. In this work, the selected technique [3] (MeX software) is based on photogrammetry. The relocations of features in differently tilted SEM images of the same sample location provide the height information. Cross-correlation algorithms detect position of matching features providing a height map which is then interpolated across the entire field of view. This technique is thus clearly sensitive to lack of topography. Another possible 3D-reconstruction technique employs four off-axis detectors with different azimuthal angles. Differences in the grey level indicate inclination and directional angle.

Since the performance of 3D-reconstruction extensively depends on the sample shape, the assessment can only provide sample-specific accuracy values. The right choice of sample model is thus critical. When possible, models closely mimicking the intended real samples are recommended. However, search for the best possible performance is still feasible. The basic (first selected) model consists of three rows of cuboids with 300-nm-long sides. The heights of the cuboids varies from 50 nm to 300 nm. Beside the cuboid rows, the model contains a ramp from 0 to 300 nm of height. A sphere and a smaller cube have been integrated into the ramp. (See Figure.)

The performance of the investigated cross-correlation-based 3D-reconstruction technique with the basic model has been rather poor. This has most probably been caused by lack of any dense topography in the model. Optimization of the model by adding dense topography has enabled significantly better performance of the analyzed technique. Adding random dense topographical patterns and rounding sharp transitions have provided the best performance.

Images of a 3D calibration sample [2] (See Figure.) have been processed to verify the technique with real images as well . The sample consists of several steps forming a pyramid. The longest (lowest) side is 20 μm long. The good results show that the assessed technique is well applicable for samples of such dimensions.
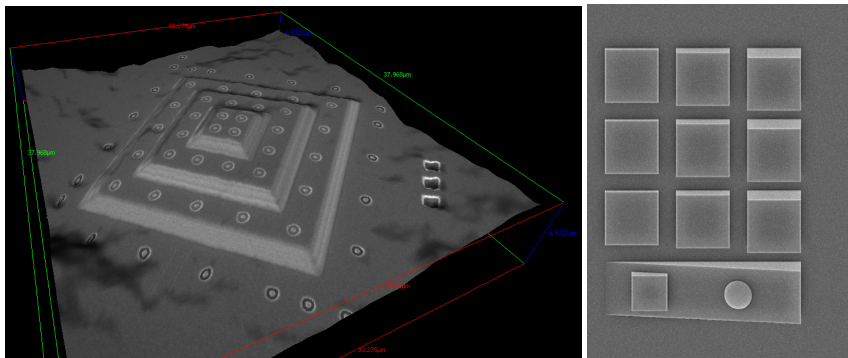

Figure: The visualization of the three-dimensional reconstructed surface of the real calibration sample (left) and the Monte-Carlo simulated SEM image of the tilted basic sample model (right).

[1] Johnsen K.-P., Frase C. G., Bosse H., Gnieser, D.: SEM image modeling using the new Monte Carlo model MCSEM, Proceedings of SPIE Vol. 7638, (2010)

[2] Ritter M., Dziomba T., Kranzmann A., Koenders L.: A landmark-based 3D calibration strategy for SPM, Meas. Sci. Technol. 18 (2007) 404-414

[3] Website: http://www.alicona.com/home/products/Mex/MeX.en.php

TOWARDS SECONDARY ION MASS SPECTROMETRY ON THE HELIUM ION MICROSCOPE

T. Wirtz[1], L. Pillatsch[1], N. Vanhove[1], D. Dowsett[1], S. Sijbrandij[2] and J. Notte[2]

[1]Department "Science and Analysis of Materials" (SAM), Centre de Recherche Public – Gabriel Lippmann, 41 rue du Brill, L-4422 Belvaux, Luxembourg
[2]Carl Zeiss NTS LLC, One Corporation Way, Peabody, MA, 01960
dowsett@lippmann.lu

The ORION Helium Ion Microscope (HIM) has become a well-established tool for high-resolution microscopy over the last years [1]. The ORION instrument is based on the atomic-sized ALIS gas field ion source, which has a brightness of $4 \cdot 10^9$ A/(cm^2·sr) and which leads to a probe size down to < 0.5 nm. The source can operate with helium and neon ions [2]. While secondary electrons are used for high-resolution high-contrast imaging, the detection of backscattered helium atoms can provide some composition information about the specimen.

In order to get chemical information with much higher sensitivity on the Helium Ion Microscope, we have investigated the feasibility of performing Secondary Ion Mass Spectrometry (SIMS). SIMS is an extremely powerful technique for analyzing surfaces owing in particular to its excellent sensitivity, high dynamic range, very high mass resolution and ability to differentiate between isotopes.

We have experimentally determined on a test set-up the secondary ion yields for different elements sputtered from different materials exposed to helium and neon ion beams. While the basic yields were found to be rather low compared to the ones found in conventional SIMS due to the use of rare gas elements for sputtering, as expected, these yields could be increased by several orders of magnitude by using reactive gas flooding during analysis (oxygen flooding for positive secondary ions [3], cesium flooding for negative secondary ions [4]). In addition, the experimentally determined sputtering yields coupled with modeled characteristics of the collision cascades triggered by He$^+$ and Ne$^+$ impacts allowed us to estimate the achievable lateral resolutions by taking into account the competition between sputtering and imaging.

The obtained results are very encouraging and the prospects of performing SIMS on the ORION are very interesting. In addition to having high-resolution microscopy and high-sensitivity chemical mapping on a single instrument, this information can be combined to reach a new level of correlative microscopy. This paper will present an overview of our experimental and simulation results and it will discuss the prospects of SIMS on the Helium Ion Microscope in terms of detection limits and lateral resolutions. Our experimental results show in particular that detection limits down to the ppm level are possible.
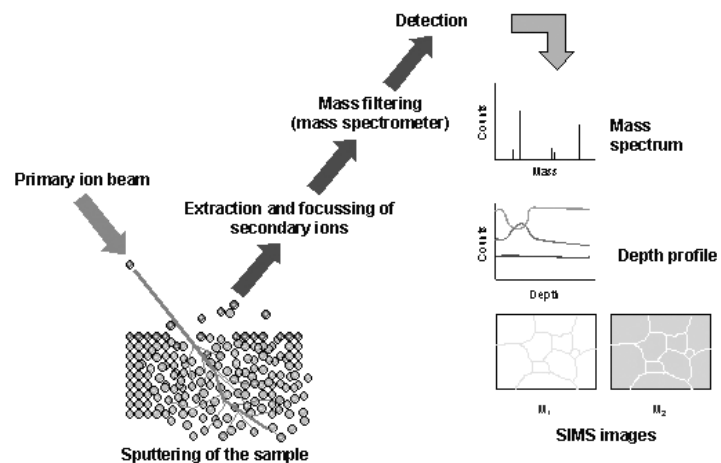
Figure 1: Schematic of Secondary Ion Mass Spectrometry and its main applications.
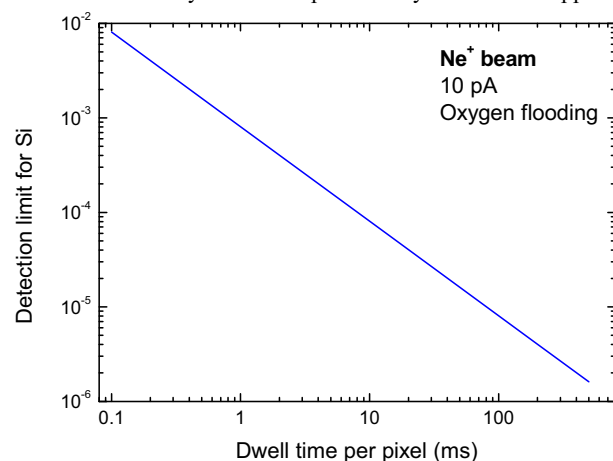
Figure 2: Detection limits obtained for Si with a 10 pA Ne$^+$ beam and oxygen flooding in the positive secondary ion mode.

[1] L. Scipioni, C.A. Sanford, J. Notte, B. Thompson, and S. McVey, J. Vac. Sci. Technol. B **27**, 3250 (2009)
[2] F. Rahman, S. McVey, L. Farkas, J. Notte, S. Tan, and R. Livengood, Scanning **33**, 1 (2011)
[3] K. Franzreb, J. Lorincik, and P. Williams, Surf. Sci. **573**, 291 (2004)
[4] P. Philipp, T. Wirtz, H.-N. Migeon, and H. Scherrer, Int. J. Mass Spectrom. **253**, 71 (2006)

ELECTRON BEAM CUTTING OF NON-METALS

L. Dupák

Institute of Scientific Instruments AS CR, v.v.i., Královopolská 147,612 64 Brno, Czech Republic
e-mail: ldupak@isibrno.cz

Various materials are difficult to cut or drill, e.g. due to their mechanical properties (hardness, fragility). Also, sometimes the required hole shape and dimensions may be difficult to obtain by mechanical machining or the efficiency of such process is low. Electron beam machining is one way to overcome these issues [1], [2]. It is based on the melting and evaporation of the material by the intense electron beam.

The presented experiments were performed on the desktop electron beam welder MEBW-60/2 [3], developed at the Institute of Scientific Instruments AS CR, v.v.i. at Brno. It is also manufactured and sold by the Focus GmbH company [4] under licence.

In the following experiments, several sets of grooves were prepared, both in quartz glass (see **Figure 1**) and Al$_2$O$_3$ ceramics, to find out the influence of various beam parameters on groove dimensions. The experimental conditions were as follows: acceleration voltage 50 kV, beam current 0.1-1 mA, machining speed 2.5-50 mm·s^{-1}.

Typically, the cross section of the created grooves is triangular. The dependence of the groove width on the machining speed for several values of the beam current is shown in **Figure 4**. It is apparent that the depth of the groove decreases with increasing machining speed. Similarly, the width of the groove rises with decreasing speed. As the electron beam moves faster, less energy is transferred and thus less material is melted.

Although the beam diameter increases with beam current only slightly from 0.12 mm for 0.2 mA to 0.15 mm for 1 mA, the width of the groove grows approximately twice. The groove depth increases slower than the beam current. This can be explained by the melted material flowing down and refilling the bottom of the groove.

Using the right beam parameters, it is possible to cut through the quartz glass plate. Together with computer-controlled deflection of the electron beam, various shapes can be cut. However, cutting through the whole thickness of the plate may not be suitable for various applications. Evaporated material from the groove settles back onto the surface and creates an opaque thin film that must be cleaned. A way around this is to create just grooves instead of cutting through the whole thickness of the plate. The plate is then broken along these grooves into pieces which are used e.g. as substrates for thin film depositions. The bottom side stays clean and the squares have sharp edges. The quartz glass plate can be divided into rectangles of required dimensions (see **Figure 2**).
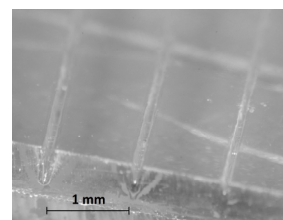
Figure 1 *Grooves in quartz glass*
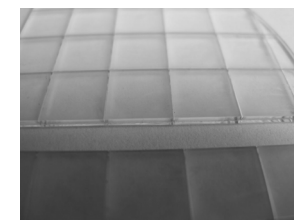
Figure 2 *Grooves in 1.5 mm thick quartz glass plate.*
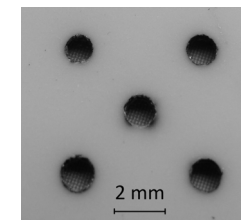
Figure 3 *Holes in a 0.6 mm thick ceramic plate.*
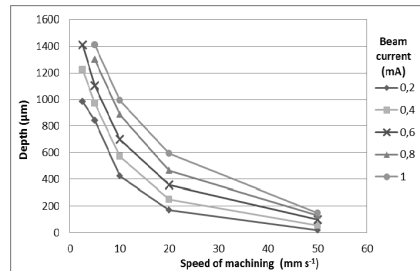
Figure 4 *Dependence of depth on BC and speed in quartz glass*
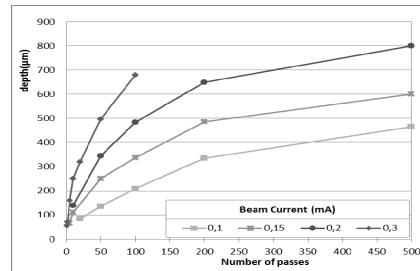
Figure 5 *Dependence of groove depth on the BC and number of passes in ceramics.*

In the case of ceramics, high thermal stress could often lead to the fracture of the plate. To reduce it, a lower beam current and a higher cutting speed could be used. However, this results in lower material displacement. Thus to create a groove of a desired width and depth, multiple passes of electron beam were used. Dependences of groove depth and width on beam current and number of passes were investigated. The speed of the machining was 10 mm·s⁻¹.

As can be seen in **Figure 5**, the maximum groove growth occurs during the first pass. After several more passes the grow rate drops down and the groove deepens only slowly. However, during experiments with an increasing number of pulses, the thermal stress caused cracking of the ceramic plate. To lower the thermal load further, additional pause (0.8 s) was added between each pass of the beam. This allowed the ceramics to cool down and the risk of fracture was reduced to minimum.

The width of the groove grows slowly with the number of passes from 0.15 mm to 0.22 mm for the 0.1 mA beam current and from 0.17 mm to 0.29 mm for the 0.3 mA beam current. This is understandable as the narrow electron beam passes through the upper part of the groove and hits the bottom while only a fraction of energy is lost on the walls. From **Figure 5** it is also apparent that the depth of the groove increases almost linearly with increasing beam current.

While small holes are drilled with a static beam, for larger holes computer controlled deflection can be used. The electron beam then follows the boundary of the future hole. The groove deepens with each pass until the plate is cut through. The inner part is pushed out afterwards. This way, even holes of various shapes can be drilled, although circular holes are the most common. A series of holes with a diameter ranging from 0.5 to 4 mm was created in a 0.6 mm thick ceramic plate. **Figure 3** shows several of these drilled holes.

Acknowledgement

References

[1] VISSER, A. Werkstoffabtrag durch Elektronen-und Photonenstrahlen. Bern: Technishe Runhschau, 1972.
[2] DUPÁK, L, ZOBAČ, M.: Electron Beam Micromachining. In *Proc. Recent Trends (10th seminar).* Brno: ÚPT AV ČR, 2006. p. 15-16. ISBN 80-239-6285-X.
[3] VLČEK, I., et all.: Prototype of desktop e-beam welder MEBW-60/2. *Jemná mechanika a optika,* 2008, vol. 53, no. 1, p. 27-29. (in Czech).
[4] Focus GmbH. *Micro Electron Beam Welder MEBW-60/2* [online]. [cit. 20. 4. 2012]. http://www.focus-gmbh.com/

SURFACE CRYSTALLINITY AT THE SIGHT OF ELECTRONS

L. Frank[*], Š. Mikmeková, F. Mika and I. Müllerová

Institute of Scientific Instruments ASCR, v.v.i., Královopolská 147, 61264 Brno, Czech Rep.
[*]e-mail: ludek@isibrno.cz

Scattering of electrons, injected into solids in order to produce an electron optical image of their surfaces, is governed by the inner potential of the sample with its spatial distribution inherent to the target structure. Except truly amorphous materials of the spatial arrangement range shorter than the interaction volume of electrons, we meet anisotropic scattering with the resulting image signal responding to the local crystalline structure. Incident electrons undergo scattering events the number of which depends on their energy and on the scattering cross section of the material and the final emitted current results from statistics of these events.

With decreasing energy of electrons the scattering anisotropy is known to enhance and become observable on all signals emitted from the sample under bombardment [1]. Fig. 1(a) presents the backscattered electron (BSE) yield η subjected to stronger variations across crystal directions while the secondary electron (SE) coefficient δ as well as the total yield factor σ respond much less. Fig. 1(b) explains the phenomenon showing the backscattering effects more intensive from atomic planes seen as denser by the incident electrons, also with more subsurface events capable of producing the SE. This explanation works until we arrive at electron wavelengths long enough to enable the low energy electron diffraction (LEED) revealing geometry of the surface crystal plane via arrangement of the diffraction pattern. Below few tens of eV, when only the specular (00) spot of the LEED pattern emerges to above the sample surface, we get the spot intensity modulated with the local density of electron states, which is also characteristic for individual atomic planes [2,3].
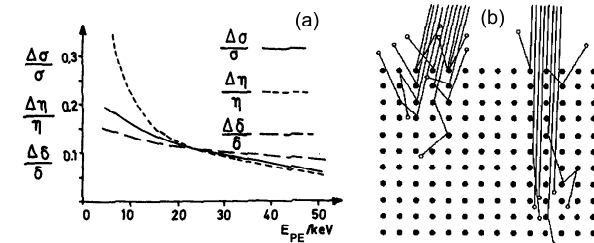
Figure 1 (a) Relative variations in the electron emission from Si (111) (reproduced from [1]); (b) schematics of the electron beam impinging on a crystalline target.

Less known is to what extent the scattering anisotropy effects depend on angular distribution of the primary and signal electron fluxes. At very low energies the diffracted beams carrying the crystallographic information have their directions of movement fixed by relations between the primary beam and reciprocal lattice axes. Above hundreds of eV the BSE emission completely fills the above-surface semisphere with angular distribution that has been only rarely examined, except identification of Kikuchi bands. Two published examples, illustrated in Fig. 2, required nontraditional equipments, namely auxiliary detectors attached to electron

backscatter diffraction (EBSD) assembly or even a tailored multi-detector device [5]. The inserts in Fig. 2(a) indicate the backscatter detector providing the material contrast while the forescatter detector, acquiring BSE emitted under high angles with respect to the primary beam, reveals detailed crystallographic structure. Similarly, the anisotropy of BSE emission visible in Fig. 2(b) is mostly concentrated at scattering angles near and above 90°. Thus, the crystallographic information is expected from BSE emitted at high angles with respect to the incident electron beam.
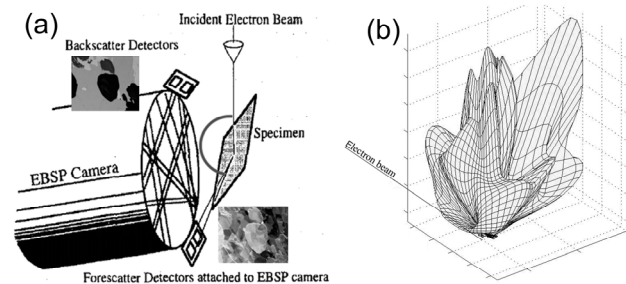
Figure 2 (a) Scheme of an EBSD camera completed with two detecting assemblies acquiring the low angle (with respect to the incident beam) and high angle BSE (reproduced from [4]); (b) angular distribution of BSE between 50 eV and 1 keV for 5 keV primary energy (reproduced from [5]).

Applications in materials science seek efficient tools primarily for two specific tasks: to recognize crystalline grains with different orientation and possibly to identify these orientations, and to visualize distribution of the local internal strain and plastic deformation. The widespread device securing this function in scanning electron microscopes (SEM), the EBSD attachment, fulfills the task but suffers from slow data acquisition and large information volume for a single pixel owing to required large tilt of the sample and the primary energy in tens of keV. For this reason, it is worth exploring the standard electron detectors in the SEM as regards their ability of providing the crystallographic information.

Traditionally, the BSE emission is recorded with coaxially situated detectors above the sample, free of any bias and hence acquiring a hollow cone of the BSE trajectories between polar angles, say, 10° and 40° from the optical axis. The detectable energy of BSE is bottom-limited with the detector sensitivity. When immersing the sample into strong electric field retarding the primary electrons and accelerating and collimating the emitted electrons, we can acquire the complete BSE emission at all energies and emission angles even with a standard single-channel detector [6].

This study is directed to examination of single-channel BSE signals as regards their ability of bearing the crystallographic information in dependence of their emission energies and angles, with the very low energy range discussed in [3]. In Figs. 3 and 4 there are two examples of polycrystalline materials imaged using the cathode lens equipped SEM (CL SEM) with the sample immersed in electric field so that the complete BSE emission except a narrow central ray escaping detection through the central detector bore together with the SE signal.
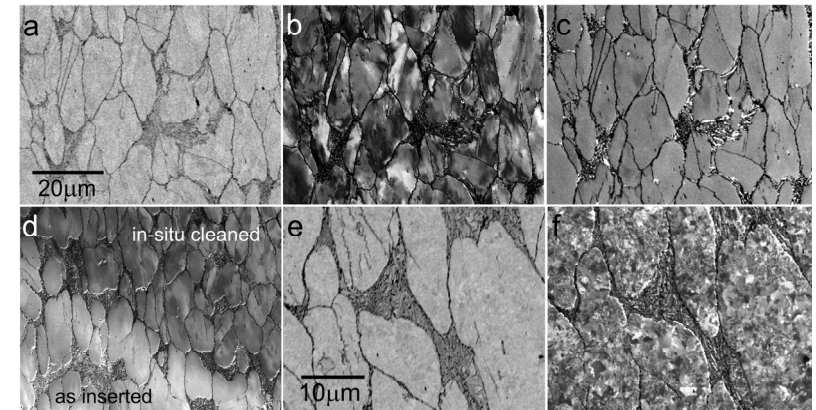
Figure 3 The X210Cr12 steel, heated to semi-solid state at 1265°C, deformed 2:1 at 800°C and cooled, UHV observations: standard BSE image at 6 keV (a), CL SEM images at 500 eV (b) and 50 eV (c); boundary between in-situ cleaned and as-inserted areas (d); annealed at 500°C for 60 min: BSE at 8 keV (e) and CL SEM at 500 eV (f).
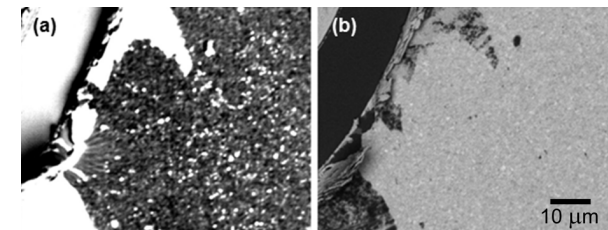
Figure 4 Microcrystalline Cu film on silicon surface: (a) the CL SEM micrograph at 10 eV, (b) standard BSE image at 6 keV.

In Fig. 3 we can compare crystallographic details provided by low angle 6 keV BSE with those available with high angle 500 eV and 50 eV BSE. Obviously, it is just the 500 eV frame that shows even intensive signal variations inside grains, corresponding to lattice deformations either elastic or plastic ones. While superiority of Fig. 3(b) follows from the above discussion, lack of the inner-grain contrast at 50 eV needs to consider the deformations not protruding to the few uppermost atomic layers contributing that image signal. The crystalline layer with sub-μm grains in Fig. 4 exhibits at 10 eV much higher contrast, here coming from the very surface of an in-situ cleaned and under UHV conditions observed sample.

Realizations about the crystallographic contrast growing with decreasing energy of incident electrons and with increasing angle of emission from the surface normal (at normal impact of the primary beam) has been supported with measurement presented in Fig. 5. Results have confirmed the grain contrast intensifying at low energies, with this increase enhanced by the limiting angle of detected BSE growing from 45° at 10 keV to 90° at 2 keV. Further contrast increase is expected toward hundreds of eV.
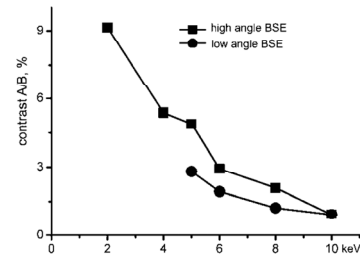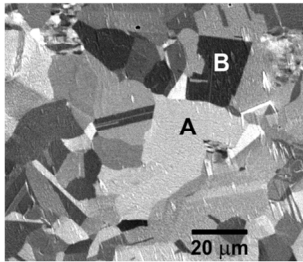
Figure 5 Ultrafine grained Cu relaxed by annealing: contrast between two grains measured in dependence of the impact energy of electrons both in the standard SEM configuration with only low angle BSE detected, and in the CL SEM mode with more complete BSE emission.
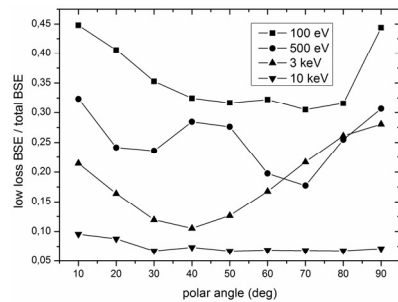
Figure 6 Ratio between simulated yields of low loss BSE (with maximum loss of 50 eV) and the total BSE emissions from Au for intervals of the polar emission angle taken from the surface normal. Simulation software described in [7] was used.

For simulation of the BSE emission no software tools are available that take into account anisotropy of the scattering parameters. The electron scattering is only traced inside a completely amorphous environment. Should the experimental data be confronted with simulated ones, we have to manage with partial simulated factors like the depth of penetration, number of scattering events or energy loss, and to presume from their angular and energy dependences about reasons for the BSE emission around 500 eV providing the optimum crystallographic contrast. First results of this study might indicate the proportion of low loss BSE to be responsible (see Fig. 6). [8]

References

[1] Seiler H. and Kühnle G., Z. Angew. Phys. **29** (1970), p. 254-260.
[2] Jaklevic R.C. and Davis L.C., Phys. Rev. B **26** (1982), p. 5391-5397.
[3] Pokorná Z. et al, Appl. Phys. Lett. (2012), in print; see also this Proceedings.
[4] Prior D.J. et al., Mineralog. Mag. **60** (1996), p. 859-869.
[5] Wagner J. et al., Scanning **27** (2005), p. 298-304.
[6] Müllerová I. and Frank L., Adv. Imaging & Electron Phys. **128** (2003), p. 309-443.
[7] Kieft E. and Bosch E., J. Phys. D, Appl. Phys. **41** (2008), 215310: p. 1 to 10.
[8] Study supported by the Czech Science Foundation under grant no. P108/11/2270.

PERTURBATION THEORY AND SPACE-CHARGE ION DYNAMICS IN ORBITRAP MASS ANALYZER

D. Grinfeld[1*], A. Makarov[1], M. Skoblin, M. Monastyrskiy[2], E. Denisov[1], and A. Neishtadt[3]

[1] Thermo Fisher Scientific, Hanna-Kunath Str. 11, 28199 Bremen, Germany
[2] General Physics Institute of RAS, 38 Vavilov St., 119991 Moscow, Russia
[3] Loughborough University, Dep. Math. Sci., Leicestershire, LE11 3TU, United Kingdom
[*] e-mail: dmitry.grinfeld@thermofisher.com

Introduction. The Thermo Scientific Orbitrap[TM] mass analyzer [1] is based on dynamic confinement the ion motion in the electrostatic axisymmetric potential (the principle was introduced by Kingdon [2] and further developed by Knight [3]):

$$V(z, r) = V_c \frac{k_0}{2} \left(z^2 - \frac{r^2}{2} + r_m^2 \ln \frac{r}{r_m} \right) + const \qquad (1)$$

where r_m and k_0 are geometrical parameters, V_c is the voltage applied to the spindle-shaped electrode 1 in Fig 1A. Two outer *detection* electrodes 2a, 2b are connected to the differential amplifier and readout the current induced by the trapped ion species. The spindle and detection electrodes are machined with submicron accuracy to form equipotential surfaces of the potential distribution Eq. 1. Radial confinement of the trapped ions is guaranteed by the balance between electrostatic attraction to the spindle electrode and the centrifugal force of orbital motion; the ion orbits are restricted between the values r^{min} and r^{max} (Fig. 1B), being the roots of the equation

$$U(r) = 0.5 \, q V_c k_0 [r_m^2 \ln(r/r_m) - r^2/2] + K^2/(2m \, r^2) = E \qquad (2)$$

where $U(r)$ is the rotational pseudopotential with regard to the conserved orbital momentum K, E is radial component of the full energy, and q, m are ion's charge and mass. An important property of the potential (1) is that the frequency of axial motion $\omega = \sqrt{V_c q k_0/m}$ does not depend on the orbital parameters r^{min} and r^{max} and the oscillation amplitude Z, which makes Orbitrap a high-precision Fourier Transform Mass Spectrometer (FT MS), with ultimate mass resolving power restricted by deviation of the real field from the ideal one due to (1) the presence of ion injection aperture and inaccuracies of electrode manufacturing and (2) Coulomb interaction between the ions. The first factor restricts the resolving power for a low number of trapped ions whilst the second factor determines the dynamic range of measured mass spectra. Both factors can be described by the potential perturbation $\varphi(z, r, \psi, t)$ which in practice is significantly smaller than $V(z, r)$ ($\varphi \lesssim 10^{-4} V_c$). However those perturbations become of great concern when it comes to high-precision measurements.

Modeling of the space-charge effects in FT MS by direct ray-tracing of multiple interacting ions represents an exceedingly time-consuming simulation problem which can be addressed only with the use of cluster computers, as described in [4] for Ion Cyclotron Resonance (ICR) and in [5] for Orbitrap analyzers. On the other hand, direct simulation of space-charge effects can hardly allow the accuracy required. An advanced approach is proposed for ICR in [6], where the motion equations are written in the reference system rotating with the Larmor frequency. In the case of Orbitrap analyzers, the electrostatic trapping field $V(z, r)$ can also be excluded using the averaging of fast oscillations (see, e.g. [7]), which leaves only the

perturbation φ in the differential equations to be solved. Apart from allowing the integration time step as big as $\sim (10^2 \div 10^3)/\omega$, the averaging approach gives most comprehensive and demonstrative results in terms of amplitude-phase evolution.
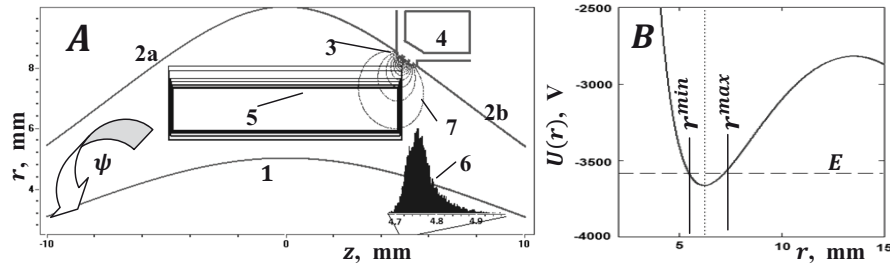
Figure 1. A - Distribution of injected ions. 1 – spindle electrode (V_c = -3.5 kV for positive ions), 2a, 2b – detection electrodes (ground potential), 3 – an aperture for ion injection, 4 – a compensating electrode (potential $V_d > 0$), 5 – areas of ion orbits with different amplitudes and radial constraints, 6 – distribution of z-oscillation amplitudes, 7 – equipotential lines of the field perturbation caused by the injection aperture (3). B – Effective radial potential.

Averaged equations of the oscillatory motion. The Lorentz equations for a system of N interacting ions with masses m_i and charges q_i in the perturbed electric field read

$$\frac{d^2 z_i}{dt^2} + \omega_i^2 z_i = -\frac{1}{m_i} \frac{\partial \varphi(z_1, r_1, \psi_1, \ldots, z_N, r_N, \psi_N)}{\partial z_i}, \qquad \omega_i = \sqrt{V_c q_i k_0 / m_i} \qquad (3)$$

($i = 1..N$) where the (generalized) perturbation potential can be represented by two sums:

$$\varphi = \sum_{i=1}^{N} q_i\, \varphi_s(z_i, r_i, \psi_i) + \frac{1}{2} \sum_{i,j=1}^{N} q_i q_j \varphi_c(z_i, r_i, \psi_i; z_j, r_j, \psi_j) \qquad (4)$$

The function $\varphi_s(\ldots)$ is the potential perturbation that arises from electrodes' non-ideality, and $\varphi_c(\ldots)$ is the potential of the pair-wise Coulomb interaction. In contrast to the z-oscillation frequencies ω_i, the rotational and radial frequencies depend on the parameters K and E, so that the coordinates r and ψ are effectively randomized in the course of multiple oscillations (it takes about 0.25ms as shown in [5]). This fact allows averaging of φ in the 'rings' $0 \le \psi_i < 2\pi,\ r_i^{min} \le r_i \le r_i^{max}$ with the weight $\propto 1/\sqrt{E - U(r)}$ which reflects the time that each ion spends between r and $r + \Delta r$. We further denote the averaged field functions as $\langle \varphi_s \rangle(z)$ and $\langle \varphi_c \rangle(z)$ and omit the arguments r_i^{min}, r_i^{max} for the brevity sake.

Transformation of the motion equations to the amplitude-phase form $z_i = Z_i(t) \cos(\omega_i t + \zeta_i(t))$ opens the opportunity to extend the averaging technique to z-oscillations. The amplitudes $Z_i(t)$ and phases $\zeta_i(t)$ are 'slow' functions of time since the differential equations for them only contain the small terms in the right-hand sides. After the averaging procedure, these equations take the form

$$\dot{Z}_i = -\frac{\omega_i}{k_0 V_c q_i} \frac{1}{Z_i} \frac{\partial \Lambda}{\partial \zeta_i}, \qquad \dot{\zeta}_i = \frac{\omega_i}{k_0 V_c q_i} \frac{1}{Z_i} \frac{\partial \Lambda}{\partial Z_i} \qquad (5)$$

$$\Lambda(Z_1, \ldots, Z_N, \zeta_1, \ldots, \zeta_N) = \sum_{i=1}^{N} q_i \Lambda_s(Z_i) + \frac{1}{2} \sum_{i,j=1}^{N} q_i q_j \Lambda_c(Z_i, Z_j, \Delta \zeta_{ij}), \qquad (6)$$

$$\Lambda_s(Z) = \frac{1}{2\pi} \int_0^{2\pi} \langle \varphi_s \rangle(Z \cos \zeta)\, d\zeta, \qquad \Lambda_c(Z_1, Z_2, \Delta \zeta) = \frac{1}{2\pi} \int_0^{2\pi} \langle \varphi_c \rangle(Z_1 \cos(\zeta + \Delta \zeta), Z_2 \cos \zeta)\, d\zeta \quad (7)$$

where $\Delta \zeta_{ij} = \zeta_j - \zeta_i + (\omega_j - \omega_i)t$ is the oscillation phase difference between two different ions. It is noteworthy that Eqs. 5-6 have the canonical Hamilton form, where the variables conjugate to the phases ζ_i are *actions* $I_i = 0.5 k_0 V_c\, q_i\, Z_i^2/\omega_i$, and the sum of them is conserved. In accordance with Eq. 5, the 'static' term $\Lambda_s(Z)$ alters the oscillation frequencies by the values $\delta\omega_i = \dot{\zeta}_i$ that generally depend on the orbital parameters. The effect of space-charge perturbations is more complicated because the function $\Lambda_c(\ldots)$ depends on the phases ζ_i, which, according to Eq. 5, makes the amplitudes Z_i to evolve as well.

Simulation results. In the simulation example below, we consider two isotopic states of the small peptide (MRFA+H$^+$) (Met-Arg-Phe-Ala), the first one containing two atoms of heavy carbon ^{13}C (m_1=526.2717) and the second one containing one atom of heavy sulfur ^{36}S (m_2=526.2608). The mass difference in the duplet is (m_1-m_2)/m_0= 2.1e-5, where m_0 = (m_1+m_2)/2. The perturbation φ_s resulted from the injection slot is calculated with the use of 3D perturbation technique [8]. The space-charge interaction function φ_c was calculated with the use of the finite-element method. Both functions φ_s and φ_c are averaged in accordance to Eq. 7, and Λ_s and Λ_c are prepared as 1D and 3D splines, correspondingly. The fourth-order Runge-Kutta method with accuracy control is applied to integrate Eq. 5. To reduce the calculation difficulty, the ions of same sorts are combined into fifty macroparticles with multiple charges and masses. The initial distribution of $r_i^{min}, r_i^{max}, Z_i(0)$, and $\zeta_i(0)$ is obtained by means of ion injection simulation using MASIM 3D software.
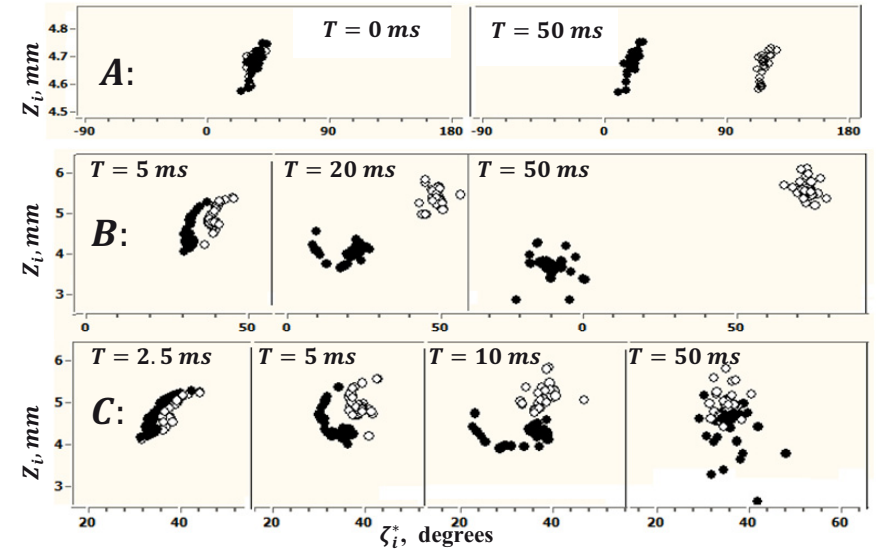
Fig. 2. Coalescence of the MRFA duplet with different total numbers Q of elementary charges: A: Q=1e2, B: Q=8e4, and C: Q=1.2e5.   ○ lighter ions, ● heavier ions.

Fig. 2. shows the evolution of macroparticles in the coordinates (Z_i, ζ_i^*), where $\zeta_i^* = \zeta_i + (\omega_i - \omega_0)t$ is the particle phase reduced to the reference frequency $\omega_0 = \sqrt{V_c q k_0 / m_0}$. In the case of negligible charge (Fig 2A), the particle amplitudes are static but the phase difference increases linearly in time as $\Delta\zeta \sim (\omega_1 - \omega_2)t$, where ω_1 and ω_2 are unperturbed frequencies of lighter and heavier ions in the MRFA duplet. The presence of a considerable charge (Fig. 2B) entails redistribution of energy (and amplitudes) upon the initial phase separation. Indeed, the lighter ions move ahead of heavier ones and gain extra energy from the repulsion force, and vice versa. It is important that the space-charge perturbation also violates the isochronous properties of the z-oscillations: the frequency perturbation $\delta\omega = \dot{\zeta}$ is non-zero and depends on the amplitude. The lighter particles with bigger amplitudes experience negative perturbation $\delta\omega < 0$; and the heavier particles have $\delta\omega > 0$. As a result, $\Delta\zeta$ changes slowly in time. Further evolution of the system qualitatively depends upon the total charge Q. When a certain threshold of Q is exceeded, the space-charge perturbation makes the oscillation frequency of the lighter ions even lower than that of the heavier ones. In this case (Fig. 2C), $\Delta\zeta$ returns to zero, and both ion populations oscillate in one phase.
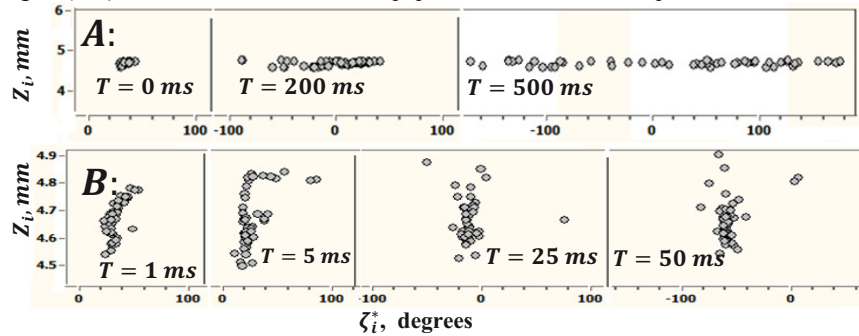
Figure 3. Ion motion (m=526.26) in a 'statically' perturbed field (V_d=1kV). A: Q = 1e2, B: Q = 2e4

In presence of a static perturbation (e.g. generated by the injection slot), dependence of the ion oscillation frequency on the orbital parameters (r_i^{min}, r_i^{max}, and Z) generally leads to the de-phasing of a bunch of even identical ions as shown in Fig. 3A. Presence of a considerable space-charge above a certain threshold makes, however, the entire ion bunch to oscillate in-phase regardless of the 'static' perturbation (Fig. 3B). The self-bunching mechanism is similar to the coalescence: an ion with higher initial oscillation frequency is accelerated to bigger amplitude where its frequency is decreased by the space-charge interaction with the others.

References

[1] Makarov A., Denisov E., Lange O., J. Am. Soc. Mass. Spec **20** (2009), p. 1391–1396
[2] Kingdon K.H., Physical Review, **21 (4)** (1923), p. 408 – 418.
[3] Knight R.D., Applied Physics Letters **38 (4)** (1981), p. 222 – 223.
[4] Leach F.E., Kharchenko A., et al., J. Am. Soc. Mass. Spec. **21 (2)** (2010), p. 203–208
[5] Kharchenko A., et al., J. Am. Soc. Mass. Spec. **23 (5)** (2012), p. 977–987
[6] Mitchell D.W., Smith R.D., Physical Review E **52** (1995), p. 4366 – 4386.
[7] Nayfeh A.H., Perturbation Methods (1973), Wiley-Interscience, NY
[8] Greenfield D., Monastyrskiy M., Selected problems of computational charged particle optics. Ch.3. (2009), Elsevier Press, In: Adv. in imaging and electron physics, **155**, Ed: P. Hawkes

A SECOND-ORDER FOCUSING PARALLEL ACQUISITION RADIAL MIRROR ENERGY ANALYSER FOR THE SCANNING ELECTRON/ION MICROSCOPE

H. Q. Hoang[1]* and A. Khursheed[2]

[1]Centre de Recherche Public-Gabriel Lippmann, 41 rue de Brill, L-4422 Belvaux Luxembourg
[2]National University of Singapore, 4 Engineering Drive 3, Singapore 117576
*e-mail: hoang@lippmann.lu

Wide range parallel energy detection of charged particles to speed up spectrometer data-acquisition times is already well known. The previous wide range parallel energy analyzers such as the Parallel Cylindrical Mirror Analysers (PCMA) [1] and the Hyperbolic Field Analyser (HFA) [2, 3], however, have first-order focusing property, resulting in low transmittance for a given energy resolution. Recently, a Radial Mirror Analyzer (RMA), designed as an attachment for inside the specimen chambers of SEMs has been reported [4]. The analyzer is predicted to have a relatively high energy resolution-transmittance performance arising from its second-order focusing properties and a relatively large bandwidth in its parallel energy mode of operation, over 12% of the central pass energy. This paper aims to design a wide-range parallel RMA (referred to as the PRMA) for use inside scanning electron/ion microscopes, one that is capable of capturing energies that vary by several orders of magnitude, while still maintaining the RMA's second-order focusing properties on the detection plane.

Figure 1 shows a simulated design of the PRMA for scanning electron/ion microscopes in the Lorentz program [5] together with simulated ray paths through it. The analyzer is rotationally symmetric through the vertical axis of the primary beam column. It has an outer zero volt plate, conical in shape on the top so that it fits under the lower pole-piece of a scanning electron/ion microscope objective lens. The first series of deflector plates within the analyzer are eleven conical electrodes at different potentials, followed by a main top deflector plate, biased to V_D. In the recent design, these electrodes are biased at voltages given by the following values (in volts): V_D = -2643, V_1 = -17, V_2 = -88.1, V_3 = -208.3, V_4 = -320.4, V_5 = -480.6, V_6 = -688.9, V_7 = -929.2, V_8 = -1249.6, V_9 = -1441.8, V_{10} = -1521.9, and V_{11} = -1762.2. A grounded conical grid, inclining 17° with respect to the horizontal axis, is used to form the bottom of the analyser through which the scattered electrons/ions enter and escape from the analyser. For simplicity, the grid is approximately to be an ideal equipotential plane in this simulation.

Scattered electrons/ions leave the specimen located below the analyzer on its rotational plane of symmetry (primary beam axis), they enter the analyzer through the grid and are mirrored down by negatively biased electrodes, and are then brought to focus on a horizontal flat plane detector as illustrated in Fig. 1. Simulation results show that second-order focusing occurs for all the energies from 100 to 5000 eV along the horizontal detection plane, resulting in high energy resolutions for a given transmittance. An ideal HFA has been also simulated in order to perform a comparison with the PRMA design. An energy resolution comparison between the two designs is shown in Table 1. It is clear that for the same polar angular spread (±3°),

the energy resolution of the PRMA is improved by about an order of magnitude compared to the ideal HFA for most of the energy range. Note that a planar version of the PRMA (like the HFA design) with the same electrode arrangement can be made, showing similar results to the rotationally symmetric version. More detail of the design will be presented at the conference.
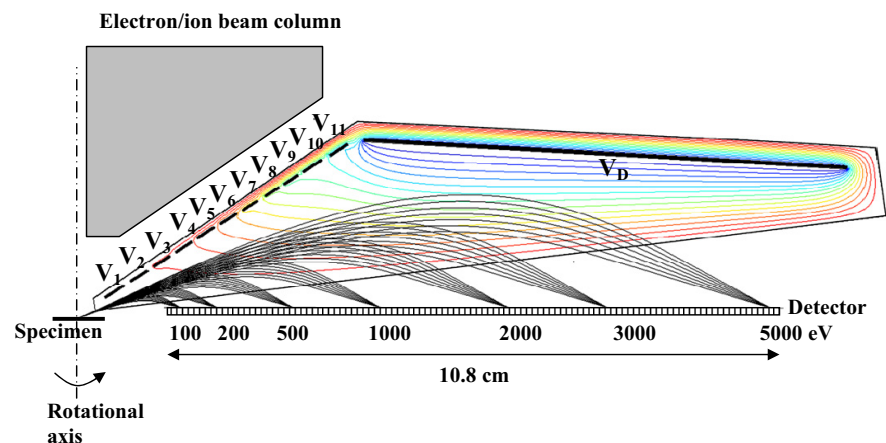
Figure 1. Simulated trajectory paths through a second-order focusing PRMA design at the energies 100, 200, 500, 1000, 3000 and 5000 eV. For each energy, seven trajectories are plot evenly between -3° to 3° around a 24.6° polar entrance angle.

	Simulated relative energy resolution (%)	
Energy (eV)	PRMA ($\Delta\theta = \pm 3°$)	HFA ($\Delta\theta = \pm 3°$)
100	0.647	1.685
200	0.313	2.197
500	0.185	2.246
1000	0.145	1.862
2000	0.144	1.63
3000	0.133	1.497
5000	0.120	1.337

Table 1. Simulated energy resolution comparison of the PRMA and the HFA

References:

[1] F. H. Read, Rev.of Sci. Instrum. **73** (3) (2002) 1129-1139.

[2] M. Jacka, M. Kirk, M. M. El Gomati, and M. Prutton, Rev. of Sci. Instrum. **70**, (1999) 2282-2287.

[3] D. Cubric, A. De Fanis, I. Konishi, and S. Kumashiro, Nucl. Instrum. Meth. Phys. Res. A **645** (2011) 227-233.

[4] H. Q. Hoang and A. Khursheed, Nucl. Instrum. Methods Phys. Res. A **536** (2011) 64-68.

[5] Lorentz - 2EM, Integrated Engineering Software Inc, Canada.

THERMAL-FIELD ELECTRON EMISSION W(100)/ZrO CATHODE: FACETS VERSUS EDGES

F. Matějka[1], M. Horáček[1*], V. Kolařík[1] and M. Matějka[1]

[1]Institute of Scientific Instruments AS CR, Královopolská 147, 61264 Brno, Czech Republic
*e-mail: mih@isibrno.cz

The tungsten cathode in the thermal-field emission (TFE) regime can achieve significantly higher angular current density in comparison with the Schottky cathode. The Schottky emission regime is located between the thermal emission regime and the cold field emission regime. The typical operation electric field is 0,1 - 1 V/nm and tip radius varies from 0.3 to 1.0 µm [1,2]. The thermal-field regime is located between the Schottky regime and the cold field emission regime. In the cold field emission regime the electron tunnelling is a dominant mechanism due to the electric field higher than 1 V/nm. The TFE is a combination of the field supported thermal emission and the field emission under the higher electric field. The radius of the thermal-field emitter should be lower in comparison with the Schottky emitter [3,4].

The activated tungsten single-crystal etched tip is typically used for Schottky and field electron emitter. The top of the tip is made of one of the chemically active facets, nowadays commonly (100). The aim of the activation is to reduce the work function, hence to increase the total emission current in comparison with the low temperature field emitter. A typical activation process uses Zr and O_2 influence under high temperature. The tip radius of the Schottky cathode is purposely increased after the activation up to 1 µm. As a consequence, the electric field intensity on the tip is lower, the potential barrier is wider thus the electron tunnelling is lower. Ergo, the electron energy spread is nearly as lower as for the cold field emission regime. Next, the higher radius results in the larger emission surface; more atoms of the surface emit the electrons so the noise is lower in comparison with the field emission regime. The spherical surface of the tip made after the etching is changing during activation process and next during the stabilization of the cathode emission. The facets grow on the tip with the (100) facet on the top. The higher field at the edges between the facets accounts for the nonhomogeneous emission distribution. In the case of the Schottky emitter with higher radius the ring-shaped emission distribution with rather large area homogeneous central circle is typical [1,2]. In the case of the sharper TFE emitter (Fig. 1) the electric field at the central facet edges is much higher than on the axis (Fig. 2), the simulations are based on the approach used in [5]. The emission from the edges is dominant and the emission pattern is nonhomogeneous (Fig. 3 left) which corresponds to the crystallography of the emitter tip (Fig. 3 right) [6].

References:

[1] K. Liu et al., J. Vac. Sci. Technol. B **28**(6) (2010) p. C6C26-C6C33.

[2] Swanson L.W., Schwind G.A., Handbook of Charge Particle Optics, Second Edition, Jon Orloff, CRC Press 2008.

[3] Matejka F. et al., 12th Seminar Recent Trends in CPO and SPI, Brno (2010) 13.

[4] Matejka M. et al., 12th Seminar Recent Trends in CPO and SPI, Brno (2010) 29.

[5] Radlička T., Lencová B., Nucl. Instrum. Method, 645(1), 124-129.

[6] This research was supported by MIT CR (TIP project FRTI1/576), by EC and MEYS CR (project CZ.1.05/2.1.00/01.0017), by AV0 Z20650511 and by RVO 68081731.
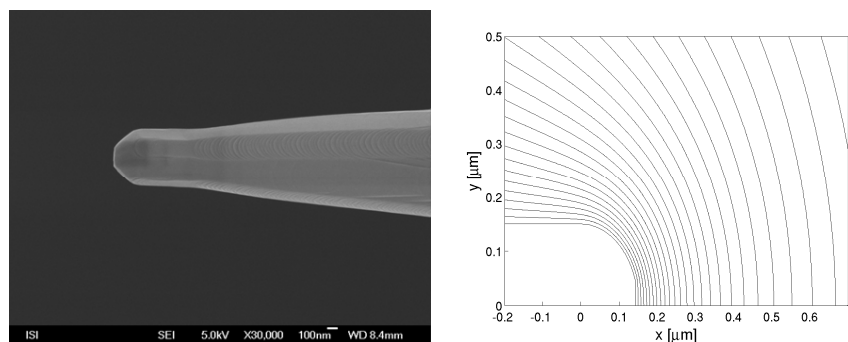
Figure 1 SEM image of the emitter shape (left) and 2D simulation of the electric field for tip radius 150 nm, central (100) facet size 90 nm, tip-anode distace 3 mm and tip-anode voltage 15 kV (right).
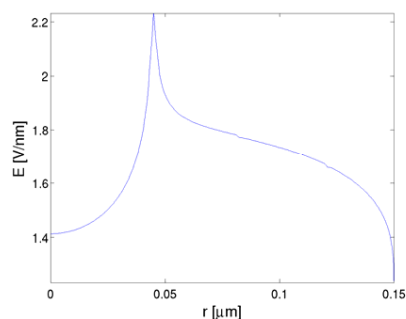
Figure 2 Emitter surface field versus radial/axis distance for electric field simulation in Fig. 1 (right).
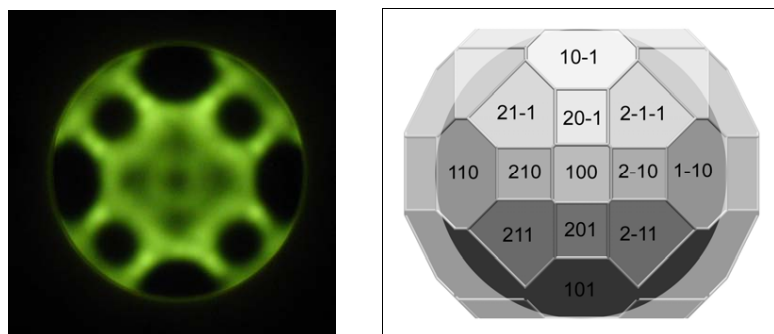
Figure 3 Emission pattern of the emitter (left) and probable model of the end form shapes of the emitter tip (KrystalShaper software).

APERTURES WITH NON CIRCULAR HOLES - A KEY TO ABERRATION CORRECTION IN MULTI COLUMN / MINIATURIZED E-BEAM SYSTEMS?

R. Janzen[1]

[1]Laboratorium für Elektronenmikroskopie, Karlsruher Institut für Technologie (KIT), Engesserstr. 7, D-76131 Karlsruhe, Germany
e-mail: info@dr-janzen.de

Charged particle optics is a continuously developing and expanding technology with a meanwhile broad area of applications.

Unfortunately aberrations limit the performance of nearly all particle optical applications. In the highly sophisticated area of electron microscopy correctors are meanwhile commonly used. Hexapole correctors are state of the art and are continuously advanced by the experts at CEOS Company in Germany.

Nowadays charged particle optics finds its way into miniaturized applications. Whereas miniaturized columns including mini lenses exist, the commonly used correctors are too complex for a use in miniaturised single or multicolumn systems. Nevertheless the correction strategies of electrostatic aberration correctors may be transferred to such systems.

The key is the fact that a hole with n-fold shape within an aperture separating two electric fields with different strengths produces a superposition of a round lens field and a 2n-pole field (plus more or less higher order terms depending on the shape).

In simple terms all that has to be done in order to use such multipole fields for reduction / correction of aberrations, is to pile up apertures with specially shaped holes on adequate voltages in a sophisticated way. The formula how to use which fields may carefully be transferred from working corrector designs.

The method doing so will be denoted by SPANOCH (**S**ophisticated **P**ile of **A**pertures with **no**n **c**ircular **H**oles) in the following, indicating that it uses apertures with non circular holes in order to produce multipole fields (for correction purposes). Using SPANOCH one faces native difficulties:

- The coupling of the multipole fields with additional round lens fields.
- The coupling of the field strengths with distances and voltages of the apertures (leading to velocity changes).

So far apertures with twofold and threefold shapes have been investigated by computer simulation. The results for the apertures with twofold shaped holes were:

- By designing the twofold shape of the hole in an adequate way an additional oktupole field can be added to the desired quadrupole. Its strength can be chosen out of a wide range of positive and negative values.
- The strength of the quadrupole field depends directly on the bigger diameter of the shape.
- The ratio of the strength of the quadrupole and that of the associated round lens field can be made suitable for the use in an electrostatic corrector for chromatic aberration.

Apertures with threefold shaped holes were used to build up a first test setting to demonstrate the SPANOCH concept and its proof of principle in computer simulation: An electrostatic analogue of the commonly used hexapole Cs-correctorr was composed as a SPANOCH

design. Therefore two identical hexapoles and round lenses were created that way that the mid plane of the first hexapole was imaged into the mid plane of the second one and the intermediate image plane became a symmetry plane of the entire assembly.

The assembly based upon this principle is depicted in figure 1. It was generated using a computer simulation procedure based on the charge simulation method.

Results: The hexapole strengths of single apertures having holes with a threefold shape, denoted by hexapole apertures in the following, showed to be too small. Building up a corrector yielding negative values of C_s succeeded by using duplets of hexapole apertures.
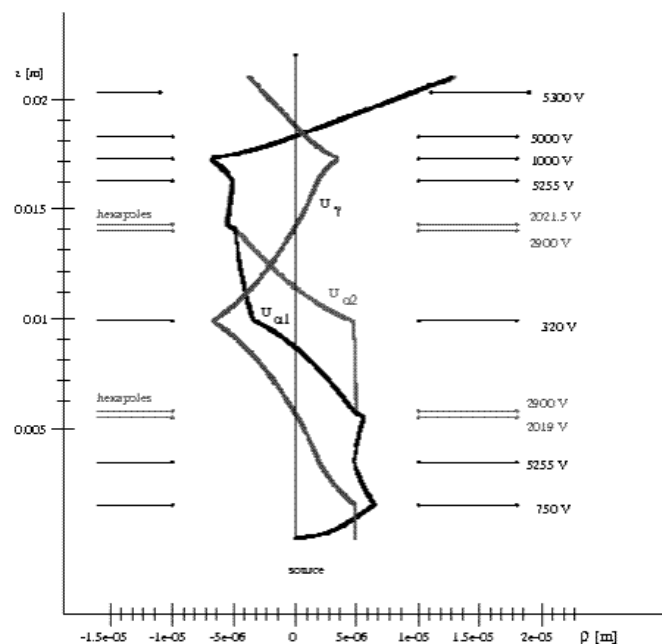
Figure 1: Positions and optimum voltages of the apertures and course of the (numerical) fundamental rays within an example system of the electrostatic C_s-mini corrector. $U_{\alpha 1}$ and $U_{\alpha 2}$ differ in the area between the hexapole apertures because the azimuth of their starting angle differs by 60 degrees.

Summary and outlook: Specially shaped holes in piled up apertures on suitable potentials were found out to produce electrostatic quadrupole, hexapole and octupole fields that were (partially) demonstrated by computer simulation to be suitable for correction purposes in miniaturized particle optical multi column systems. Further investigations have to reveal if requirements concerning alignment and fabrication tolerances can be fulfilled.

IMPROVING RESOLUTION AT LOW VOLTAGES IN A NOVEL FE-SEM COLUMN WITH BEAM DECELERATION TECHNOLOGY

J. Jiruše*, F. Lopour, M. Havelka

TESCAN a.s., Libušina třída 21, 623 00 Brno, Czech Republic
*e-mail jaroslav.jiruse@tescan.cz

The scanning electron microscopy (SEM) at low voltages is advantageous for the investigation of non-conductive materials, semiconductors, polymers, biological samples or lithographic resists susceptible to the radiation damage. They allow a microscope user to determine very fine surface details that cannot be observed at high voltages. The best resolving power of commercial instruments is about 1 nm for Schottky type of field-emission SEM, typically achieved at high voltages 15-30 kV, whereas it is in principle inferior at low voltages due to increased chromatic aberration.

One of the suggestions for improving SEM performance at low voltages is to keep the electron beam at a higher energy through the column and decelerate it to the final energy by applying a negative voltage on the sample in a cathode lens [1]. In this case the secondary electrons (SE) are accelerated by the same negative sample bias and they have to be detected in similar way as the high energy backscattered electrons (BSE). In a standard BSE detector below the final pole piece the central hole for the primary beam has to be very small (typically 0.3 mm), thus limiting the observable field of view. Further, there are high demands on alignment. Thus integrating a suitable detector inside the column is a necessary step towards a comfortable use of this method.

A novel column of MIRA3 model 2012 Schottky field-emission SEM of TESCAN incorporates the beam deceleration together with a possibility to detect BSE electrons in the column and to probe samples with high currents up to 200 nA for analytical applications. The principle called Beam Deceleration Technology (BDT) is shown in Fig. 1. The primary electrons, that leave the objective lens with higher energy, are decelerated by sample bias just before landing on the specimen surface. Optical aberrations are lowered and the resolution is improved compared to the case where the primary beam would have the landing energy throughout the whole column; the resolution for 1keV landing energy is improved from standard 3.5 nm to 1.8 nm with BDT. Moreover, the minimum landing energy is pushed below 100 eV. The secondary electrons are accelerated and focused inside the electron column in the direction of the optical axis. Therefore, they cannot be detected by a conventional SE detector. A configuration with the detector placed inside the electron column, where high efficiency scintillator YAG:Ce is used, proved to be optimal for reaching the excellent SE signal.

The very same system can also be used for the detection of backscattered electrons in the standard mode where the sample is grounded. This so-called In-Beam BSE detector is of great practical value. Standard in-chamber BSE detector placed just below the SEM pole-piece limits the minimal working distance significantly. The new In-Beam BSE detector breaks this limitation and allows achieving an arbitrarily low working distance. In addition, the location of the detector further from the sample enables to detect high angle BSE while in-chamber detector accepts mainly low-angle BSE, thus the two detectors collect complementary signals and, if necessary, both signals can be acquired simultaneously. Moreover, removing the BSE

detector from the vicinity of the sample substantially increases free working space for other analytical methods. In-Beam BSE detector is a natural complement to older In-Beam SE detector [2].

Accurate calculations of working distances, magnification and all other optical parameters are performed using the state-of-art In-Flight Beam Tracing[TM]. This unique method of calculations, developed and implemented since TESCAN very first FE-SEMs, now extends to an accurate tracing of the BDT, and it achieves the precision typically an order of magnitude better than the semi-analytical approach in [3].

All this instrumentation was applied also in LYRA3 combined FIB/SEM tool of TESCAN. Users are benefited with In-Beam SE, In-Beam BSE plus SE in BDT detectors in addition to in-chamber SE an BSE. In-Beam detectors enable to free the working space in the vicinity of the sample, which plays an important role in complex multi-techniques apparatus, combining FIB-SEM-GIS-EDX-EBSD-CL-TOF [4].

References:
[1] Müllerová I and Lenc M., Ultramicroscopy **41** (1992), p. 399-410.
[2] Jiruše J. and Lopour F., Patent CZ 298 912.
[3] Zobačová J. *et al*, Scanning **28** (2006), p. 155-163.
[4] Jiruše J., in Proceedings Next Generation Solar Energy, Schloss Erlangen (2011).
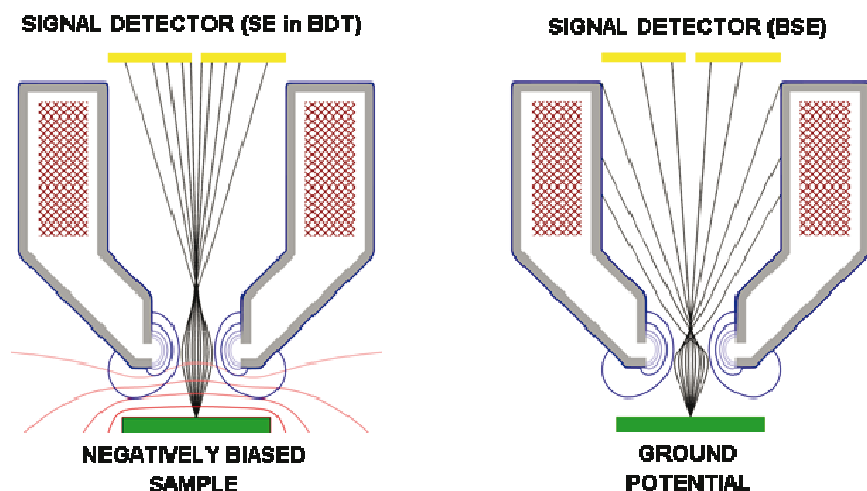
Figure 1 Left: Beam Deceleration Technology configuration where the electron detector inside the column detects secondary electrons. Right: Standard configuration where the sample is grounded and back-scattered electrons are detected.

A WIDE-RANGE PARALLEL MAGNETIC ENERGY ANALYZER FOR SCANNING ELECTRON MICROSCOPES

K.H. Cheong* and A. Khursheed

Dept. of Electrical and Computer Engineering, National University of Singapore, Block EA, #06-10, Singapore, 117576.
*e-mail: g0800484@nus.edu.sg

Cubric *et al* [1] recently showed that it is possible to acquire the Auger electron spectrum using a parallel electron energy analyzer in the HV environment of a SEM for a short period of time after cleaning the specimen surface by ion bombardment. This is possible because data acquisition times for parallel energy detection can be in the order of milliseconds, compared to serial mode acquisition, which is typically in the order of minutes. Cubric *et al* used the Hyperbolic Field Analyzer (HFA), designed to capture electron energies that typically range from 50 to 2500 eV [2]. The HFA has a relative energy resolution of 0.8% at 100 eV and 0.16% at 2500 eV [2] for entrance angles of $\pm$ 1.1° in both the polar and azimuthal directions, giving an overall low transmittance of less than 0.05%. It functions by using a planar analytical electric field distribution and is characterized by first-order focusing optics with second-order focusing properties at a single energy (100 eV) [3]. Khursheed presented a wide-range parallel analyzer design based upon the use of field variations within a magnetic sector box unit, simulated by using a three-dimensional magnetic scalar potential numerical model [4]. He predicts this analyzer to have a transmission of 5 times better than the HFA (for approximately the same energy resolution) and an average relative energy resolution of 0.33% (minimum of 0.147% and maximum of 0.622%) for a polar angular spread of $\pm$ 3°.

This paper presents improvements in the Khursheed parallel magnetic box energy analyzer design, and is simulated using magnetic vector field distributions in three-dimensions which take into account the property of materials, as well as fringe field effects at the entrance slit. The relative energy resolution is predicted to lie below 0.1% at a polar angular spread of $\pm$ 3° across its entire energy range of 50 to 2500 eV. In order to achieve this, a damped least-squares technique was used to optimise the energy resolution at selected energies. A conical upper part to the analyzer is used to allow for shorter working distances. A detection system consisting of a parallel array of channeltrons is proposed, whose individual heights can be adjusted. The relative energy resolution of the present parallel magnetic box analyzer design is predicted to be better than the HFA by over an order of magnitude.

References
[1] D. Cubric, A. De Fanis, I. Konishi, S. Kumashiro, Nuclear Instruments and Methods in Physics Research Section A: Accelerators, Spectrometers, Detectors and Associated Equipment **645** (2011), 227-233.
[2] M. Jacka, Journal of Electron Spectroscopy and Related Phenomena **114-116** (2001), 277-282.
[3] M. Jacka, A. Kale, N. Tratler, Review of Scientific Instruments **74** (2003), 4298-4300.
[4] A. Khursheed, Journal of Electron Spectroscopy and Related Phenomena **184** (2011), 57-61.

(a)

(b)
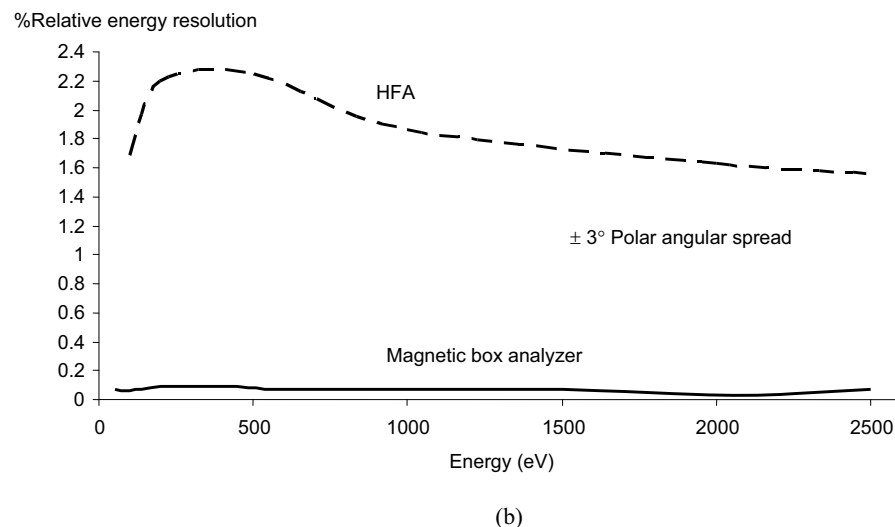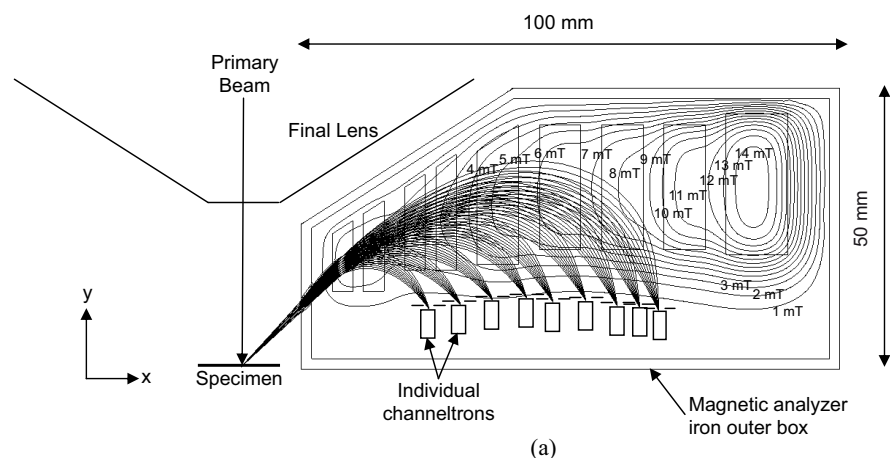
Figure 1. Simulated characteristics of the wide-range parallel magnetic box energy analyzer
(a) Simulated electron in-plane trajectory paths for emission energies of 0.05, 0.1, 0.2, 0.4, 0.6, 1, 1.5, 2 and 2.5 keV where the polar angular spread uniformly ranges between -3° and +3°. B_z contours on the central odd-symmetry plane are plot between 1 and 14 mT in steps of 1 mT.
(b) Predicted relative energy resolution as a function of energy in comparison with the HFA at a polar angular spread of ± 3°

NANO EMITTER RING ARRAY FOCUSED ELECTRON BEAM COLUMNS

A. Khursheed

Dept. of Electrical and Computer Engineering, National University of Singapore, Block EA, #06-10, Singapore, 117576.
eleka@nus.edu.sg

Promising field emission characteristics have been reported for a wide variety of vertically aligned patterned nanotube arrays. Some use a regular rectangular array of carbon nanotube (CNT) dots [1], while others form densely packed block/ mesh CNT structures [2]. Emission currents ranging from 0.3 to 30 nA per CNT dot have been measured experimentally. Large area field emitters of this type are usually discussed only in relation to applications such as flat panel displays. However, in this proposal, a focused electron beam column design using nanotube field emitter ring arrays is presented. Simulation results indicate that these kinds of columns will be able to focus several tens of micro-amperes of current into probe diameters that measure only a few tens of nanometers. This combination of high brightness and high total probe current is expected to have significant advantages over conventional single-tip field emitter focused electron beam systems.

The basic principle of the method is illustrated in Figs. 1a-c. Electrons leave the emission plane from off-axis points, are accelerated through a common anode, and form a virtual source spot as they exit the gun unit with relatively small angles. A weak electric lens in the gun unit helps to reduce their angular spread. It turns out that for points either on or close to a certain emission radius, field curvature and astigmatism aberrations generated within the gun unit cancel out with corresponding aberrations generated in the objective lens, greatly reducing the final probe size, this is illustrated by the simulation results shown in Figs 1e and 1d. For the example gun/lens column shown in Fig. 1, nano-emitters having a radius of 152 μm with emission angles ranging from -100 to 100 mrad, are predicted to generate a RMS probe radius of 10 nm. Assuming that the emitter consists of 0.1 μm diameter CNT dots arranged next to one another around the circumference of a 152 μm radius ring, current from 9550 emitters will reach the specimen. This gives a total predicted probe current of 9.55 μA assuming that there is 1 nA emission current per CNT dot. Although only one focusing lens is required beyond the gun unit, it is useful to add an intermediate point of focus at which an aperture can filter the angular spread, as shown in Figs 1b and 1c.

References:
[1] S. Lacobucci *et al*, Applied Physics Letters **100**, 053116 (2012)
[2] C. Li *et al*, Applied Physics Letters **97**, 113107 (2010)
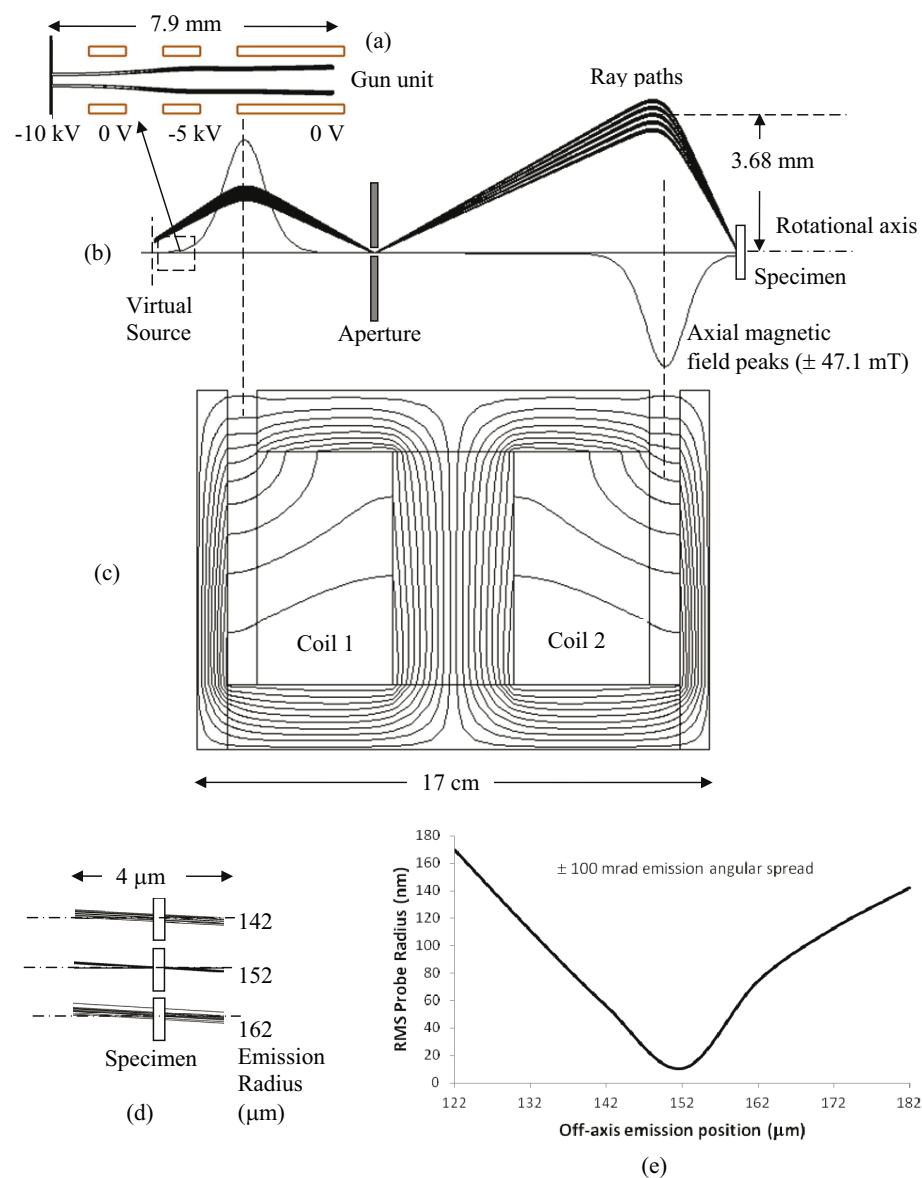
Figure 1. Simulated characteristics of a ring emission electron beam column design
(a) Direct ray tracing in the gun unit for ring-radii of 132 to 172 μm in steps of 10 μm
(b) Direct ray tracing in column (c) Flux lines for the magnetic lens (d) Ray paths around the
specimen plane (e) Predicted RMS probe radius as a function of emission radius

WHAT IS THE BUZZ ABOUT THE TZ MODE

V. Kolařík, F. Matějka, M. Matějka, M. Horáček, M. Urbánek, J. Bok, S. Krátký. S. Král,
F. Mika

Institute of Scientific Instruments of the ASCR, v. v .i., Královopolská 147, 612 64 Brno, CZ
E-mail: kolariQ@isibrno.cz

This contribution deals with an e–beam pattern generator BS 600 that works with a variable rectangular spot of electrons (stamp). The TZ stands for the 'technology zoom'; its meaning is a reduction of the spot size by a factor of 3. Original description of the TZ exposure mode can be found in [1], [2] and [3]; further aspects concerning the exposure system and its electron source were described in [4] and [5]; technology and related topics are discussed in [6], [7], [8] and [9]; overview of application areas is in [10], [11] and [12]; and finally, very recent results are summarized in [13], [14] and [15].

Key factors of the TZ exposure mode are as follows:

- higher exposure speed due to (9 times) increased beam current density;
- finer stamp size adjustment (stamp size step is reduced from 50 nm to 17 nm);
- sharper stamp shape due to the stronger shaping aperture size reduction.

On the other hand, several drawbacks of the TZ exposure mode are to be noticed. The total exposure could be regarded to as the ordered stamp list: $E = \{E_i\}$, where each individual stamp is basically defined by its position / stamp size / exposure time triplet: $E_i = \{C_i; S_i; t_i\}$. The strategy for data preparation (stamp size selection, stamp list ordering, proximity effect correction, etc.) is to be approached differently than it was in the standard mode; major challenge is related to the fact that in parallel with the stamp size reduction, the stamp shape is rotated by -45° (*cf.* Figure 1, where a rectangle of 10 × 6 um2 is filled by 15 2-by-2-um adjacent stamps in the standard mode; this rectangle is overprinted by 15 TZ-mode stamps). Besides the data preparation, a distinct configuration is necessary for the column adjustment and the correction of the deflection–field distortion. Anyway, the improvement of the exposure resolution and the writing speed is prominent.
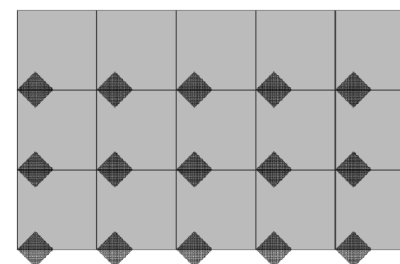
Figure 1 Schematics of a 5×3 stamp area (standard mode and TZ mode).
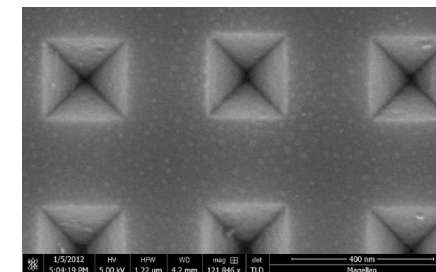
Figure 2 Detail of a calibration specimen: cross grating with a period of 463 nm.

The TZ exposure mode gives a large potential in new application areas. As an example, Figure 2 shows a detail of a calibration specimen for SEM adjustment consisting of a cross grating with a period of 463 nm: the data were prepared using the proximity effect correction method for shaped electron beam, the pattern was exposed in the TZ exposure mode, standard technology resist development, anisotropic Silicon etching process and thin film Platinum sputtering. It might be noticed that even the shape of exposure stamps was rotated WRT to the deflection coordinates; the anisotropic etched artefacts reflect the crystallography of the Silicon substrate with $\langle 100 \rangle$ orientation.

References:

[1] V. Kolarik, Towards the Sub-100nm E-beam Writing System. In Abstract booklet of the NANO '05 Conference. Brno: VUT, 2005. p. 116. ISBN 80-214-3044-3.

[2] V. Kolarik *et al.*, Writing System with a Shaped Electron Beam. *Jemná mechanika a optika*, **Vol. 53**, **No. 1** (2008), pp. 11–16, ISSN 0447–6441 (*in Czech*).

[3] F. Matějka *et al.*, Reducing the Size of a Rectangular-Shaped Electron Beam in E-Beam Writing System. Proc. of the 8th Multinational Congress on Microscopy. Prague: CMS. 2007. pp. 87-88. ISBN 978-80-239-9397-4.

[4] V. Kolarik *et al.*, Nanolithography and Magnetic Field Cancellation in the Industrial Area. *Jemná mechanika a optika*, **Vol. 56**, **No. 11-12** (2011), pp. 312–316, ISSN 0447–6441 (*in Czech*).

[5] F. Matejka *et al.*, Modification of the Schottky Fe ZrO/W Electron Emitter. *In Proc. of 12th Int'l Seminar on Recent Trends in CPO*. Brno: ISI AS CR, 2010, pp. 13-14. ISBN 978-80-254-6842-5.

[6] M. Matejka *et al.*, Comparison of Techniques for Diffraction Grating Topography Analysis. *In Proc. of 12th Int'l Seminar on Recent Trends in CPO*. Brno: ISI AS CR, 2010, pp. 29-32. ISBN 978-80-254-6842-5.

[7] M. Urbanek *et al.*, Determination of Proximity Effect Forward Scattering Range Parameter in E-beam Lithography. In Proc's of the 12th Int'l Seminar on Recent Trends in CPO. Brno: ISI AS CR, 2010 pp. 67-68. ISBN 978-80-254-6842-5.

[8] M. Matejka *et al.*, Scanning Probe Microscopy: Measuring on Hard Surfaces. NANOCON 2011. 3rd Int'l Conference. 2011, pp. 701-704. ISBN 978-80-87294-27-7.

[9] M. Urbanek *et al.*, SPM Nanoscratching in the Sub 100 nm Resolution. NANOCON 2011. 3rd Int'l Conference. 2011, pp. 213-217. ISBN 978-80-87294-27-7.

[10] J. Kettle *et al.*, Fabrication of Poly(3-Hexylthiophene) Self-Switching Diodes using Thermal Nanoimprint Lithography and Argon Milling. *Journal of Vacuum Science & Technology B*, **Vol. 27**, **No. 6** (2009), pp. 2801-2804. ISSN 1071-1023.

[11] V. Kolarik *et al.*, Institute of Scientific Instruments: An Overview Presentation. In Proc's of 21st Int'l Conference on Metallurgy and Materials. 2012. p. 28. ISBN 978-80-87294-29-1.

[12] M. Horacek *et al.*, Thin Metallic Layers Structured by E-beam Lithography. In Proc's of 21st Int'l Conference on Metallurgy and Materials. 2012. p. 68. ISBN 978-80-87294-29-1.

[13] J. Bok et V. Kolarik, Measurements of Current Density Distribution In E-beam Writer, *In Proc. 13th Int'l Seminar on Recent Trends in CPO*. Brno: ISI AS CR, 2012.

[14] M. Matejka *et al.*, Proximity Effect Simulation for Variable Shape E-beam Writer. *In Proc. 13th Int'l Seminar on Recent Trends in CPO*. Brno: ISI AS CR, 2012.

[15] F. Matejka *et al.*, Thermal-Field Electron Emission W(100)/ZrO Cathodes: Facets versus Edges, *In Proc. 13th Int'l Seminar on Recent Trends in CPO*. Brno: ISI AS CR, 2012.

ANOTHER DEVELOPMENT IN ELECTRON OPTICAL DESIGN PROGRAM

J. Zlámal[1*], B. Lencová[1,2*]

[1] Institute of Physical Engineering, Faculty of Mech. Eng., Brno University of Technology, Technická 2, 61696 Brno, Czech Republic
[2] TESCAN a.s., Libušina třída 21, 623 00 Brno, Czech Republic
*e-mail: zlamal@fme.vutbr.cz or lencova@fme.vutbr.cz or bohumila.lencova@tescan.cz

Electron Optical Design (EOD) program has reached maturity, and the improvements seem to be rather marginal [1]. Some editing menus slightly changed, new options were added. However, as the development in compiler technology and in operating systems goes on, we have to keep pace with it. It is often not trivial to change the compiler, because there are some changes, e.g. in memory management, that cannot be solved by simply recompiling the program and the plugins.

The biggest obstacle in getting correct results is the user. The typical problems are that he/she specifies the geometry of the design (the coarse mesh) by using a mesh with a low number of coarse mesh lines, and on top of it using too few mesh points in the fine mesh (in spite of the fact that the PCs are getting faster and faster), plus avoids the use of built-in accuracy checks. Next frequent error is incorrect specification of material properties, namely magnetization curves. With all that obtaining wrong results is not difficult. A simple procedure to avoid them is to read the manuals and check the test examples provided with the software.

EOD program can be very accurate. In ray tracing the critical parameter is the use of dense meshes. For the best results the most suitable meshes are rectangular in the region where the particles move, and adequate interpolation method suitable for a given task should be selected. For example, the non-physical behavior of the slice method implemented formerly in the TRC program, where the expansion of potential was used only up to the third term in radial expansion in r^2, was found insufficient for getting 5th order aberrations in electrostatic lenses such as mirror [2], with "horrific" disagreement of 7% in Cs5. This problem was removed simply by not implementing this method in EOD. The "universal" ZRP interpolation method fits potential so that neither the potential nor the fields are continuous; thus it tends to introduce random errors that can be avoided by statistical processing of the results and using sufficiently large distance of particles from the axis [3]. Such a character of computation error is best visualized by plotting e.g. Cs effect for axial points as $\Delta r/\alpha$ on α^2. In practice bi-cubic and bi-quintic 2D interpolation is our recommendation for computations accurate enough to get easily aberrations and aberration figures; this naturally requires rectangular mesh around the axis. The source of problems can be, of course, the low quality of the field if not the data error, but this is again easy to identify by plotting the potentials and fields along selected lines and checking the relevant graphical outputs available.

Electrodes of electrostatic lenses naturally cannot have sharp corners, although the rounding of the electrodes is not difficult, and there are insulators further away from the axis; all that naturally changes the field distribution. The question is how much they change the optical properties when we neglect the rounding, and if this change is worth noticing in the values of the optical properties. The errors introduced by using inclined mesh lines in the coarse mesh

to input the unnecessary geometrical detailed features of the lens often introduce much larger error than more simple coarse mesh [4]. Of course, the field can be influenced by the boundary position and boundary condition. Often there is no analysis is given about the influence of the boundary conditions!

In recent literature papers appear on "electron optics" based on 2D SIMION [5, 6]. If we neglect the lack of information on basic physical problem of what boundary conditions and mesh size are used, one can often ask what accuracy has the result and if they mention it, how do they understand the parameter? Why aberrations are still extracted from ray traces and not computed from aberration integrals as electron optics does by using the extracted axial potential.

The discussion of meshes and material problems in magnetic lenses and in calculation of multipole field components is sufficiently discussed at CPO-6to CPO-8 papers [1, 7, 8] and at previous meetings of this series. We have also added the computations of the permanent magnet lenses in EOD [9].

The tolerancing analysis does not need the full 3D field [1]. We also do not need the 3D to calculate the aberration corrector. On the other hand, the developments in 3D computations have become a reality with faster computers and workstations. These programs do not often provide the accuracy high enough and they do not allow ray tracing with sufficient accuracy. In EOD we have intensively tested a plugin to import 3D data from a range of 3D programs available (e.g. COMSOL, Field Precision, SIMION 3D). The problem is then to find a suitable interpolation method, and as before to check the field quality by computing (and plotting) the fields (not published).

References:
[1] Zlámal J. and Lencová B., Nucl. Instr. Meth. in Phys. Res. A 645 (2011) p. 278–282.
[2] Lencová B., *Recent Trends in Charged Particle Optics and Surface Physics Instrumentation - 6th Seminar* 1998, p. 40-43.
[3] Oral M. and Lencová B., *Ultramicroscopy* **109** (2009) p. 1365-1373.
[4] Lencová B., Nucl. Instr. Meth. in Phys. Res. **A 519** (2004) p. 141–148.
[5] Sise O., Ulu M. and Dogan M., Nucl. Instr. Meth. in Phys. Res. **A 554** (2005) p. 114–131.
[6] Fitzgerald J.P.S., Word R.C., and Könenkamp R., Ultramicroscopy **115** (2012) p. 35-40.
[7] Lencová B., Nucl. Instr. Meth. in Phys. Res. **A 519** (2004) p. 149–153.
[8] Lencová B. and Zlámal J., *Phys. Procedia* **1** (2008) p. 315-324.
[9] Adamec P., Delong A., and Lencová B., J. Microscopy **179** (1995) p. 129-132.

LYRA 3 GM – A VERSATILE MULTIFUNCTIONAL TOOL

B. Lencová*, J. Jiruše, F. Lopour, M. Zadražil, M. Rudolf, T. Šamořil, J. Dluhoš

TESCAN a.s., Libušina třída 21, 623 00 Brno, Czech Republic
*e-mail bohumila.lencova@tescan.cz

LYRA3 GM is a powerful tool for nanotechnology capable of observation, measurement, analysis, manipulation, and manufacturing on the nanoscale with a unique analytical system. The combination of a number of observation and analytical methods in a single instrument avoids moving the studied sample among several devices for different applications and the time consumed for the necessary localization of the nano-sized object. The core of the system is a high resolution SEM with resolution 1 nm combined with a Ga FIB having a 2.5 nm resolution [1], both at 30 kV. In-situ scanning probe microscopy (SPM, e.g. [2]) complements the imaging possibilities; tunneling, atomic and magnetic force microscopy (STM/AFM/MFM) modes are possible in the high vacuum environment of the SEM. The SEM is used for finding the regions worth studying with SPM, navigating the tip to the sample surface, simultaneous observation of tip movement and checking the tip quality. The SEM is also used simultaneously for the observation of FIB modifications of the sample.

A whole range of detectors for secondary electrons (SE), back-scattered electrons (BSE), electron-beam induced current (EBIC), cathodoluminescence (CL) and TESCAN detector of secondary ions (SITD) have been combined with analytical methods of energy or wavelength dispersive X-ray spectroscopy (EDX, WDX), electron back-scatter diffraction (EBSD) and time-of-flight secondary ion mass spectrometer (TOF-SIMS) in such a way that imaging and analysis is possible at the same working distance of 9 mm of SEM, for which also the gas injection system (GIS) is accessible. Optionally nanomanipulators and nanoindentor are available. Most detectors can be applied simultaneously for imaging but also for 3D tomography. Unique results were reported with orthogonal TOF-SIMS [3].

LYRA3, similar to all TESCAN microscopes, works with an extremely large range of field of view due to patented WideField optics™. Typical applications of SEM/FIB for electron and ion lithography and gas-assisted electron and ion beam induced deposition can be performed under computer control using the DrawBeam™ software. The SPM technique (a comparison of SE and AFM image is shown in Figure 1) opens a completely new range of applications, such as determination of depth of sputtered areas and calibration of sputtering rate of FIB etching, determination of the height of the deposits with electron and ion beam assisted deposition from GIS, etc. To get high quality SPM images, it is necessary to avoid that the tip gets blunt, dirt particles or parts of the sample attach during the observation after some time of operation, or broken tips are used; all this can be checked in SEM image. Moreover, the FIB can be used for repair or re-sharpening of the most frequently used Si AFM tips. The modification of the tip shape is possible with the DrawBeam™ software used to remove selectively the tip material and create tip shape suitable for high resolution scanning or imaging deeper structures. Such a repair can be repeated several times (sees Figure 2).

The large range of imaging and analytical techniques as well as the availability of lithography, sample modification and manufacturing, makes LYRA3 GM a versatile multifunctional tool for microscopy and nanotechnology.

References:
[1] Delobbe A., Salord O. and Sudraud P., The ECR-FIB. The EFUG2011 meeting, available at http://www.imec.be/efug/EFUG20o.html.
[2] Curlew™SPM, brochure from 31-1-2012, available at www.specs.com.
[3] Whitby J. A. et al., Adv. Mater. Sci. Eng., Volume 2012, Article ID 180437, 13 pages.
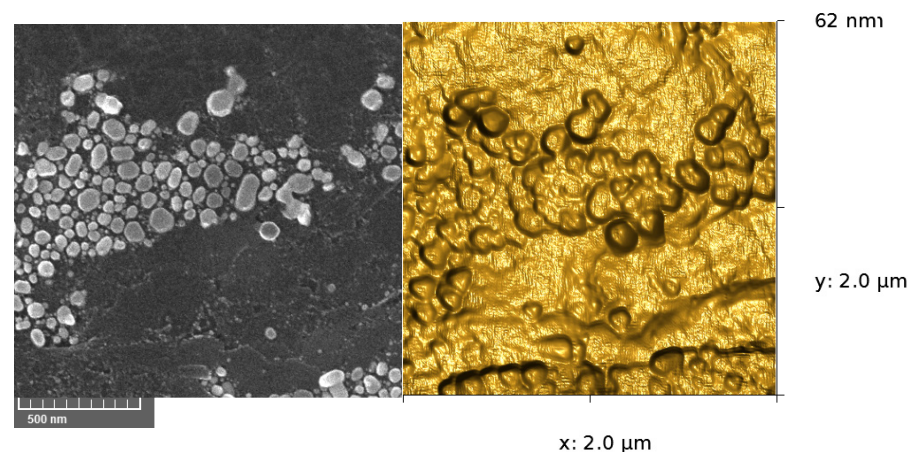
Figure 1 Gold on carbon specimen imaged with SEM and AFM from the same region. Vertical range of AFM image is 62 nm.
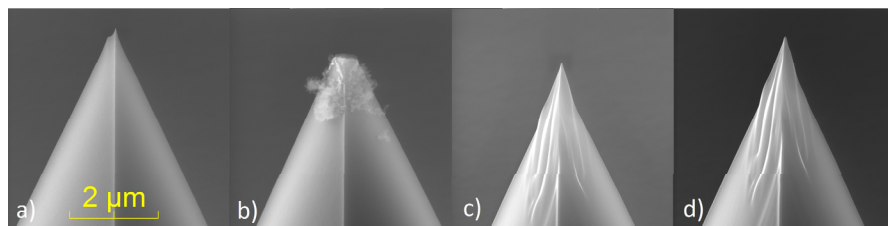
Figure 2 Repair of silicon AFM tips: a) the new tip b) tip after more than 13 hours operation on calibration grating SiO_2/Si in contact mode, c), the same tip after repair by FIB (30 keV; dose $8.3*10^{17}$ Ga ions/cm^2) and d) after the same 13 hours of AFM measurement.

OBSERVATION OF HIGH STRESSED HYDROGENATED CARBON NITRIDE FILMS BY SLEEM

E. Mikmeková[1*], I. Müllerová[1] and J. Sobota[1]

[1]Institute of Scientific Instruments of the ASCR, v.v.i., Královopolská 147, Brno 612 64, CZ
*e-mail: eliska@isibrno.cz

Two main factors can lead to losing adhesion in thin sputtered carbon nitride films: high residual stress and absorption of humidity.

Basically, two different types of stress can be identified in thin films: compressive stress and tensile stress. Compressive stress can lead to wrinkling and film delamination, and tensile stress can cause the fracturing of thin films [1]. For reactive sputtering of hydrogenated carbon nitride films, the compressive stress is typical. The films were prepared from graphite target (high purity, 99.9999 %) in mixture of nitrogen and hydrogen discharge.

During the WCA (water contact angle) experiments we discovered the destruction of CN_x:H film (delamination blisters on all sample surfaces) per second. This effect is caused by absorption of moisture, their diffusion into the bulk, and then to the interface. The post-deposition annealing in vacuum can be a way to improve adhesion between interfaces and to eliminate the open character of the films.

In order to determine stress in thin films we used a home assembled high-resolution X-ray diffractometer. The stress is calculated by Stoney´s equation:

$$\sigma = \frac{E_s}{1-v_s} \cdot \frac{d_s^2}{6d_f R}$$

where the E_s is elastic modulus, v_s is Poisson's ratio, d thickness (s: substrate, f: film), and R is radius of curvature. The films start to loss adhesion when the films residual stress is higher than so called critical value of stress. In the case of our films, this value can be calculated from the size of delamination (telephone cords) [2]:

$$\sigma_c = \frac{\pi^2 E_f}{12(1-v_f^2)} \cdot \frac{h^2}{b^2}$$

This critical value is connected to the film thickness h, the half-buckle width b, the material properties of elastic modulus E, and the Poisson's ratio v.

For observation of the consequences of residual stress and absorption of moisture to interface, we used Scanning Low Energy Electron Microscopy (SLEEM). SLEEM is increasingly becoming recognized as a valuable analytical tool in the field of materials science. Experiments were made in the Tescan TS 5130 MM equipped with the Cathode Lens system (CL), which enables us to observe samples at arbitrary landing energies of the illuminating electrons. Operation of a SEM at low energies offers several advantages: an increase of signal given by SE and therefore high signal to noise ratio of the final image, smaller interaction volume and elimination of charging effects [3].
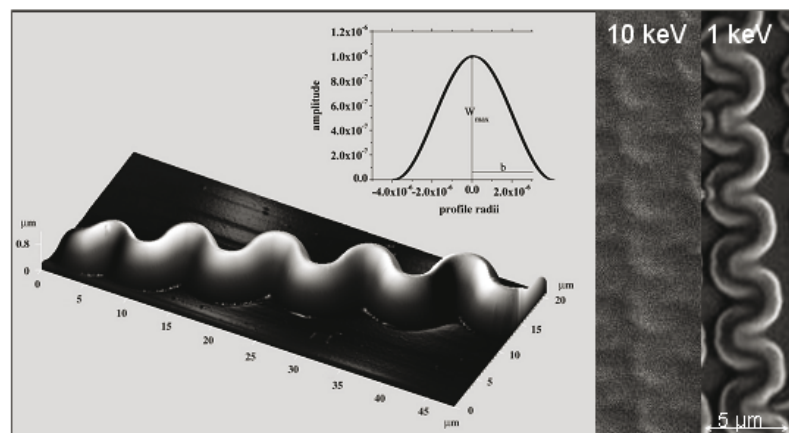
Figure 1 Telephone cords observed by AFM [2] and SLEEM by 10 keV and 1 keV. The critical value for CN_x:H is 1.10 GPa.
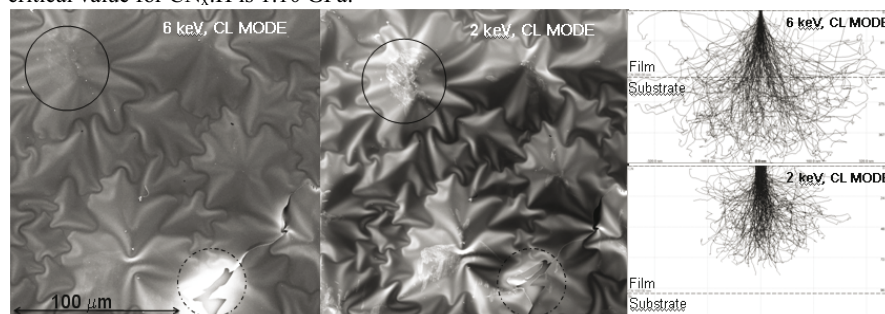
Figure 2 Delamination blisters of CN_x:H observed by SLEEM and penetration depths are calculated by software Casino [4].

Figure 3 Annealed CN_x:H after contact with water (from 600 °C the films are stable).

References:
[1] M. Ohring, Materials Science of Thin Films, Academic Press, San Diego (1992).
[2] S. Peponas, M. Guedda, M. Benlahsen, Solid State Communications 146 (2008) 78–82.
[3] I. Mullerova. L. Frank, Adv. Imag. Electron Physics 128 (2003) 309-443.
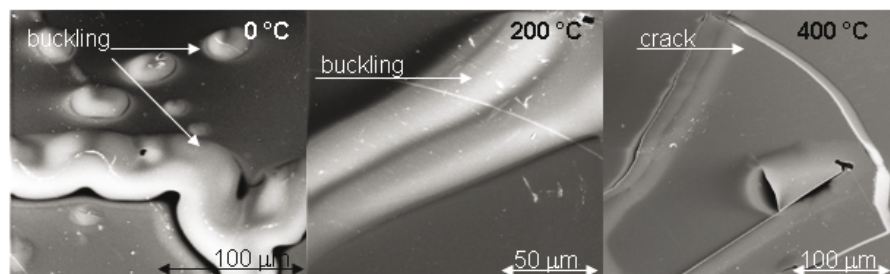[4] www.gel.usherbrooke.ca/casino/What.html

CHARACTERIZATION OF INDUSTRIAL MATERIALS BY SLOW AND VERY SLOW ELECTRONS

Š. Mikmeková[1*], I. Müllerová[1] and L. Frank[1]

[1]Institute of Scientific Instruments ASCR, v.v.i., Královopolská 147, 612 64 Brno, Czech Republic
*e-mail: sarka@isibrno.cz

Progress in materials science and engineering is inseparably connected with excellent knowledge of the correlation between materials properties and their microstructure. In our experiment an ultra-high vacuum scanning low energy electron microscope (UHV SLEEM) of an in-house design was used to observe microstructure of specimens. The UHV SLEEM is equipped with the cathode lens (CL) assembly, which enables us to observe samples at arbitrary landing energies of primary electrons. The device provides argon ion beam for in-situ cleaning of the specimen surface [1].

By means of slow and very slow electrons reflected from the sample surface and effectively detected in their full angular and energy distribution the crystalline structure is imaged at high spatial resolution, and high contrast is obtained between differently oriented grains in polycrystals and between areas with different chemical composition in multi-component materials [2 to 4].

We have applied the UHV SLEEM for characterization of common industrial materials such as a duplex (ferritic – austenitic) steel (Fig. 1), ledeburic tool steel, cast CB2 steel (Fig. 2) and non-ferrous alloys. In all cases the SLEEM method provides a tool capable of examining the structures with extremely high sensitivity and spatial resolution [5].

The SLEEM has proven itself very effective for studying a wide range of materials and is very useful not only in fundamental research but also for practical diagnostics of materials.

References:
[1] I. Müllerová and L. Frank: Adv. Imag. Electron Phys. 128 (2003), 309-443
[2] Š. Mikmeková et al.: Mater. Trans. 52 (2011), 292-296
[3] Š. Mikmeková et al.: Key Eng. Mater.465 (2011), 338-341
[4] Š. Mikmeková et al.: Mater. Trans. 51 (2010), 292-296
[5] Š. Mikmeková et al.: Acta Metalurgica Slov. (2012), in press
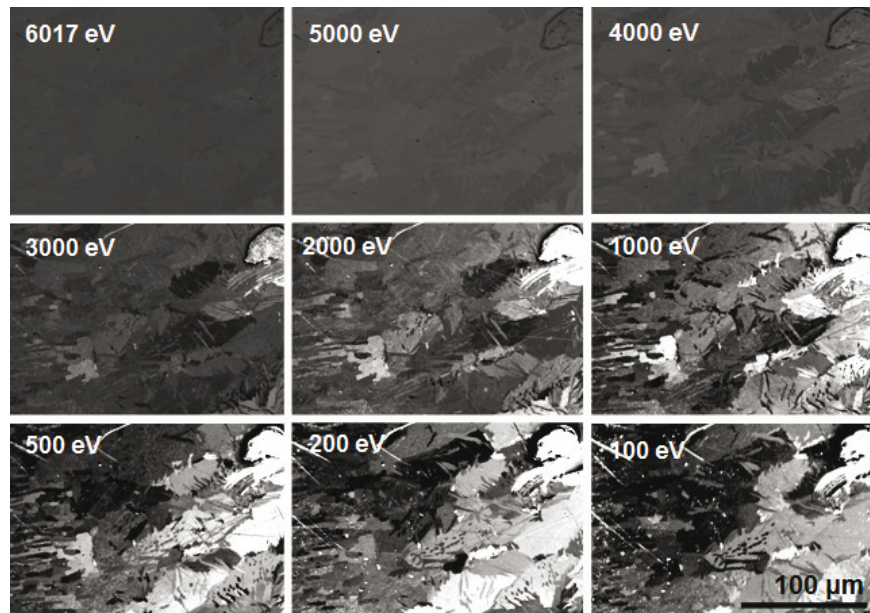
Figure 1 The heat affected zone on the duplex (ferritic – austenitic) steel surface, in-situ cleaned by the Ar+ ions and imaged in the UHV SLEEM microscope. Electron impact energies are labelled.
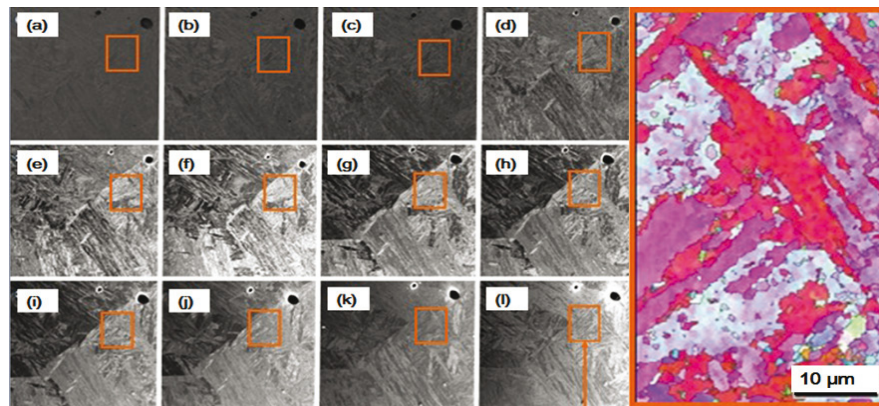
Figure 2 UHV SLEEM images of the CB2 steel. The incident electron energies were 6012 eV (a), 5000 eV (b), 4000 eV (c), 3000 eV (d), 2000 eV (e), 1000 eV (f), 500 eV (g), 400 eV (h), 300 eV (i), 200 eV (j), 100 eV (k) and 50 eV (l); the EBSD map of the same area (on the right).

PRACTICAL ASPECTS OF AN APLANATIC TRANSMISSION ELECTRON MICROSCOPE

H. Müller, I. Maßmann, S. Uhlemann, P. Hartel, J. Zach and M. Haider.

Corrected Electron Optical Systems GmbH, Englerstr. 28, D-69126 Heidelberg, Germany.
e-mail: mueller@ceos-gmbh.de

During the last decade aberration correctors have become well-accepted tools in high-resolution transmission electron microscopy. These correctors compensate for the spherical aberration C_s of the imaging system. Also the simultaneous correction of the chromatic aberration C_c has been demonstrated successfully at an energy range from 80 kV to 300 kV [1]. For instruments with considerably improved information limit recently the off-axial aberrations have attracted more attention since these aberrations can limit the high-resolution field of view. Parasitic second-order off-axial astigmatism and third-order azimuthal off-axial coma are most critical among these generalized coma aberrations [2].

Recently, we have introduced the next-generation aplanatic C_s/B_3-corrector CEOS B-COR for the conventional TEM. This three-stage hexapole corrector has been integrated with the new Hitachi HF3300V TEM equipped with a cold field emission gun [3]. Due to its small intrinsic energy width and the good stability this aberration-corrected instrument provides an information limit of better than 70 pm at 300 kV [4]. This has been verified with the Young's fringes method at a thin tungsten specimen (Fig. 1). The residual aberrations of the system at 300 kV have been characterized with the diffractogram tableau method. The axial aberrations up to fifth order have been calculated from the induced C1 and A1 values for a tilt set with an outer tilt angle of 40 mrad by least squares fitting. To determine the coefficients of the generalized coma up to third order we recorded a tilt set with an outer tilt angle of 24 mrad. For each tilt position C1 and A1 have been evaluated at four off-axial 512 x 512 sub-regions of the 2k x 2k image (see Fig. 2). Both measurements were recorded with the same Nyquist frequency of $f_{Ny} = 6.68$ nm^{-1}. From this data the linear variation of the lower-order axial aberrations over the field of view can be calculated with good precision. For each axial aberration coefficient K of first and second Seidel-order two off-axial components must be determined [5]:

$$K_\gamma = \frac{1}{4\sqrt{2}|\gamma_0|}\left[\left(K_{13}-K_{24}\right)-i\left(K_{13}+K_{24}\right)\right]$$

$$K_{-\gamma} = \frac{1}{4\sqrt{2}|\gamma_0|}\left[\left(K_{13}-K_{24}\right)+i\left(K_{13}+K_{24}\right)\right]$$

The results in Tab. 1 show that the azimuthal off-axial coma has been reduced from 0.7 to less than 0.1 while the parasitic off-axial two-fold astigmatism is below 0.01. All axial coefficients including the fourth order are corrected and the residual six-fold astigmatism is below 100 µm.

In our contribution we will discuss different mechanisms how off-axial aberrations occur in an uncorrected TEM and describe methods how they can be measured quantitatively. Finally, we will show how these aberrations can be compensated and why a careful discrimination between off-axial and higher-order axial aberrations during alignment with convergent or divergent illumination is mandatory.

[1] M. Haider, et al. Advances in Imaging and Electron Physics 153, 43-119, 2008.
[2] M. Haider, et al. Microsc. Microanal. 16, 393-408, 2010.
[3] T. Sato, et al. Hitachi Rev. 57(3), 132-135, 2008.
[4] H. Müller, et al. Proceedings of MC 2011 Kiel (Germany), 2011.
[5] H. Müller, et al., Nucl. Instr. and Meth. A 645(1), 20-27, 2011.
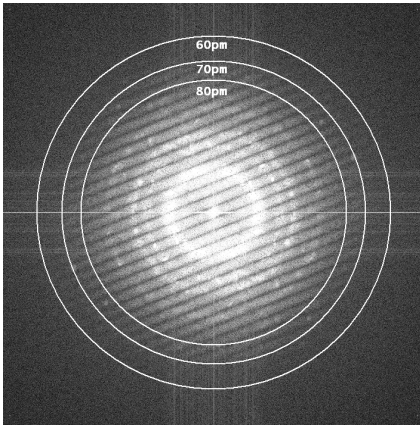
Figure 1. Central region of a Young's fringe pattern from a thin tungsten specimen recorded at 300 kV with 4 s illumination time. The Nyquist frequency in the original image is 38.3 nm^{-1}.

Figure 2. Definition of sub-regions used for the analysis of off-axial aberration across the field of view for each individual image in the tableau. Only differences of diagonally opposite regions are evaluated.

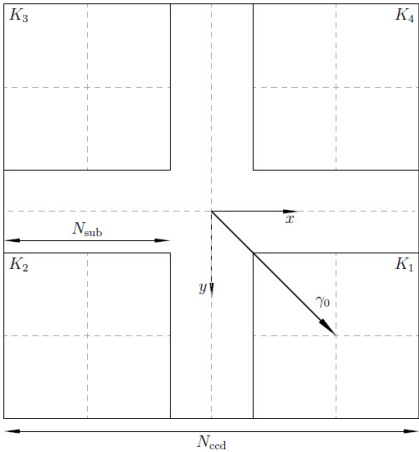| coeff.	value	abs. err.	coeff.	value	abs. err.	coeff.	value	abs. err.
C_1	-204 nm	0.7 nm	$C_{1\gamma}$	0.077 / -163°	0.002			
A_1	0.5 nm / -79°	0.5 nm	$A_{1\gamma}$	0.005 / 113°	0.004	$A_{1\overline{\gamma}}$	0.006 / -108°	0.004
B_2	12 nm / 52°	11 nm	$B_{2\gamma}$	0.03 / -130°	0.04	$B_{2\overline{\gamma}}$	0.07 / -51°	0.04
A_2	14 nm / 128°	12 nm	$A_{2\gamma}$	0.40 / 25°	0.07	$A_{2\overline{\gamma}}$	0.14 / -70°	0.01
C_3	4.1 µm	0.8 µm	S_3	49 nm / 55°	65 nm	A_3	100 nm / -99°	111 nm
B_4	9.3 µm / 170°	2.6 µm	D_4	5.0 µm / 20°	1.0 µm	A_4	5.3 µm / -78°	2.2 µm
C_5	-3.2 mm	0.3 mm	A_5	49 µm / 30°	46 µm			

Table 1. Residual axial and off-axial aberration coefficients measured at 300 kV from a tilt tableau with 40 mrad (axial) and 24 mrad (off-axial) aberrations. The absolute error is the radius of the 95% quantile estimated from the residuals of the least squares fit.

COLLECTION CONTRAST IN THE IMMERSION OBJECTIVE LENS OF THE SCANNING ELECTRON MICROSCOPE

I. Müllerová*, I. Konvalina and F. Mika

Institute of Scientific Instruments of the ASCR, v. v. i., Královopolská 147, 612 64 Brno, Czech Republic
*e-mail: ilona@isibrno.cz

Signal trajectories of secondary (SE) and backscattered electrons (BSE) were simulated for two cases: an immersion magnetic objective lens (OL) alone and for the case when an electrostatic immersion objective lens is added. Micrographs of a semiconductor structure are presented for these two set-ups.

Collection efficiency of the detectors is one of the most important parameters of a scanning electron microscope (SEM). It describes how many electrons are collected out of all the electrons emitted from the specimen. Considering the contrast formation of the final specimen image, it is very important not only to know the number of collected electrons but especially, what part of the energy and angular distribution of the emitted electrons is collected. We can speak about the collection contrast. Spatial immersion objective lenses using strong magnetic and/or electrostatic fields were designed to obtain sub-nm spot size of the primary beam down to low energies, but their fields influence the signal trajectories. Therefore, the same specimen can exhibit a different contrast in different SEMs depending on operation conditions such as the working distance, specimen holder size etc. Several authors have been engaged in this topic; see e.g. [1-4]. We present the changes in contrast formation for a case when a strong electrostatic field of the cathode lens (CL) [5] is added to the magnetic field of the immersion objective lens.

Fig. 1a shows the simulations of the BSE and SE trajectories when these are influenced by the magnetic field. The magnetic field reaches a maximum of 261 G on the axis and 237.7 G in the specimen plane. It looks as if all SE could be collected by the upper detector located above the objective lens, but the magnified detail in Fig. 1b shows that SE emitted under large angle will be turned back to the specimen (so called "bottle" effect). It is impossible to distinguish initial polar angles of the BSE and SE trajectories in the final image as they are strongly mixed. Smooth trajectories can be obtained and all SE can be collected when a strong electrostatic field is added to the specimen region, see Fig. 1c and 1d. Electrostatic field of the CL is formed by the negative potential on the specimen (cathode) and by the ground potential of the anode (YAG detector with the inner opening of 0.3 and 1.7 mm). The micrographs of the semiconductor structure for all simulated conditions are shown in Fig. 2.

References:
[1] Griffin B. J., Scanning **33** (2011**)**, p. 162-173.
[2] Cazaux J., Journal of Microscopy **217** (2004), p. 16-35.
[3] Konvalina I. and Müllerová I., Scanning **28** (2006), p. 245-256.
[4] Konvalina I. and Müllerová I., Journal of Microscopy **236** (2009), p. 203-210.
[5] Müllerová I. and Frank L, in: Adv. in imag. and electron physics **128** (2003), p. 309-443.
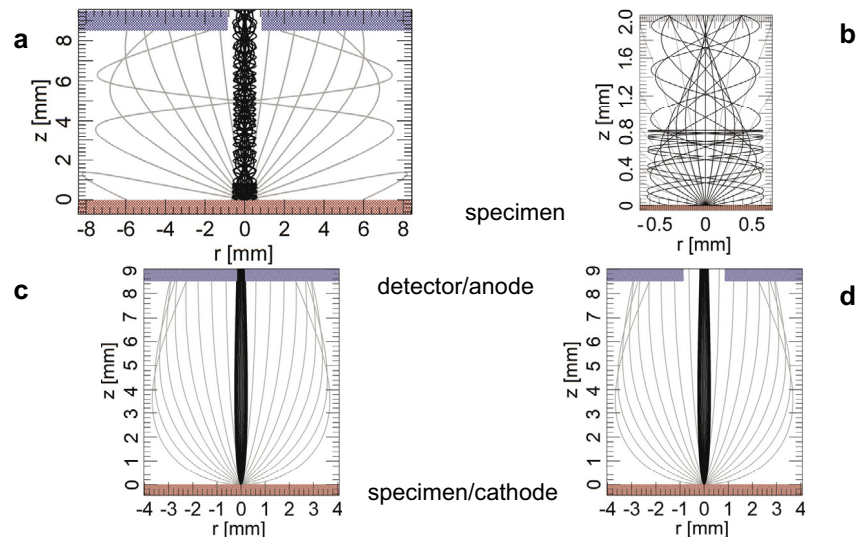
Figure 1 (a) Simulated trajectories of BSE (1keV-gray lines) and SE (5 eV-black lines) for polar angles ± 90° with a step of 10° in a strong mag. field. (b) Magnified detail of the specimen region in Fig.1a. (c, d) Electrostatic field of the CL (4kV/8.5 mm) is added to the specimen region between the specimen and detector.
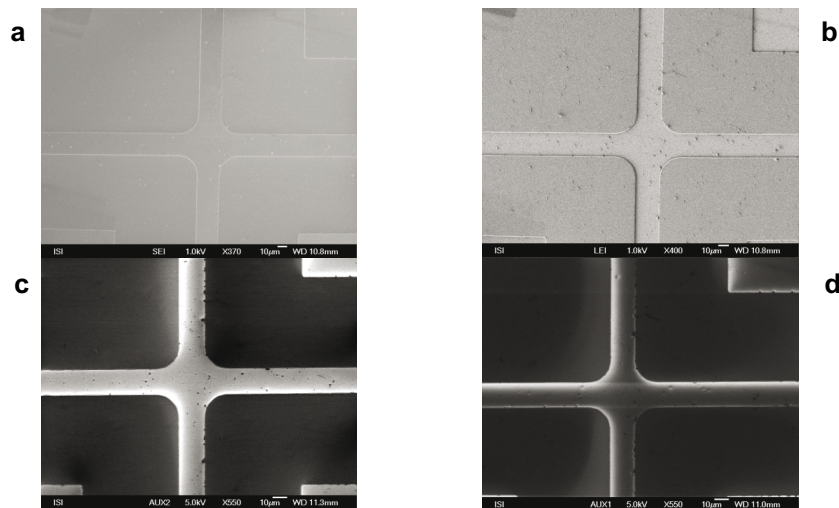
Figure 2 Micrographs of P-type areas (boron of the surface concentration $1\times10^{19}/cm^2$) on an N-type substrate Si <111> covered by oxide, imaged in JEOL JSM 6700F, where the mag. field is present in the specimen region. (a): image obtained by the SE detector above the OL, (b): image taken by a lateral SE detector positioned between the specimen and the OL, (c, d): the elstat. field of the CL is added and the micrographs corresponds to the set-up of Fig. 1c, d. In figure 2a, 2b, the primary beam energy is 1 keV. In figure 2c and 2d, electrons of the energy 5 keV are decelerated by the specimen potential of - 4 kV to a final energy of 1 keV.

FAST SIMULATION OF ToF SPECTROMETERS

M. Oral[1]

[1]Institute of Scientific Instruments of the ASCR, v.v.i., Královopolská 147, 612 64 Brno, Czech Republic
*e-mail: oral@isibrno.cz

A fast simulation method was developed for analysis of time-of–flight spectrometers and it has been successfully used to optimize parameters of a real instrument. In the general case, the function of a time-of-flight spectrometer is best modeled using the Monte Carlo method [1]. That involves calculation of a high number of ion trajectories, which is time consuming. We have found a way to reduce the calculation time greatly by introducing a simplification and using pre-computed data independent on the ion mass and charge. The procedure makes it computationally feasible to run iterative optimizations. By comparing the results with those of a realistic simulation on a selected case, we have verified that there is no noticeable influence on the results.

In the time-of-flight secondary ion mass spectrometry (ToF SIMS), the sample is probed with a pulsed, focused ion or laser beam. Secondary ions are collected with an extracting electrostatic field which accelerates them into the time-of-flight analyzer. The secondary ions are emitted from the sample at different times during the primary beam pulse, and they have energy and angular distributions. The spread in the initial energy and the differences in emission times are the two main properties that limit the mass resolution of the instrument. Namely, shorter primary pulses provide a better mass resolution, as the bunches of ions with equal mass to charge ratio are better synchronized, and narrower energy distributions lead to smaller differences in times of flight at the detector. The influence of the energy distribution can be reduced, but not completely removed, using an electrostatic mirror (reflectron). On the other hand the pulses can only be made short at the expense of the signal strength (and signal-to-noise ratio) or the spatial resolution, if the burst alignment mode [2] is used.

For several decades, a method known as *delayed extraction* or *time-lag focusing* has been used to partially compensate for those two resolution-limiting influences [3]. During the primary pulse, the extracting field if switched off. Secondary ions then drift in a field free space (Coulomb interactions are neglected), maintaining their initial velocity and direction. However, basic theory on the delayed extraction [3,4] shows that one cannot compensate for both different initial energies and different emission times simultaneously, there is a trade-off between the two types of time focusing.

We have developed a greatly accelerated simulation of the ToF spectrometer, which enables efficient search for the optimal parameters that provide the best mass resolution at given circumstances. As a testing configuration the system in Fig. 1 was used. The extraction lens collects and accelerates secondary ions and focuses them further into the system in a way that the loss of the ions in the instrument is minimized. After drifting in a field-free space, the ions enter a reflectron (an electrostatic mirror), which emulates about 250 mm long homogeneous field using a system of rings. The mirror is tilted under the angle of 2°. The ions decelerate in the mirror to an almost complete standstill (depending on their angle of attack) and are accelerated back. The tilt and the position of the mirror causes that the exiting beam is tilted under 4° relative to the entering one. The ions then impact on a detector. The electrostatic fields and ion trajectories were computed in EOD [5]. Later trajectories were computed using

Trasys (a ray-tracing predecessor to EOD), as it enables a better automated processing and easier parallelisation. With Trasys, an interpolation using electrostatic field series expansion about the optical axis was used, the necessary axial potential derivatives were obtained using a method based on Green's theorem [6]. The agreement between the trajectories computed in EOD and in Trasys was verified on selected examples and it was found to be very good.

In the simulation it is assumed that the secondary ions are emitted from the axial point on the sample. Each ion is assigned initial azimuth and elevation angles (cosine distribution in the solid angle) and an emission time (uniform distribution) during the primary pulse and the initial kinetic energy (Thomson's distribution, binding energy of 5 eV). An ion then follows a uniform linear motion until the extracting field is switched on. The Coulomb interaction between ions is neglected, but it could be modeled using an algorithm described in [7]. After the extraction is activated, the ions are accelerated into the lens and the fly through the system. Many of them hit a barrier before reaching the detector. The trajectories in the electric fields of the system are computed with ray tracing and the times of flight are recorded. The simulated spectrum is obtained as a histogram. The properties of a ToF mass spectrometer are usually studied for a few ion masses and charges, significant in typical usage of the instrument.

The trajectory calculation can be easily parallelised, taking advantage of today's multi core computers and clusters. However, a typical calculation involves, according to our experience, several million of ions, which still makes repeated simulations prohibitive. Several simplifications were introduced without a noticeable influence on the results. Due to the limited admittance of the system (Fig. 2), the particles eventually transmitted onto the detectors occur in a narrow region around the optical axis when the extracting field is switched on. The 3D position then can be reduced by considering just its projection onto the z-axis. The difference in times of flight is negligible. The ToF function then can be reasonably represented by an interpolation of the time of flight on a grid of z and energy values. The interpolation table is computed for a reference mass and charge; the interpolated values of time of flight are scaled with the appropriate factor for the required mass and charge. The decision whether an ion will reach the detector or hit an obstacle is provided by pre-computed admittance data (Fig. 2) which is also independent on mass and charge and the timing of the time-lag focusing. The calculation of time of flight is then several thousand times faster.

As an example we present an optimization of the time-lag after the primary pulse, t_d, for the primary beam pulse duration of 50 ns (Fig. 3) and the ion mass of 50 amu. The mass resolution is calculated as $t/(2\Delta t)$, where t is the mean time of flight and Δt is a characteristic width of the intensity distribution for which we use several criteria. Here we present results of the usual full width at half-maximum (FWHM) and the distance between equal levels around the maximum containing 50 % of the integral. 10^7 particles were used in the calculation. The dependencies in Fig. 3, calculated for 201 values of t_d, took about 10 minutes to calculate. The same calculation using the full 3D initial positions without the interpolation would take more than 100 days to complete. The simulation shows that each criterion provides different optimum with different intensity distribution shapes (the FWHM tends to ignore long tails of a curve). It is also clear that a longer t_d decreases the collection efficiency, which is caused mainly by the energy-filtering effect of the reflectron. One then has to select a balance between the measurement speed and the shape of the spectral lines which, in fact, determines the mass resolution.
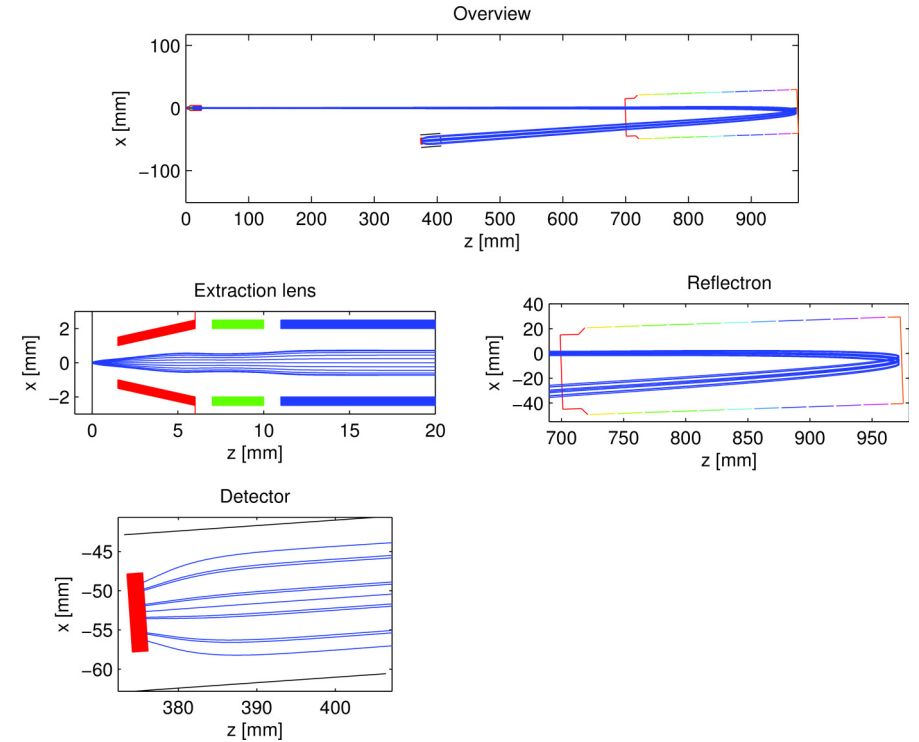
Figure 1: ToF analyzer. The sample (z = 0) is grounded. The electrode facing the sample is at a pulsed extraction voltage of 500 V. The central focusing electrode is at 3640 V and the exit electrode is at 2000 V. The ring electrodes of the reflecron are at equidistantly distributed potentials from 2000 V to -20 V; there is some energy filtering, as too energetic ions are not reflected back. The detector is a micro-channel plate at 10 kV, surrounded by a shielding tube at 2 kV.
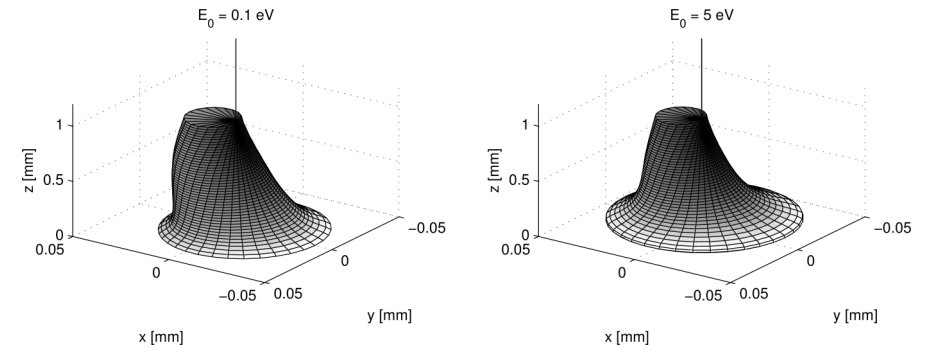
Figure 2: Admittance bodies at two values of the initial energy. The ions that are inside the region at the start of the extraction are transmitted by the optics of the analyzer onto the etector.
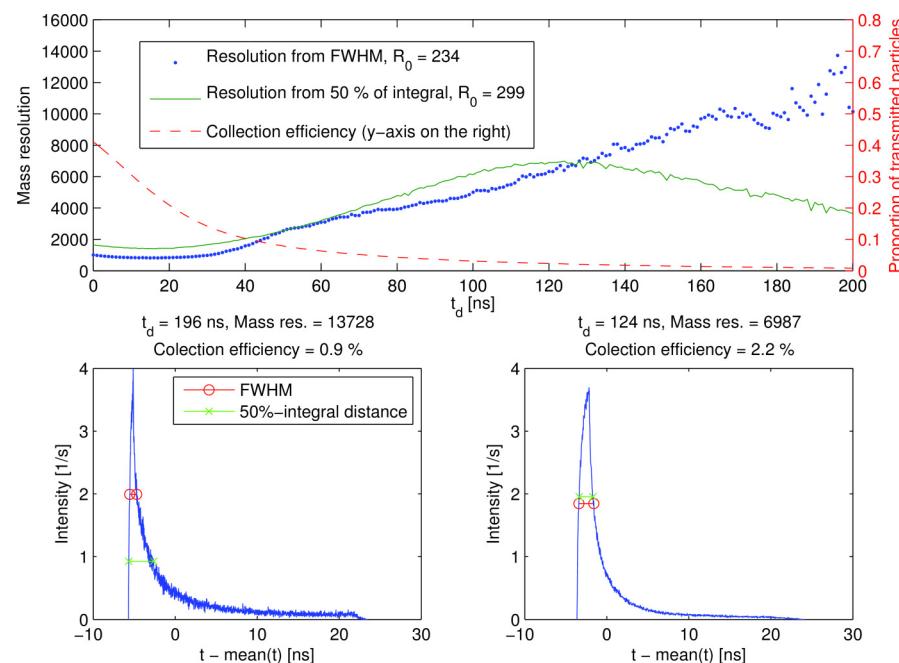
Figure 3: Dependency of mass resolution for 50 amu on the extraction delay, t_d, of the primary pulse, obtained using two criteria for the width of the intensity distribution curve. The duration of the primary pulse is 50 ns. R_0 (in the legend) is the value of the resolution without the time-lag focusing.

References:
[1] Weisstein E. W., http://mathworld.wolfram.com/MonteCarloIntegration.html
[2] Sodhi R. N., Analyst **129** (2004): p. 483–487.
[3] Wiley W. C. and McLaren I. H., Rev. Sci. Instrum. **26** (1955), p. 1150—1157.
[4] Colby M., Reilly J. P., Anal. Chem. **68** (1996), p. 1419—1428.
[5] Zlámal J., Lencová B., Nucl. Instr. Meth. A **645** (2011), p. 278—282.
[6] Radlička T., Lencová B., Ultramicroscopy **110** (2010), p. 1198—1204.
[7] Radlička T., Ultramicroscopy **108** (2008), p. 445—454.

DEVELOPMENT OF A THIN-FILM SPINFILTER OPTICS FOR PEEM

D. Panzer[*], J. Kuttig and G. Schönhense

Institut für Physik, Johannes Gutenberg-Universität, 55128 Mainz, Germany
[*] e-mail: panzerd@uni-mainz.de

Analysis of spin polarized electrons is a vital aspect of experiments in nuclear, molecular, surface and solid-state physics and of fundamental importance for investigations of ferromagnetic materials. Spin dependent transmission and spin rotation of electrons passing ferromagnetic thin films has been studied by Weber and coworkers [1,2]. Uniform magnetization of such a film allows it to act as a spinfilter for an electronic image.

In the present work we use an imaging system that projects an electron optical image onto such an ultrathin ferromagnetic film and then watch the transmitted electrons using a standard Photo Emission Electron Microscope (PEEM) column (see Fig. 1).
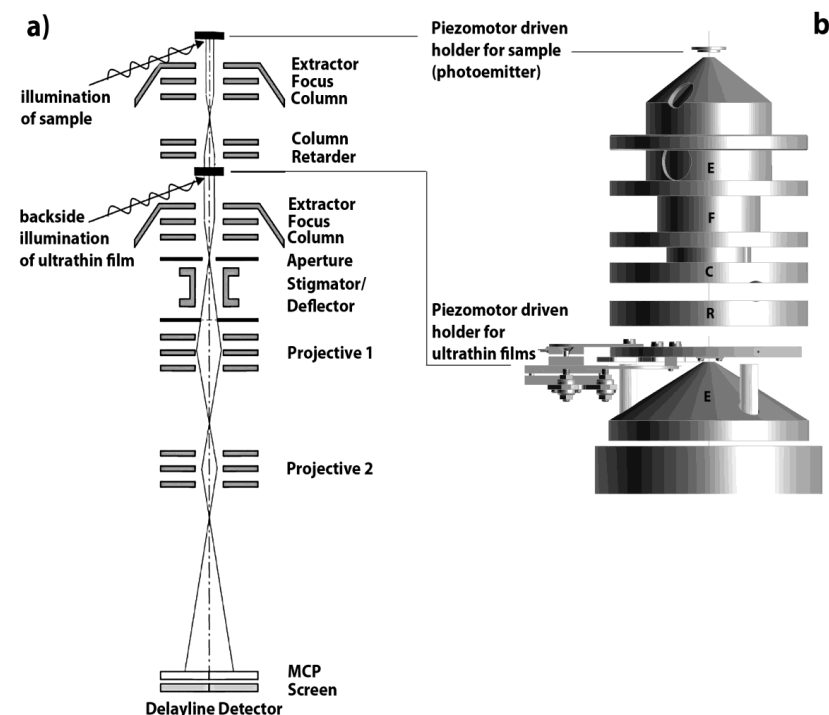
Figure 1 Electron optical layout (a) and view of the setup for spin dependent transmission (b). Add-on with thin-film filter and tandem optics mounted at the front of the PEEM.

Photoelectrons are emitted by a Hg lamp (hν = 4.9eV) and the slightly magnified electron optical image of the photoemission pattern is focused onto the surface of the film. The electrons transmitted to the other side are "viewed" by a cathode lens microscope similar to a PEEM and are detected by an MCP/screen/CCD camera combination or a delay line detector.

The inelastic mean free path λ_{IMFP} of electrons in matter is strongly energy dependent, i.e. it increases steeply at low energies < 20eV [3]. For transition metals it was predicted [4] and confirmed [5,6] that λ_{IMFP} is inversely proportional to the number of *d* holes.

In order to test the projection and imaging system we initially used the transmission through a TEM grid instead of a thin film, the results of which can be seen in Fig. 2.
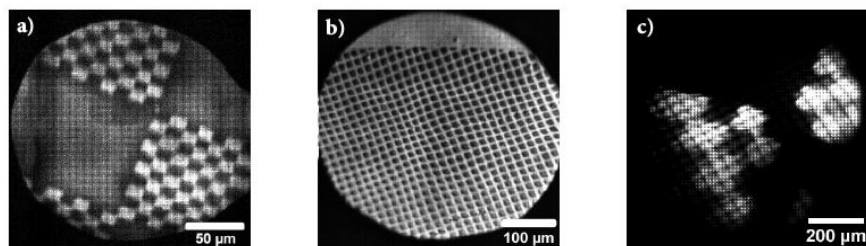
Figure 2 (a) UV-PEEM image of a "Chessy" test sample. (b) UV-PEEM image of a standard TEM-grid in the position of the transmitting film. (c) "Chessy" test sample (large squares) imaged through the TEM-grid (small squares).

For the second series of tests a low energy thermal emitter (BaO) was installed in the sample position, providing a higher emission rate than a photoemitter and making it pos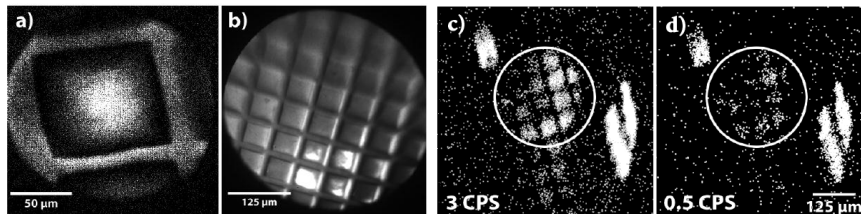sible to quickly test the transmission of various metal and non-metal films to be used as either filter or support material (Fig. 3).

Figure 3 (a) UV-PEEM image of a 5nm Si thin-film sample overlaid with a transmission image through the film; (b) UV-PEEM image of a 3nm Pd thin-film sample overlaid with a transmission image; (c) Transmission through a Pd thin-film sample before and (d) after coating with about 10nm of Co.

For a ferromagnetic material λ_{IMFP} also depends on the spin. Hence, a thin-film spinfilter can be realized by measuring electron transmission through a thin metal film for two opposing magnetization directions of the film [2]. A spin-polarized electron source is currently being assembled to test the spin-filter properties of magnetized ferromagnetic thin films in the setup.

References:
[1] W. Weber, S. Riesen and H.C. Siegmann, *Science* **291** (2001), 1015
[2] P. Dey and W. Weber, *J. Phys.: Condens. Matter* **23** (2011) 473201
[3] M.P. Seah and W.A. Dench, *Surface and Interface Analysis* 1 (1979) 2
[4] G.Schönhense and H. C. Siegmann, *Ann. Physik* **2** (1993) 465-474
[5] F. Passek, M. Donath and K. Ertl, *J. Magn. Magn. Mat.* **159** (1996) 103
[6] K. Zumbrägel, A. B. Schmidt and M. Donath, *DPG conference* Berlin 2012

IMAGING THE LOCAL DENSITY OF ELECTRONIC STATES BY VERY LOW ENERGY ELECTRON REFLECTIVITY

Z. Pokorná and L. Frank

Institute of Scientific Instruments AS CR v.v.i., Královopolská 147, 61264 Brno, CZ
e-mail: zuza@isibrno.cz

This work was concerned with the relationship between the reflectivity of very low energy electrons from a crystalline sample and its density of electron states above the vacuum level. Also, as different crystallographic orientations of the same single crystal exhibit different density of states, the usefulness of electron reflectivity at very low energies was demonstrated for the determination of crystallographic orientation. The technique chosen was the Scanning Low Energy Electron Microscopy (SLEEM) which allows using arbitrarily low electron energies while preserving a very good image resolution [1, 2]. In our experiments, the incident electron energy ranged between 0 and 45 eV.

Both standard vacuum and Ultra High Vacuum arrangements were tried. For the Ultra High Vacuum experiments, several samples were used: polycrystalline nickel, polycrystalline aluminium, single crystal aluminium Al(100), Al(110) and Al(111), single crystal tungsten W(110) and Highly Ordered Pyrolytic Graphite (HOPG). Different sample cleaning procedures were used, from insertion of the sample *as is,* to several cycles of thorough *in situ* argon ion cleaning combined with high temperature flashes.

It was indeed proven that differently oriented faces of the same single crystal exhibit different spectra of very low energy electron reflectivity, as shown in Fig. 1. The relationship between reflectivity and the density of states above vacuum level (as established from calculations) is demonstrated in Fig. 2. It was possible to show that there is indeed a relationship, although not one of a simple indirect proportionality. Various phenomena influencing the signal information come into play as well, including most importantly surface cleanliness and surface preparation procedures.
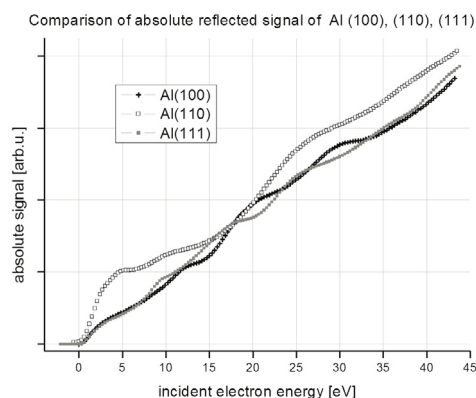
Figure 1 Reflectivity of very low energy electrons from differently oriented faces of an aluminium single crystal.
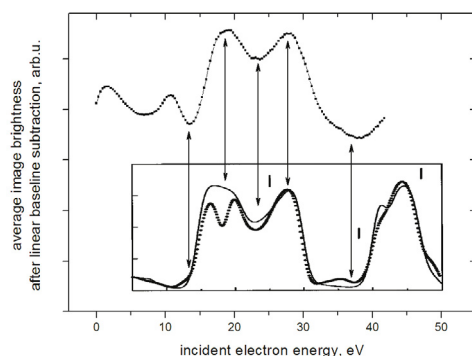
Figure 2 Comparison of calculated density of states with the reflectivity of very low energy electrons for an aluminium single crystal of the (100) orientation.

References:
[1] Müllerová I., Frank L., *Adv. Im. El. Phys.* **128** (2003), pp. 309-443
[2] Bauer, E., *Surf. Rev. Lett.* **5** (1998), pp. 1275-1286

CALCULATION OF DIFFRACTION ABERRATION USING DIFFERENTIAL ALGEBRA

T. Radlicka[1]

[1] Institute of Scientific Instruments of the ASCR, v.v.i. Královopolská 147, 612 64, Brno, Czech Republic

[*]e-mail: radlicka@isibrno.cz

Diffraction in electron optics

The resolution in light microscopy is limited mainly by the wave length of light. Although the wave length of the electron is several orders of magnitude smaller than that of light, the wave properties of the electron limit the resolution of scanning electron microscopes as well. It is described by the diffraction on the limiting aperture. While the effect of the diffraction can be reduced by increasing the limiting aperture size, it affects the resolution by increased geometrical and chromatic aberrations, that are more critical in the electron optics than in the light optics. These opposite trends cause that the best resolution is given by an aperture size that balances the effect of the diffraction with the effect of geometric and chromatic aberrations – an optimal aperture.

The recent knowledge regarding the diffraction calculations in electron optics were summarized in [1]. The general theory was described in details but the applications on real instruments have been reduced to systems with no electromagnetic fields between the limiting aperture and the sample with properties in the aperture plane described in terms of the paraxial approximation and the spherical aberration. More general systems have not been analyzed yet.

The diffraction integral for a point close to the axis can be written in the form

$$\psi(x_i, y_i) = C \iint_A \psi(x_a, y_a) \exp\left(\frac{i}{\hbar} S(x_a, y_a, x_i, y_i)\right) dx_a dy_a$$

where $S(x_a, y_a, x_i, y_i)$ is the point eikonal between given points in the aperture and image planes. The multiplicative constant C determines the absolute value of the current density, but it will not be considered in the contribution because we will compare only normalized distributions. The wave function in the aperture plane $\psi(x_a, y_a)$ is determined by the system optical properties in front of the aperture. For a point source (x_o, y_o) in the object plane, which is close to the axis we can find $\psi(x_a, y_a) = C \exp\left(\frac{i}{\hbar} S(x_o, y_o, x_a, y_a)\right)$. The point eikonal describes the paraxial and aberration properties of all optical elements in front of the aperture.

The form of the diffraction integral shows the main difficulty of the numerical evaluation. As the value of reduced Planck constant is very low $\hbar = 1.059$ e-34 Js, the value of the integral is very sensitive to the accuracy of the point eikonal S. It has been analytically described in case of paraxial approximation, and in case when only spherical and chromatic aberration are significant. The approach for the eikonal calculation in the general case was described in [1]. It is based on the numerical calculation of the two point boundary problem for trajectories, which has to be solved with precision about 14 to 15 significant digits. As this approach is very time consuming; we proceeded in a different way.

Differential algebra method for eikonal calculation

We will present the eikonal calculation based on the expansion of the eikonal function to the polynomial in positions in the aperture and image plane. This approach is a generalization of the

calculation of diffraction in the system with spherical aberration [1,2]. Our procedure is based on the application of the differential algebra (DA) method on the eikonal calculations and on efficient algorithm for evaluation of the rapidly oscillating function in the diffraction integral [3].

The differential algebra method is a very valuable tool for the calculation of aberrations in the general electron or ion optical systems. It can be simply used for high order aberration calculation, which is limited only by the accuracy of the high order derivatives of the axial field. We used procedures described in [4] to resolve that difficulty.

Using the DA method one finds the solution of the trajectory equation in the form of the polynomial in the position, slopes in the object plane and the energy deviation [5, 6],

$$x(z) = \sum_{i_1,i_2,i_3,i_4,i_5} C_{i_1,i_2,i_3,i_4,i_5}(z) x^{i_1} y^{i_2} x'^{i_3} y'^{i_4} dE^{i_5}$$

When this form of the solution is substituted into the trajectory equation, the fields are also expressed in the form of the polynomials and the both sides of the trajectory are expanded into polynomial, a differential equation can be found for all the coefficients. When these equations are solved for the initial condition $C_{10000} = C_{01000} = C_{00100} = C_{00010} = C_{00001} = 1$ and 0 for all other coefficient, the trajectory is found. We used COSYINFINITY library [5] for these computations; the differential equations were computed by the standard Runge-Kutta method. The eikonal was computed directly during the integration using equation

$$S' = (2m_e e\Phi^*)^{1/2}\sqrt{1 + x'^2 + y'^2} - e(x'A_x + y'A_y + A_z)$$

which results in the eikonal in the form of the polynomial in initial positions, slopes and energy deviation. Transition to the parameterization by positions in the aperture and image plane was done by the DA approach, which leads to a simple linear algebraic equation in DA space. An alternative method would be the calculation of the eikonal values from the direct ray-tracing followed by the fitting routine [7], which would allow calculating the eikonal in the polynomial form.

Calculation of the density function

When the eikonal function is known, the wave function in the image plane can be computed straightforwardly. The beam profile on the sample is computed from the density function, which is the square of the absolute value of the wave function, $\rho = \psi\psi^*$. In the real case the source has a non-zero size and energy width. We suppose that electrons emitted from different points on the cathode and with different energy are not coherent. Hence, the resulting density function is given as an integral of the density functions over the source plane and energy:

$$\rho(x_i, y_i) = C\int_E \rho(E)\left\{\iint_{source} \rho(x_o, y_o)\left|\iint_A e^{\frac{i}{\hbar}(S_E(x_o,y_o,x_a,y_a)+S_E(x_a,y_a,x_i,y_i))}\,dx_a dy_a\right|^2 dx_o dy_o\right\} dE$$

This calculation was done for a simple electrostatic lens. Figure 3 shows the behavior of the density function near the image. The classical trajectories are shown for the comparison. Figure 4 shows the effect of the defocus on the density function and the effect of the chromatic aberration and the finite size of the source. The results will be later compared with classical current density calculation [8,9].

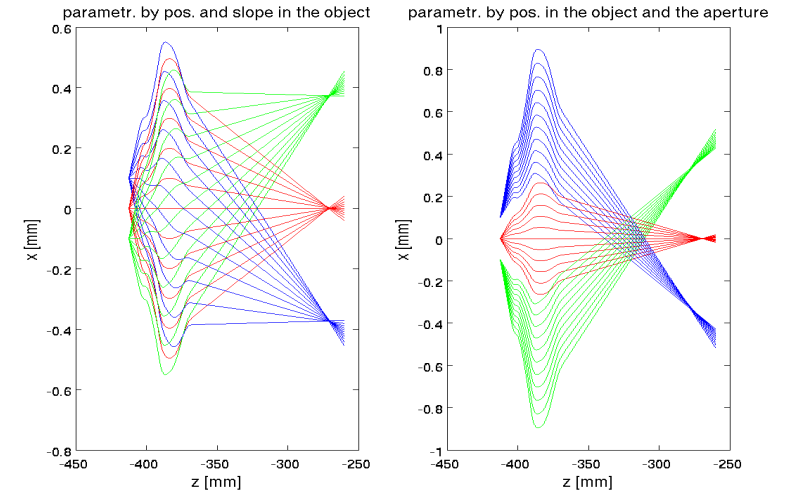**Figure 1 Trajectories in parameterization by position and slope in the object plane (left) and by position in object and aperture plane (right)**
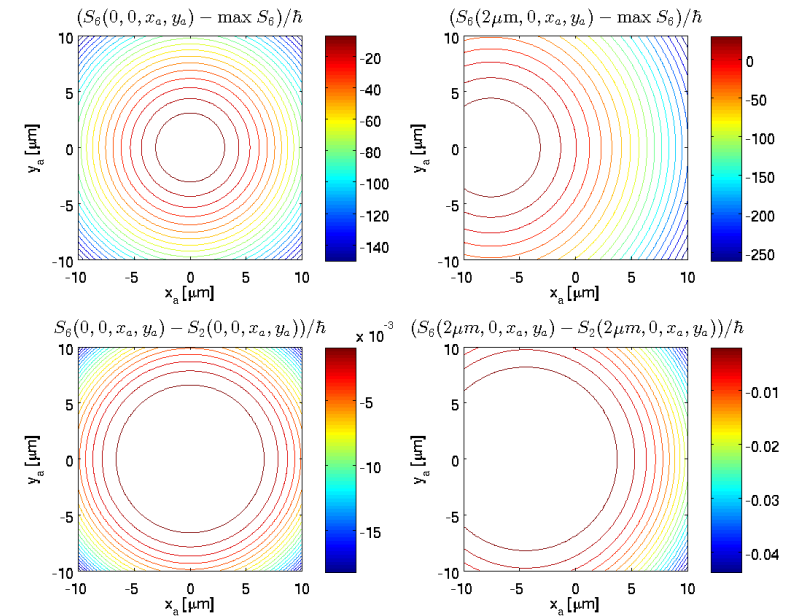

Figure 2 Value of the eikonal function in the aperture plane with accuracy up to sixth order for two different points (upper figures). The contribution of the aberration to the eikonal function is shown at the bottom.
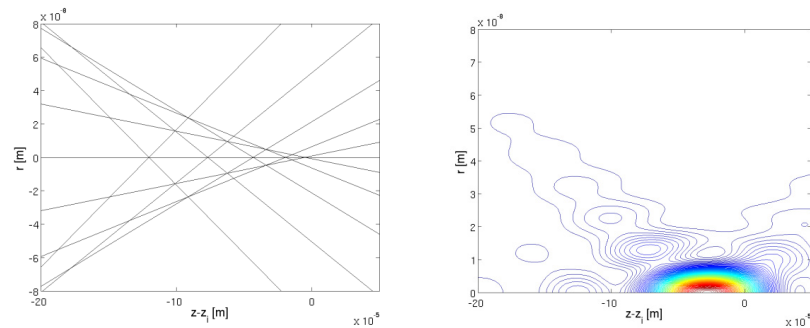
Figure 3 Aberration pattern of the axial beam near the image (left), corresponding density function (right)
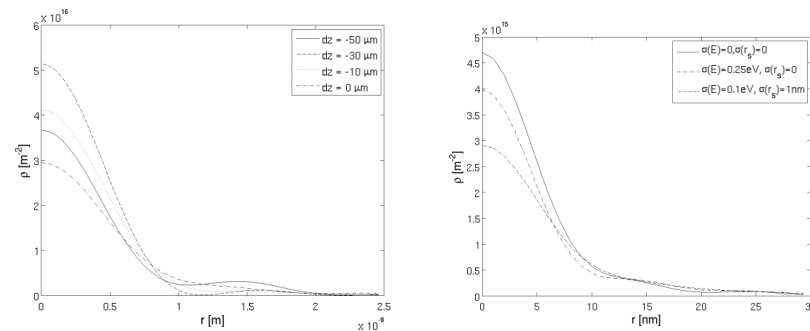

Figure 4 Series of profiles of point axial source for different values of the defocus (left), the effect of chromatic aberration and the source size (right)

[1] P.W. Hawkes, E. Kasper, Principles of Electron Optics, Academic Press, London, 1989.

[2] M. Born, E. Wolf, Principles of Optics, 7th Edition (Cambridge University Press, Cambridge, 2002) pp. 517-553.

[3] A. Mikš, J. Novák, P. Novák, Int. J. Numer. Engng, 82, (2010), 525 – 536

[4] T. Radlička, B. Lencová, Ultramicroscopy, 110(9) , (2010), 1198 – 1204

[5] M. Berz, Adv. Imaging. Elect. Ph. 108 (1999)

[6] T. Radlička, Adv. Imaging. Elect. Ph. 151 (2008), 241 – 362

[7] M. Oral, B. Lencová: Ultramicroscopy 109(11), (2009), 1365-1373

[8] M. Oral, B. Lencová: Nucl. Instrum Meth A, 645(1), 130-135

[9] M. Oral, et al., Ultramicroscopy (2011), doi:10.1016/j.ultramic.2011.11.011

PARALLEL SECONDARY ELECTRON DETECTION IN A MULTI-BEAM SEM

Y.Ren[1*], C.W. Hagen[2] and P. Kruit[2]

[1]Delft University of Technology, Faculty of Applied Sciences, Lorentzweg 1, 2628 CJ Delft, The Netherlands
*e-mail: Y.Ren-1@tudelft.nl

We developed a Multi-Beam Scanning Electron Microscope (MBSEM) based on a regular FEI Nova-Nano 200 SEM, but equipped with a novel multi-electron beam source module [1,2]. This source delivers a 14x14 array of focused beams, which are all de-magnified by the optical column of the SEM with a resolution and current per beam comparable to a state of the art single beam SEM. In order to use this system as an imaging system, parallel detection of the secondary electrons (SE's) generated by the 196 beams is required.
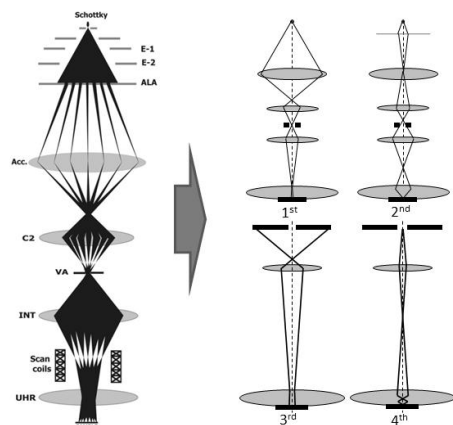
The key challenge is to separate the SE's from neighboring primary electron beams which are typically separated by 0.5 to 5 µm on the sample. It will be impossible to separate the different SE beams, with a few micrometer pitch on the sample, using a side detector. Therefore we propose to use in-lens SE detection. It is necessary to add an electrostatic lens (retarding lens) to accelerate the SE's and narrow their opening angle. This retarding lens is designed below the magnetic objective lens to form an electrostatic-magnetic objective lens.

The most practical plane to collect the SE's is the variable aperture (VA) plane (see figure 1), because it would be easiest to insert a detector into the column. In this plane an image of the sample is formed, using the secondary electrons. It is important to focus the SE beams in the detection plane with sufficient magnification. Because in order to get separated images of different SE beams, the pitch of neighboring SE beams should be larger than the spot size of each beam in the detection plane.

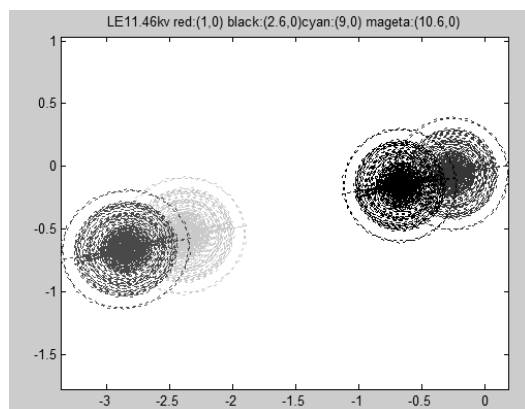We will present the results of simulations (landing energy=5keV, 11.4keV and 15keV), using the EOD package from SPOC (Brno), to demonstrate that the SE's in the multi-beam system can be detected separately in the detection plane for different landing energies in this multi-beam system. Even the furthest off-axis SE beams (10µm off axis) can still be separated from its neighbouring beams (see figure 2).

Figure 1 The optical system in MBSEM which can be divided into 3 sub optical system; the 1st is for single beam focusing; the 2nd is for multi-beam focusing; the 3rd shows SE magnification and the 4th shows SE focusing.

Figure 2 The distribution of secondary beams in the detection plane, originating from positions in the sample plane 1 μm apart, for a landing energy of 11.4 keV. The right cluster comes from near the axis, the left cluster from a corner of the 14x14 beams.

References:
[1] A. Mohammadi-Gheidari, P.Kruit, Nuclear Instruments and Methods in Physics Research A 645 (2011) 60
[2] A. Mohammadi-Gheidari, C. W. Hagen, and P. Kruit, J. Vac. Sci. Technol. B28, (2010) 1071

PROSPECTS AND FIRST RESULTS OF SUB-ANGSTROEM LOW-VOLTAGE ELECTRON MICROSCOPY– THE SALVE PROJECT

H. Rose* and U. Kaiser

University Ulm, Albert-Einstein-Allee 11, D-89069, Germany
*e-mail: harald.rose@physik.tu-darmstadt.de

The ultimate goal of high-resolution analytical electron microscopy is the acquisition of detailed information about the structure, the chemical composition and the local electronic states of the object on an atomic scale. This knowledge is necessary to elucidate relations existing between the macroscopic and the nanoscopic properties of solid and organic materials. Radiation damage is the fundamental limitation for the attainable specimen resolution. Specimen damage results from displacement and ionization of the constituent atoms of the object by the incident electrons. The tolerable electron dose D depends on the properties of the material and on the energy of the image-forming electrons. In order to avoid atom displacement for carbonaceous and other low-Z materials, the accelerating voltage must be lower than about 80kV. The specimen resolution limit d_S of radiation-sensitive objects is determined by the instrumental resolution limit d_i and the dose-dependent resolution limit d_n resulting from the noise:

$$d_S = \sqrt{d_i^2 + d_n^2}, \quad d_i \approx \frac{\lambda}{\alpha}, \quad d_n = \frac{\frac{S}{N}}{C\sqrt{D}}. \quad (1)$$

In order to discriminate in the image an object detail from the structural noise, the signal to noise ratio S/N must be larger than a fixed value which is commonly put equal to 4. The tolerable dose D decreases with decreasing energy E of the incident electrons whereas the contrast C increases such that the product CD is approximately constant. Therefore, d_n becomes smaller at lower energies, thus improving the specimen resolution provided that the instrumental resolution d_i is kept constant. In order to meet this requirement, we must enlarge the usable aperture angle α by means of a novel corrector because the wavelength λ of the electrons increases if their energy is reduced. The simultaneous compensation of chromatic and aperture aberrations requires electric magnetic quadrupole fields and octopole fields. The standard hexapole corrector can only eliminate spherical aberration because the hexapole fields do not affect the paraxial rays.

The SALVE (Sub-Angstrom Low-Voltage Electron microscope) project aims for atomic resolution of radiation-sensitive objects at low voltages by means of a dedicated TEM based on the Zeiss Libra microscope equipped with a novel corrector which compensates for the spherical aberration, chromatic aberration and off-axial coma. To enable local spectroscopy with high-energy resolution, an electrostatic monochromator and an aberration-corrected in-column Ω energy filter are incorporated into the microscope which will operate at voltages in the range between 20 and 80kV. The novel aberration corrector shown schematically in Fig.1 has excellent correction properties. It provides in combination with the objective lens usable aperture angles of at least 50mrad and a large field of view. The basic corrector consists of six multipole elements which are arranged symmetrically about the mid-plane z_m. Magnetic quadrupole fields are excited within each element. The front quadrupole doublet introduces the required astigmatic path of the electron trajectories which is eliminated by the exit doublet. Owing to the symmetry of the multipole fields and the exchange symmetry of the

paraxial rays with respect to the mid-plane, all field aberrations which are linear in the off-axial coordinates cancel out, except of the anisotropic (azimuthal) third-order coma of the magnetic objective lens. Skew octopole fields formed within the twelve-pole elements of the corrector compensate for this aberration. Regular octopole fields and crossed electric magnetic quadrupole fields are excited within the two inner twelve-pole elements. These octopole fields eliminate the spherical aberration of the objective lens. The remaining fourfold axial astigmatism, introduced by the quadrupole fields of the corrector, is nullified by the additional octopole centered at the midplane without introducing any linear off-axial aberrations. Apart from the astigmatic focusing, the electric-magnetic fields of the inner quadrupoles also act as first-order Wien filters compensating for the axial chromatic aberration. Because the field rays run close to the optic axis within the inner multipole elements, the formation of large non-linear off-axis aberrations (e.g. third-order field curvature and field astigmatism) is avoided. Due to the suppression of these aberrations a large field of view of more than 2000 equally-well resolved object elements per diameter is obtained.
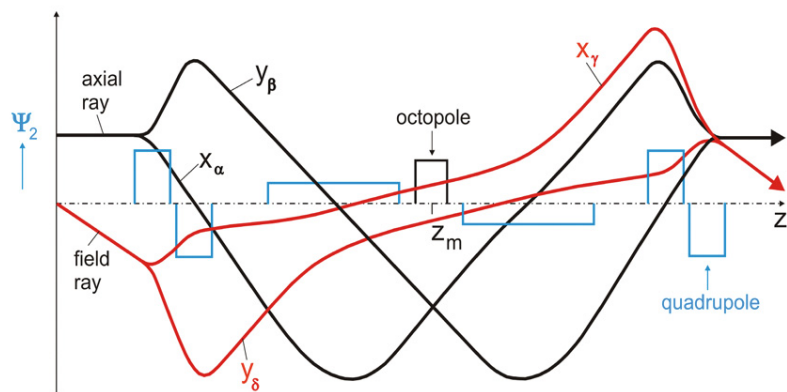

Fig.1: Scheme of the SALVE C_C/C_S-corrector and path of the fundamental paraxial rays, the blue boxes show the approximate strength Ψ_2 and the extension of the magnetic quadrupole fields. Chromatic correction is performed within the two inner multipole elements by superposition of additional crossed electric magnetic quadrupole fields acting as first-order Wien filters.

In order to achieve atomic resolution for amorphous objects their thickness must be smaller than the elastic mean free path length. Because this length is inversely proportional to the energy E of the incident electrons, the specimens must be very thin for low-voltage imaging. Moreover, the inelastic scattering cross-section $\sigma_{in} \approx \dfrac{Z\sigma_e}{18}$ is significantly larger than the elastic scattering cross-section σ_e for low-Z material. In this case, most electrons will be scattered inelastic or scattered elastically and inelastic depending on the thickness of the specimen. Removing these electrons by the imaging energy filter reduces the image intensity and the S/N considerably if the object thickness is appreciably larger than the inelastic mean free path length. Fortunately, we can utilize a large fraction of these electrons because the corrector can handle energy deviations up to at least $\pm 10\text{eV}$ even at very low voltages. Detailed image simulations have shown that at low voltages even light atoms like carbon are strong scatters which produce large amplitude contrast.

CURRENT STATE AND PROSPECTS OF SCINTILLATION MATERIALS FOR DETECTORS IN SEM

P. Schauer and J. Bok

Institute of Scientific Instruments of the AS CR, v.v.i., Královopolská 147, Brno, CZ-61264, Czech Republic
*e-mail: petr@isibrno.cz

The two principal quantities are important for assessing the quality of each imaging system. Firstly, it is the detective quantum efficiency (DQE), which is primarily a measure of image noise. As the DQE is determined by signal to noise ratio (SNR), the efficient and noise-free components are the key to the high DQE. Second, not less important indicator of image quality is also the modulation transfer function (MTF). MTF describes the ability of adjacent pixels to change from black to white in response to patterns of varying spatial frequency, and hence it determines the actual capability to show fine detail, whether with full or reduced contrast. Using a scanning imaging system the fast components are the key to the good MTF. In a scintillation electron detector of scanning electron microscope (SEM) the scintillator is the most crucial component, because it significantly influences both the DQE and MTF. The aim of this study is to assess the scintillation materials suitable for SEM detectors characterized by the both high efficiency and fast decay characteristic.

Looking for scintillators suitable for detectors in SEM, it is necessary to exclude all standard hygroscopic materials such as CsF, NaI:Tl, CsI:Tl or BaF_2. They are not suitable for electron detectors as they require a housing to be protected from moisture. Unfortunately, for the same reason some newly developed products including $LaCl_3$:Ce and $LaBr_3$:Ce do not come into consideration. It is a pity, because they are characterized by excellent light yield, stability and linearity as well as by a very fast response. Excluded must be also so call cross-luminescent materials, as they have a relatively low light yield. Thus the only scintillators suitable for detectors in SEM are those based on oxides. However the self-activated oxides have a poor combination of light yield and time response, so that only activated oxides can be considered. From these the scintillators characterized by a very fast 4f-5d emission are the best choice.

Earlier CL studies of scintillators carried out in our laboratory [1] and shown in Table 1 resulted in conclusions that defect centres are responsible for a deterioration of CL decay characteristics of YAG:Ce and YAP:Ce, and the possibilities of kinetics enhancement consist in a reduction of the influence of these defect centres. The CL properties of the Crytur scintillators recently studied in our laboratory are listed in Table 2. The durations of excitation pulses at the earlier as well as at the present measurements have been 10 μs. It can be seen that the current single crystal scintillators from the Crytur Company are generally faster. First of all they possess much lower afterglow. It succeeded, although the CL efficiency was retained or even increased. This is due to elimination of the defect centrum influences. Of course, scintillators having lower activator concentration are slower width lower efficiency.

In the future, probably the major way to reduce the afterglow of scintillators and at the same time to increase the efficiency will be efforts of increasing the activator concentration.

Unfortunately, this is not an easy task for a single crystal grown because of a sharp decrease of the distribution coefficient at the crystal growth. Feasible, but at the expense of some efficiency decrease can be crystal co-doping to reduce the afterglow through nonradiative recombination. As for the material structure, very promising is the development of optical ceramics for the scintillator applications [2].

Table 1. Cathodoluminescence properties of earlier [1] YAG:Ce single crystal scintillators for SEM. [1]Intensities of the CL emission (in arbitrary units) have been corrected for the photocathode used.

single crystal	—— conditions ——		—— cathodoluminescence ——		
	activator conc. (mol%)	fired	intensity[1] of char. emis.(AU)	decay time (ns)	afterglow (% at 1 µs)
YAG:Ce — 0.32 —		O_2	64	75	5
		H_2	139	131	10
		as grown	100	125	9
YAP:Ce	0.4	as grown	194	38	6.4

Table 2. Cathodoluminescence properties of new generation of Crytur single crystal scintillators for SEM. [2]Intensities of the CL emission have been corrected for the photocathode used and have been related to the intensities of the scintillators in Table 1.

single crystal	—— conditions ——		—— cathodoluminescence ——		
	activator conc. (mol%)	fired	intensity[2] of char. emis.(AU)	decay time (ns)	afterglow (% at 1 µs)
YAG:Ce	0.4	as grown	109	125	5.9
YAP:Ce	0.1		171	67	5.6
YS:Ce	0.2		95	47	0.6
CRY18	n/a	n/a	188	56	0.3
CRY19			173	41	0.8
LXSR			160	46	0.3

References:
[1] Autrata R. and Schauer P., Scanning Microscopy (Supplement), **9** (1996), p. 1-12.
[2] Miyata T., Iwata T., Nakayama S. and Araki T., Meas. Sci. Technol. **23** (2012), AN: 035501, DOI: 10.1088/0957-0233/23/3/035501

100³ THE LIBRA 200 C$_s$STEM

R. Schillinger[1],

[1]Carl Zeiss Microscopy GmbH, Carl Zeiss Straße 56, 73477, Oberkochen, Germany
*e-mail: richard.schillinger@zeiss.com

This contribution showcases the performance of the Zeiss Libra 200 C$_s$STEM with emphasis on the utilisation of the gun monochromator.

Analytical electron microscopy relies on high spatial as well as high spectral resolution. The key ingredients of such an instrument are a bright field emission electron gun delivering an intense, coherent beam from a small source[1,2], a monochromator [3,4] in the gun to further reduce the energy spread of the primary beam and a corrector for the limiting aberrations of the probe forming system[5,6]. Such (scanning) transmission electron microscopes ((S)TEM) have proven atomically resolved spectral maps feasible in electron energy loss spectroscopy (EELS) and energy dispersive X-ray spectroscopy (EDS) [7-9]. Through the improved energy resolution due to the monochromator, energy loss ear edge structure (ELNES) in TEM can compete with X-ray adsorption near edge spectroscopy (XANES) even on third generation synchrotron light sources [10]. With the additional benefit of the superior lateral resolution in the (S)TEM over present X-ray techniques.

The base microscope is a Zeiss Libra 200 FE MC with an incolumn imaging energy filter and equipped with a probe Cs corrector (CEOS CESCORR [6]). Applying the gun monochromator (built also by CEOS [4]) brings the energy spread of the electron probe below 100 meV. Energy selection is engaged just by mechanically introducing a narrow slit into the beam path in the dispersive plane of the MC, or by a slight electrostatic deflection of the beam in the MC. The imaging conditions of the electron source to the sample plane are not altered and the demagnification of the probe stays constant with and without energy discrimination.

Figure 1 a) shows a HAADF STEM image of Si-<110> resolving the well known dumbbells with 136 pm spacing. The spectrum of the direct beam used to acquire this image monochromated to an energy spread of 93 meV (FWHM) is displayed in figure 1. b). Fourier filtering was applied to figure 1. a) to remove statistical noise. A raw image at an energy spread of dE = 245 meV is shown in figure 2. The fast Fourier transform (fig. 2 b) shows transfer until the 422 reflexes (111 pm). This increase is due to the better signal to noise ratio since beam current is increased as more electrons are admitted to form the beam at the specimen location with respect to the 93 meV image. The images were taken at 200 keV electron energy.

Hence, the title collects three characteristic figures: 100 pA beam current for high resolution STEM at the 100 pm level and 100 meV energy spread of the primary beam using the monochromator .
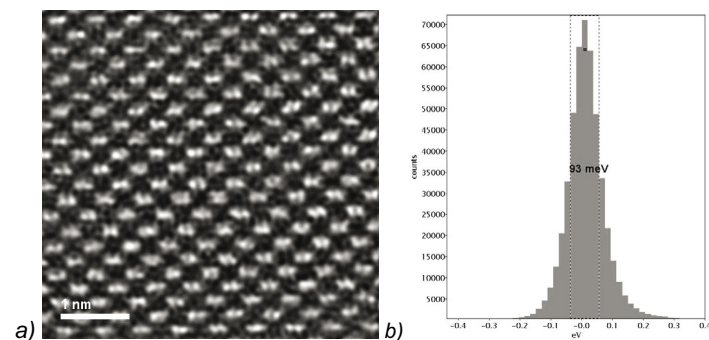
Figure 1. *a) HAADF STEM Image of Si <110>, fourier filtering has been applied to remove statistical noise. b) Spectrum of monochromated direct beam dE= 93 meV(FWHM).*
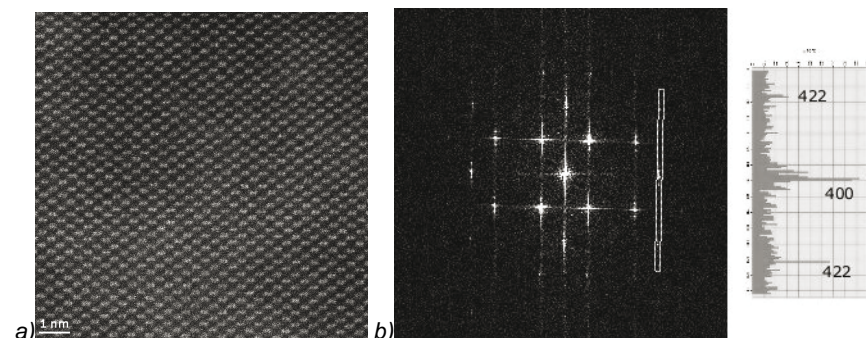
Figure 2. *HAADF STEM image of Si <110> raw data; dE = 245 meV and FFT with line plot of intensities of 400 and 422 reflexes.(Scale bar 1 nm)*

References:
[1] N.J. Bacon et al., Proc. 17th IMC (2010), 240
[2] B. Freitag et al., Microsc Microanal **14**(Suppl 2) (2008), 1370
[3] F.Kahl, H. Rose, Proc 11th EUREM11, Vol 1 (1996), 478
[4] S. Uhlemann, M. Haider, Proc. 15th ICEM, Vol.3 (2002), 327
[5] M. Haider et al., Nature, **392** (1998), 768
[6] M. Haider, S. Uhlemann, J. Zach, Ultramicroscopy **81** (2000), 163
[7] Kimoto K. et al., Nature **450** (2007), 702
[8] Watanabe M. et al. Microsc Microanal **12** (2006), 515
[9]D'Alfonso A.J. et al. Phys Rev B **81** (2010), 100101
[10] M. Cheynet et al., Ultramicroscopy **110** (2010), 1046
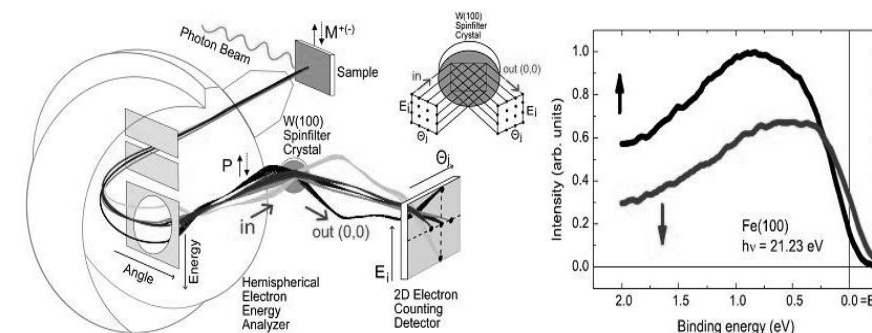
IMAGING SPIN FILTER FOR ELECTRONS

G. Schönhense

Institut für Physik, Johannes Gutenberg Universität, D-55099 Mainz, Germany
Email: schoenhense@uni-mainz.de

Stern-Gerlach-type spin filters for electrons are impossible because of the interplay between Lorentz force and Heisenberg uncertainty relation. Spin analysis of electron beams is accomplished by spin dependent scattering processes that are based on spin-orbit or exchange interaction. In the high energy range Mott-scattering at high-Z targets or Moeller scattering at ferromagnetic targets are exploited [1]. In the energy range below 100eV spin dependent low energy electron diffraction (SPLEED) at high-Z single crystals [2] or at ferromagnetic surfaces [3] can be utilized. All of these are inherently single-channel methods characterized by low figures of merit of typically 10^{-4} to 10^{-3}. Lateral resolution can only be achieved by scanning the electron beam across a sample like in scanning electron microscopy with polarization analysis (SEMPA or Spin-SEM).

The single-channel approach is not compatible with parallel imaging microscopes (PEEM, LEEM, TEM) and also not with modern electron spectrometers that acquire a certain energy and angular interval simultaneously, yielding up to 10^4 data points in parallel. Comparing a state-of-the-art electron spectrometer with subsequent single channel spin polarimeter with a hemispherical energy analyzer of the present generation (detecting 10^4 data points simultaneously) we are facing a difference in detection efficiency of 7-8 orders of magnitude!

Our new method makes use of the fact that an electron-diffraction process is principally capable to transmit lateral image information. This is illustrated in Fig. 1a for the idealized case of a perfectly parallel beam specularly diffracted at a single-crystal surface. This yields a spin-filtered image when diffraction energy and angle are chosen such that a high spin asymmetry is present [4]. In the present contribution the different application cases will be discussed, depending on whether the two lateral coordinates of the spatially-resolved diffraction process correspond to spatial coordinates (x,y), components of the momentum vector (k_{lx}, k_{ly}), energy coordinate or combinations of these. Fig. 1 shows the application of the ***spin filter behind a hemispherical electron spectrometer*** yielding 4 orders of magnitude improvement of spin detection efficiency [5]. This is a large advantage for the study of highly reactive surfaces [6] or for photoemission in the hard X-ray range (Spin-HAXPES).


Figure 1   Scheme (centre top), electron optical layout (left) and a spin-resolved spectrum of an Fe film (right) of the imaging spin filter behind a hemispherical energy analyzer. (from [5])

The gain in performance results from the simultaneous acquisition of 1000 data points (Ei/θj) along with a high asymmetry function of 0.43 and a reflectivity of 1.2%. This makes up a "2D figure of merit" *F2D* = 1.8 being a measure of the performance in comparison with common single-channel spin polarimeters $F1D = 10^{-4}$ to 10^{-3} (for details, see [5]). A further increase of an order of magnitude seems feasible.

When used in a PEEM, the imaging spin filter yields ***high contrast magnetic images*** and is suitable for the direct observation of magnetization structures on ferromagnetic surfaces and their ultrafast dynamics. In this mode the spinfilter crystal (e.g. W(100) or Ir(100)) is placed in a crossover of the electron beam at the desired scattering energy (different working points in the range below 100eV) as sketched in Fig. 2. A non-spinfiltered image can be detected in the horizontal branch when the spinfilter crystal is retracted. The device built at the Max Planck Institute in Halle can resolve 3800 pixels and is characterized by *F2D* = 8   [7]. The magnetic contrast is larger than in the commonly used XMCD-PEEM technique, cf. Fig. 2 a (spinfiltered image) and (b) XMCD-PEEM image.

Finally, the two transversal momentum components (k_{lx}, k_{ly}) can be resolved by the imaging spin filter, leading to ***spin-resolved momentum microscopy***. This mode is also realized in the instrument in Halle. In this contribution we will discuss all for cases, with emphasis on the first two which have been demonstrated in previous experiments.
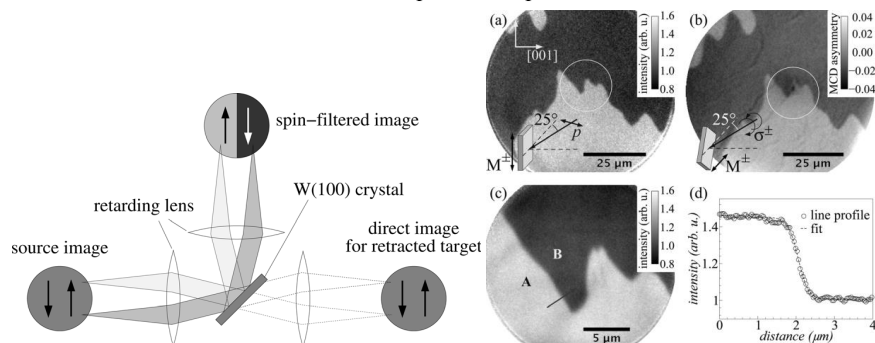
Figure 2   Working principle (left) and ferromagnetic domain images of the spin filter in the column of a low-energy microscope. The spin-filtered image of a Co film (a,c) exhibits a higher magnetic contrast than the XMCD image of the same field of view (b). (from [7])

----

[1] J. Kessler, *Polarized Electrons*, Springer Berlin (1976)
[2] J. Kirschner, *Polarized Electrons at Surfaces,* Springer Tracts in Mod. Phys. **106** (1985)
[3] F.U.Hillebrecht, R.M.Jungblut, L. Wiebusch, C. Roth, H.B. Rose, D. Knabben, C. Bethke, N.B.Weber, S. Manderla, U. Rosowski, and E. Kisker, *Rev. Sci. Instrum*. **73** (2002) 1229
[4] Patent DE 10 2005 045 622 B4
[5] M. Kolbe, P. Lushchyk, B. Petereit, H.J. Elmers, G. Schönhense, A. Oelsner, C. Tusche and J. Kirschner; *Phys. Rev. Lett.* **107** (2011) 207601
[6] M. Kolbe et al.; *Phys. Rev.* B (2012) *in print* and *Appl. Phys. Lett*. **98** (2011) 232503-3
[7] C. Tusche, M. Ellguth, A. A. Ünal, C. T. Chiang, A. Winkelmann, A. Krasyuk, M. Hahn, G. Schönhense and J. Kirschner; *Appl. Phys. Lett*. **99** (2011) 032505

DETECTION OF SURFACE VOLTAGE CHANGES USING A SECOND-ORDER FOCUSING TOROIDAL ENERGY ANALYZER SEM ATTACHMENT

A. Srinivasan and A. Khursheed

Dept. of Electrical and Computer Engineering, National University of Singapore, Block E4, Level 5, Room 45, 4 Engineering Drive 3, Singapore 117576
e-mail: avinash.srinivasan@nus.edu.sg

A second-order focusing toroidal analyzer SEM attachment was reported by Khursheed and Hoang. [1]. Initial experimental SE signals related to the SE spectrum demonstrate that it has high signal-to-noise capability in detecting specimen voltage changes, well into the sub-mV range [2], and is therefore of interest for mapping dopant concentration in semiconductor samples. However, these initial results were obtained in idealised conditions, for field-free conditions above a large metal sample. This work presents SE signals from the analyzer for doped semiconductor samples under more realistic conditions, in the presence of contamination, oxidation and surface fields.

Figure 1 shows the layout of the modified second-order focussing toroidal analyzer prototype. The sample holder is modified from the hemispherical arrangement reported earlier [1] to a concentric conical structure, in which the specimen, and inner/outer caps can be independently biased. The scattered electron energy distribution can be obtained by ramping the analyzer deflection electrodes and monitoring the PMT output. In addition, the sample and conical caps can be biased to further increase the SE signal sensitivity to specimen voltage changes. Experimental SE signals for the n-type doped side of an uncoated solar cell sample were obtained for the specimen voltage changing from –10V to –13V, and are shown in Fig 2. The outer conical cap voltage V_{C2} and the inner conical cap voltage V_{C1} are set to 0V and -10V respectively. There will obviously be surface micro-fields created above the specimen when the specimen voltage and inner cap voltage differ. Figure 2 shows that as the sample becomes more negative with respect to the inner cap voltage, the SE signal decreases in amplitude as well as shifts towards the right. As the specimen becomes more negative with respect to the inner cap voltage, low energy secondaries are deflected upwards by accelerating surface micro-fields, are pulled away from the analyzer entrance slit, thereby decreasing the signal amplitude, while the width of the SE signal grows because the kinetic energy of the SEs as they travel through the analyzer increases. To better quantify the specimen voltage change, the output signal mean μ and the standard deviation σ are monitored. The standard deviation σ is plot against the change in specimen voltage, ΔV_s, as shown in Fig. 2 (b), and is found to vary in an approximately linear way. This result demonstrates that it is possible to quantify surface specimen voltage changes in non-metallic specimens even in the presence of surface micro-fields, and confirms that the second-order focusing toroidal analyzer has a variety of different applications that involve surface voltage detection, such as dopant concentration mapping, and quantifying charging/contamination in the SEM.
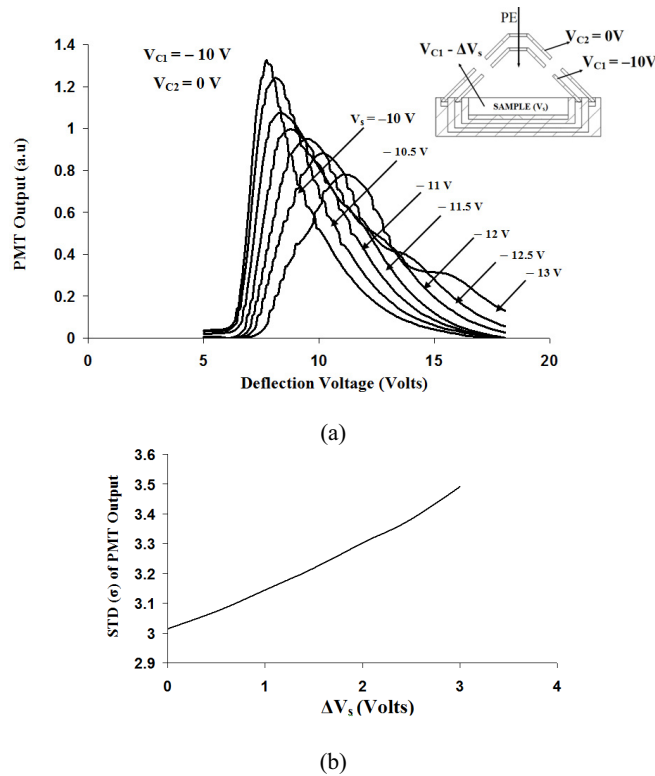
References:
[1] A. Khursheed, H.Q. Hoang, Ultramicroscopy 109 (2008) 104.
[2] H.Q. Hoang, M. Osterberg, A. Khursheed, Ultramicroscopy 111 (2011) 1093–1100
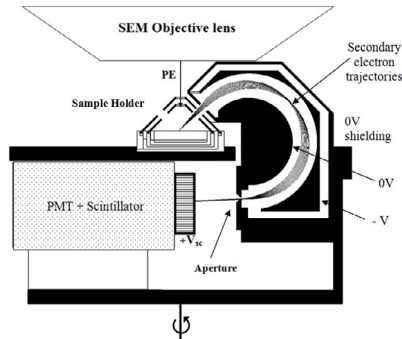
Figure 1 Layout of the modified second-order focussing toroidal analyzer prototype. The sample holder is a modified version of the prototype reported by Hoang *et al* [2]

(a)

(b)

Figure 2 Experimental SE signals obtained from a semiconductor sample (Solar Cell). (a) Specimen biasing from – 10 to –13 volts with V_{C1} = –10 V, V_{C2} = 0. Inset shows the biasing condition of the sample holder. (b) A plot of PMT signal STD (σ) for specimen potential change (ΔV_s) from 0 to 3V

PROXIMITY EFFECT SIMULATION FOR VARIABLE SHAPE E-BEAM WRITER

V. Kolarik[1], M.Matějka[1], M. Urbánek[1*], S. Král[1], S. Krátký[2], P. Mikšík[3], J. Vašina[3]

[1] Institute of Scientific Instruments ASCR, Královopolská 147, 612 64 Brno, Czech Republic

[*] e-mail: urbanek@isibrno.cz

[2] FEEC Brno University of Technology, Technická 3058/10, 61600 Brno, Czech Republic

[3] ELTEK spol. s.r.o, Tomečkova 4298, 767 01, Kroměříž, Czech Republic

Electron Beam Writer (EBW) is a lithographic tool allowing generation of patterns in high resolution. The writing is carried out into a layer of a sensitive material (resist), which is deposited on the substrate surface (e.g. silicon). The resolution of the EBW is limited not only by the beam spot size, but also by the electron scattering effects (forward scattering, backscattering). Thus, even if the beam spot size on the resist surface is very small, due to electron scattering effect in the resist, the exposed area is significantly broader than the original beam spot size [1, 2].

From the aspect of electron beam lithography (EBL) the electron scattering phenomenon, also called proximity effect, cause that the dose transferred in the outer regions of the writing area receive a nonzero dose. This causes the exposure dose distribution and the final pattern size is wider than intended.

The electron scattering effects can be approximated by the two Gaussian functions model (see 1) [3]. This model represents the distribution of energy absorbed in the material in distance r from the incidence point of primary electrons (PE), where α is the forward scattering range, β is the back scattering range and η determines the ratio between the energy absorbed from the back scattered electrons (BSE) and the PE.

$$f(r) = \frac{1}{1+\eta}\left(\frac{1}{\pi\alpha^2}\exp\left(-\frac{r^2}{\alpha^2}\right) + \frac{\eta}{\pi\beta^2}\exp\left(-\frac{r^2}{\beta^2}\right)\right) \qquad (1)$$

The first step towards compensation of proximity effect is to understand its influence on the exposed/unexposed area. From this reason the Proximity Effect Simulator (PES) for simulation of dose distribution has been created. The input parameters for the PES are coefficients α, β and η. Values of those parameters were mathematically and experimentally evaluated in preview works [3, 4]. The PES allows simulation of the dose distribution of the exposition pattern (see Fig 1a). When the resist sensitivity curve is known, the next step is the simulation of the resist development process (see Fig 1b). As it can be seen on the Fig.1, the individual exposure points of the pattern have the same exposition time (dose), except for four points at the right and bellow the main pattern. Cross sections *A-A'* and *B-B'* shows non ideal dose distribution. Similarly, for the simulation of the profile, the dose is insufficient for the developer reaches the surface of the substrate (e.g. silicon). The parameters chosen for PES tool follows: α = 0.20, β = 1.20 and η = 0.74. The exponential shape of sensitivity curve with parameters γ = 3.0; D_0 = 100 μC/cm^2 was used for the resist development process.

In conclusions, we managed to create a tool for simulation of electron scattering phenomena for patterns recorded using e-beam writer with a shaped beam. Experiments were provided with the EBW system (TESLA BS 600) that works with a fixed energy of 15keV and a rectangular variable-size beam shape. The system can be operated in one of the two patterning modes: the standard one (ST-mode) and the one with reduced–size beam shape (TZ-mode) [5, 6]. Further work should deal with a software tool that will be capable of offline proximity effect compensation by the dose modulation method.
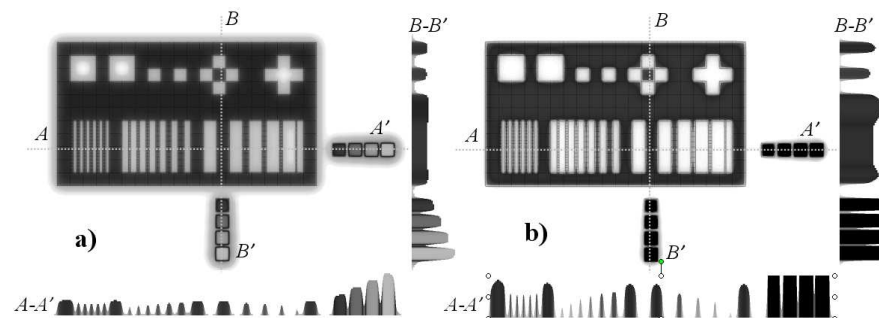
Figure 1. Simulation from the Proximity Effect Software (PES): a) dose distribution; b) depth distribution.

References:

[1] Franssila S., Introduction to Microfabrication (2004), p. 93-95.

[2] Rai-Choudhury P., Handbook of Microlithography, Micromachining and Microfabrication **Vol.1** (1997), p. 155-164.

[3] Urbánek M., Kolařík V., Král S., Dvořáková M., Determination of proximity effect forward scattering range parameter in e-beam lithography. *In Proc. 12th Int'l Seminar on Recent Trends in CPO (2010),* p. 67-68.

[4] Kraats A. van der, Raghuntah M., Proximity effect in E-beam lithography, http://nanolithography.gatech.edu/proximity.htm, p. 1-5.

[5] Kolarik V., *et al.*, Writing System with a Shaped Electron Beam, *Jemná mechanika a optika*, **Vol. 53**, No. 1 (2008), p. 11–16, ISSN 0447–6441.

[6] Matějka F., Practical e-beam lithography (2012), p.4-27.

CLASSICAL AND ADVANCED METHODS OF OPTICAL MICROMANIPULATIONS AND THEIR APPLICATIONS

P. Zemánek[*], O. Brzobohatý, M. Šiler, V. Karásek, O. Samek, P. Jákl, M. Šerý, J. Ježek

Institute of Scientific Instruments of the ASCR, v.v.i., Královopolská 147, 612 64 Brno
[*]e-mail: zemanek @isibrno.cz

Optical micro-manipulation techniques have been using for more than 30 years to transfer the momentum from light to microparticles or nanoparticles and influence their movement in liquid, on the surface, or in the air. These days such techniques become more developed and frequently used in physics, chemistry and biology to manipulate, trap, rotate, or sort various types of objects, including living cells in a contactless and gentle way [1].

This contribution will briefly introduce into the "classical" methods of optical micromanipulations, such as optical tweezers and holographic optical tweezers, and their combinations with selected diagnostics methods. Optical tweezers [2] represent the most famous tool for manipulation with microparticles and nanoparticles using light. This tool is based on a single tightly focused laser beam and provides a spatial confinement of a microobject, having refractive index higher comparing to the surrounding medium. Especially its combination with precise detection of the position of the optically trapped probe provided sensitive tenzometer enough to measure directly the force interaction at the level of single biomolecules leading to the investigation of various types of molecular motors [3]. This classical single beam optical tweezers have been gradually evolved into more complex tool (frequently called holographic optical tweezers) providing controlled 3D confinement of many microparticles using so-called spatial light modulators [4]. This method also enables spatial organization of many microparticles into complex spatial geometries.

Several novel micromanipulation methods will be described, too. They will cover optical trapping of nanoparticles or synchronous delivery of thousands confined microobjects in interfering laser beams. Here the interference of two or more coherent laser beams is used and regular pattern of intensity maxima and minima (so called optical lattice) is generated [5]. Particles are confined either in intensity maximum or intensity minimum depending on their size with respect to the lattice constant. Optical sorting in heterogeneous colloidal suspensions represents an interesting way how to separate particles or microorganisms of different properties dispersed in liquid in a contactless way [6]. This method is usually combined with microfluidic platforms and optical detection method based on fluorescence or laser spectroscopy. Especially combination with Raman microspectroscopy (so-called Raman tweezers) has already found numerous applications especially in the fields of analytical and physical chemistry and cell and molecular biology [7]. The combined technique offers the possibility of analyzing individual target microobjects under relevant environmental conditions. Moreover, it allows detecting directly the variations of their individual properties and composition which would be otherwise lost in an ensemble-averaged measurement. However, with increasing number of particles confined in the structure the original spatial light pattern is more severely disturbed and the particles themselves dictate their final spatial organization. This phenomenon is called optical binding [8] and it has been also demonstrated

that the particles self-organize in the light beams even without the existence of the optical lattice and form so-called optically bound structures (OBS).
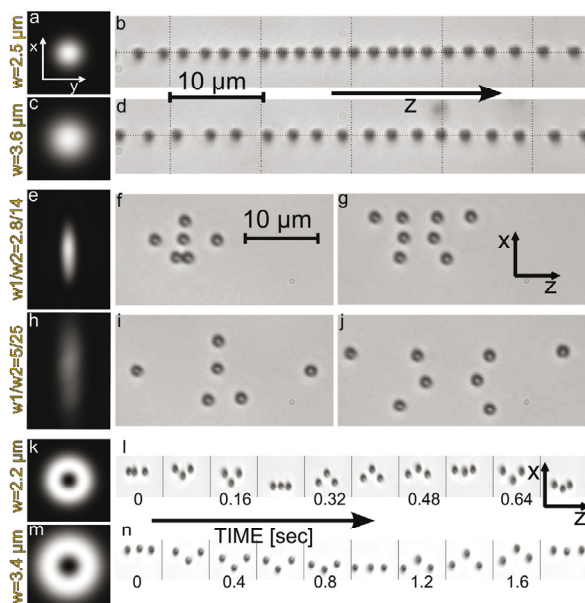
Figure 1. Examples of tunable optically bound structures. Left column: Lateral intensity profiles measured in one of counter-propagating identical incoherent laser beams propagating along or against z axis. (b,d) Side view of chains of polystyrene micro-particles (diameter 800 nm) self-arranged along the z axis of counter-propagating (CP) Gaussian beams of waists 2.5 μm (a,b) and 3.6 μm (c,d). (f,i) and (g,j) Examples of two-dimensional OBSs formed by polystyrene particles of diameter 1070 nm in xz plane in CP elliptical Gaussian beams of lateral profiles (e,h). (l,n) Examples of OBSs made of three polystryrene spheres (diameter 1070 nm) revolving around z axis of two CP Laguerre-Gaussian beams of opposite topological charges +/1 of two different lateral intensity profiles (k,m).

References:
[1] Jonáš, A., Zemánek, P., Electrophoresis **29** (2008), 4813-4851
[2] Ashkin A., *et al.* Opt. Lett. **11** (1986) 288-290.
[3] Mehta A. D. *et al.* Science **283** (1999)**,** 1689-1695.
[4] Dufresne E. R., *et al.* Rev. Sci. Instr. **72** (2001), 1810-1816.
[5] Čižmár, T. *et al.* Appl. Phys. B **84** (2006), 197-203.
[6] Dholakia, K. *et al.* Methods in Cell Biology **82** (2007), 467-495.
[7] Petrov, D.V. J. Opt. A **9** (2007), S139–S156
[8] Dholakia, K., Zemánek, P., *Rev. Mod. Phys.* **82** (2010), 1767-1791